AD-A191 996 CENTER FOR THIN FILM STUDIES(U) ARIZONA UNIV TUCSON 1/2
OPTICAL SCIENCES CENTER R P SHANNON ET AL. 15 NOV 87
AFOSR-TR-88-0136 F49620-86-C-0123

UNCLASSIFIED F/G 20/12 NL

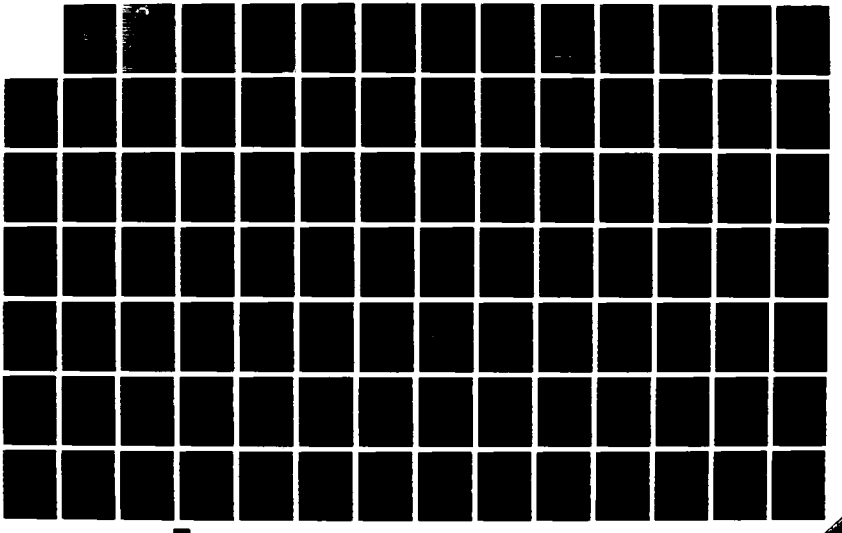

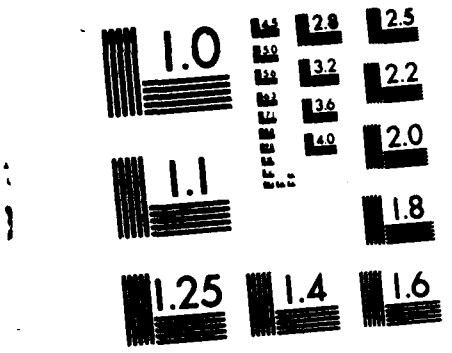


MICROCOPY RESOLUTION TEST CHART
NATIONAL BUREAU OF STANDARDS-1963-A

DTIC FILE COPY

(2)

UNCLASSIFIED
SECURITY CLASSIFICATION OF THIS PAGE

# REPORT DOCUMENTATION PAGE

DTIC ELECTE MAR 01 1988 D

| | |
|---|---|
| 1a. REPORT SECURITY CLASSIFICATION: Unclassified | 1b. RESTRICTIVE MARKINGS |
| 2a. SECURITY CLASSIFICATION AUTHORITY | 3. DISTRIBUTION / AVAILABILITY OF REPORT: Approved for public release, distribution unlimited |
| 2b. DECLASSIFICATION / DOWNGRADING SCHEDULE: a-H | |
| AD-A191 996 | 5. MONITORING ORGANIZATION REPORT NUMBER(S): AFOSR-TR- 88-0136 |
| 6a. NAME OF PERFORMING ORGANIZATION: Optical Sciences Center | 6b. OFFICE SYMBOL (If applicable): |
| 6c. ADDRESS (City, State, and ZIP Code): University of Arizona, Tucson, Arizona 85721 | 7a. NAME OF MONITORING ORGANIZATION: ONRRR Same 8a |
| | 7b. ADDRESS (City, State, and ZIP Code): Same 8b |
| 8a. NAME OF FUNDING / SPONSORING ORGANIZATION: AFOSR/ | 8b. OFFICE SYMBOL (If applicable): NE |
| 8c. ADDRESS (City, State, and ZIP Code): Air Force Office of Scientific Research, Bldg. 410, Bolling AFB, Washington, D.C. 20332-6448 | 9. PROCUREMENT INSTRUMENT IDENTIFICATION NUMBER: F 49620-86-C-0123 |
| | 10. SOURCE OF FUNDING NUMBERS: PROGRAM ELEMENT NO. 61102F; PROJECT NO. 3484; TASK NO. A3; WORK UNIT ACCESSION NO. |

11. TITLE (Include Security Classification): Center for Thin Film Studies

12. PERSONAL AUTHOR(S): Robert R. Shannon, Ursula J. Gibson, et al.

| 13a. TYPE OF REPORT | 13b. TIME COVERED | 14. DATE OF REPORT (Year, Month, Day) | 15. PAGE COUNT |
|---|---|---|---|
| Annual | FROM 10/1/86 TO 10/1/87 | 11/15/87 | 136 |

16. SUPPLEMENTARY NOTATION

| 17. COSATI CODES | | | 18. SUBJECT TERMS (Continue on reverse if necessary and identify by block number) |
|---|---|---|---|
| FIELD | GROUP | SUB-GROUP | |
| | | | |
| | | | |

19. ABSTRACT (Continue on reverse if necessary and identify by block number)

This report covers the first year of operation of the URI Thin Film Center (TFC), and describes a diverse array of studies on thin-film materials, substrates, and their processing and analysis. Individual efforts are highlighted in sections on nucleation studies, ion-assisted deposition, Rutherford backscattering spectrometry, Brillouin scattering, a continuum theory of the evolution of structure in thin films, a study of polishing parameters relevant to the preparation of substrates, and the setup of a characterization facility for the Center.

| 20. DISTRIBUTION / AVAILABILITY OF ABSTRACT | 21. ABSTRACT SECURITY CLASSIFICATION |
|---|---|
| ☒ UNCLASSIFIED/UNLIMITED ☐ SAME AS RPT. ☐ DTIC USERS | Unclassified |
| 22a. NAME OF RESPONSIBLE INDIVIDUAL: Malloy | 22b. TELEPHONE (Include Area Code): 202 767-4931 |
| | 22c. OFFICE SYMBOL: NE |

DD FORM 1473, 84 MAR — 83 APR edition may be used until exhausted. All other editions are obsolete.

SECURITY CLASSIFICATION OF THIS PAGE

UNCLASSIFIED

AFOSR-TR- 88-0136

Prepared for
Air Force Office of Scientific Research
under the
University Research Initiative Program

# CENTER FOR THIN FILM STUDIES

## ANNUAL REPORT

Robert R. Shannon
Optical Sciences Center
University of Arizona
Tucson, Arizona 85721

November 15, 1987

88 2 26 128

## CONTENTS




DTIC COPY INSPECTED

ion For
RA&I
B
nced
cation
tion/
lity Codes
il and/or
Special
A-1

## INTRODUCTION

The Center for Thin Film Studies was formed in 1986 under grant from the Air Force Office of Scientific Research as part of the University Research Initiative Program (URIP).

This report covers the first year of operation of the URI Thin Film Center (TFC), and describes a diverse array of studies on thin-film materials, substrates, and their processing and analysis. Individual efforts are highlighted in sections on nucleation studies, ion-assisted deposition, Rutherford backscattering spectrometry, Brillouin scattering, a continuum theory of the evolution of structure in thin films, a study of polishing parameters relevant to the preparation of substrates, and the setup of a characterization facility for the Center.

The work described herein was performed under Contract # F49620-86-C-0123P00001.

TASK 1

# THIN-FILM NUCLEATION STUDIES: CONVENTIONAL AND ATOMIC LAYER EVAPORATION

Principal Investigator: U. J. Gibson

## Project Goal

Study the growth of thin films produced by different deposition methods, and correlate nucleation behavior with the development of film microstructure.

## Summary

During the first year of the project, we investigated ZnS made under varying conditions, made preliminary measurements of substrate-nucleation effects in ZnS deposited on Si, and designed and assembled (minus one piece) a preparation chamber to allow detailed nucleation studies under ultra-high vacuum (UHV) conditions. The experiments performed, equipment status, and plans for the coming year are discussed below.

## Work Accomplished

### *Film Growth*

Thin films of ZnS have been prepared by resistive evaporation in a conventional system under varying deposition conditions, and by molecular beam evaporation (MBE) onto both single crystal and amorphous substrates. These films have been studied with a wide variety of techniques, including x-ray diffraction, waveguide loss measurements, second-harmonic generation, and Brillouin scattering.

In a diffusion-pumped system, we found wide variations in the structure of ZnS deposited onto silica substrates under different conditions. Some of these changes (e.g., increased grain size with increased substrate temperature) can be readily predicted on the basis of simple film-growth models. In addition, we found strong

variations in optical properties and crystal structure of the films with changes of the residual gas composition. In particular, we found that residual oxygen in the system could reduce absorptive losses of the material, while changes in the $H_2O$ partial pressure produced dramatic changes in the preferred orientation and size of crystallites in films deposited onto ambient temperature substrates. Changing the $H_2O$ partial pressure from $3\times10^{-6}$ to $4\times10^{-7}$ torr changed the preferred orientation from (111) to (220) parallel to the substrate, and the sizes of the dominant-orientation grains from about 130 Å to greater than 250 Å. These changes strongly affect the waveguide losses of these materials,[1] as shown in Fig. 1.

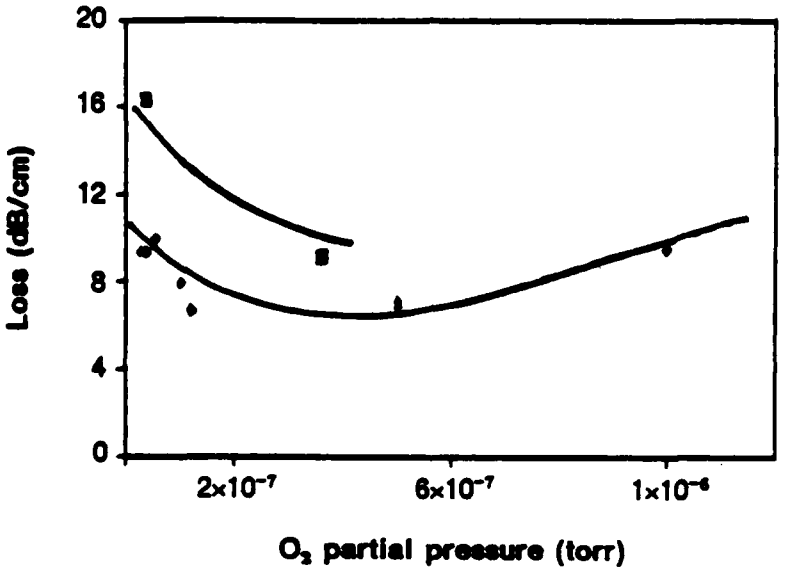


*Figure 1. Propagation loss dependence on $O_2$ partial pressure during deposition. Squares and diamonds represent $H_2O$ partial pressures of $4\times10^{-7}$ torr and $3\times10^{-6}$ torr respectively.*

MBE growth of ZnS onto Si substrates resulted in high-quality crystalline films, as determined by x-ray diffraction. Recent Brillouin measurements indicate the presence of an acoustical mode analogous to that found in ZnSe (refer to the discussion in the Task 3 report).

Second harmonic (SH) measurements on ZnS films are also underway to assess the effect of vapor impingement angle on the structure of the films. Previous results on alumina films indicate that SH is an extremely sensitive function of film anisotropy.[2]

*Nucleation Studies*

One of the goals of this project is investigation of atomic layer evaporation (ALE), where reactive pulses are brought to a substrate sequentially. In the growth of ZnS, possible reactants are Zn and thermally decomposed $H_2S$. Preliminary experiments have been performed to characterize the interaction of thin layers of Zn deposited onto Si surfaces. Equivalent thickness layers (as measured by a quartz crystal monitor) deposited onto different substrates gave widely varying x-ray photoelectron spectroscopy (XPS) signals, indicating different nucleation behaviors.

MBE layers of ZnS grown on etched and oxygen-passivated Si wafers indicated that heating the wafers in the presence of an $H_2S$ flux prior to deposition improved film properties, probably due to a Si-S layer created via an O-S surface exchange reaction. Two sets of experiments were performed on a thin Zn layer deposited onto Si prepared in this fashion. The first was on the evolution of the Zn signal with increasing temperature, and the second was angle-resolved photoemission to determine the nucleation behavior of the Zn.

The first set of experiments was used to study the appropriate temperatures for ALE using elemental Zn. Increases in the evaporation rate are expected at: a) the Zn-Zn bond energy equivalent, where Zn will evaporate from the exposed surface, and b) the temperature equivalent of the Zn-substrate bond energy. We observed slope variations at approximately 275°C and 550°C, corresponding to these thresholds.

Angle-resolved measurements were used to test the hypothesis that sulfur treatment of the Si surface led to formation of a complete monolayer as opposed to clusters of Zn. Although the analysis is complicated by spurious oxygen arising from the transfer of the sample from the deposition system to the XPS system, the results (Fig. 2) are convincing indications that the Zn does form an unbroken layer, suitable for ALE growth.

*Hardware*

Design and acquisition of almost all the pieces of the treatment chamber to be attached to the XPS system have been completed, although we still need the transfer rod (ordered in February, 1986). The configuration is shown in Fig 3. An ultraviolet source is presently being added to the surface analysis system.

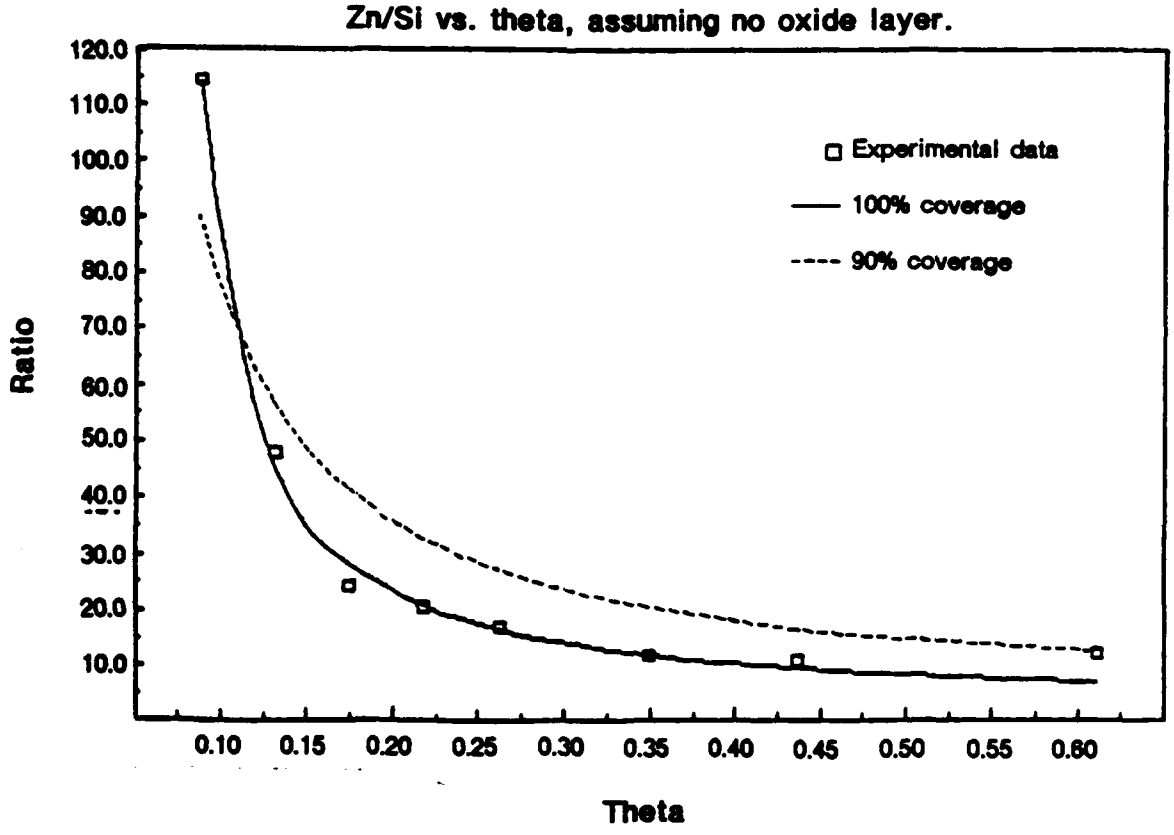


*Figure 2. Comparison of theoretical fit with actual data for Zn/Si (99eV) area ratio.*

Collaboration with Dr. Dereniak's group will allow us to assess the possibility of adding a scanning tunnelling microscope to the system; a flange for that purpose is on the chamber.

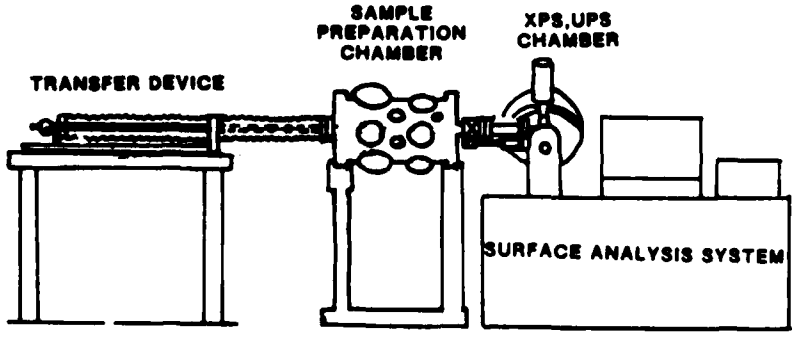


*Figure 3. Configuration of the XPS system treatment chamber.*

## Plans for the Coming Year

The plans for the coming year center around the new deposition chamber, which will allow us to perform UHV experiments on the nucleation behavior of MBE and ALE films. Sequential deposition and analysis steps will be possible between the two halves of the system. Specific studies to be undertaken include ion activation of the Si surface, and more detailed studies of the $H_2S$-prepared Si substrates. Further studies of thick samples grown by MBE in the other chamber are also planned, both in collaboration with Dr. Stegeman's lab, and using the expanding capabilities of the characterization facility.

## References


1. M. D. Himel, J. A. Ruffner, and U. J. Gibson, "Propagation Losses of Thin Film Waveguides," Proc. SPIE, 836, in press.
2. V. Mizrahi, F. Suits, J. E. Sipe, U. J. Gibson, and G. I. Stegeman, Appl. Phys. Lett., 51, 427 (1987).


## Personnel

U. J. Gibson
C. F. Hickey
J. Watanabe
F. Suits

## Collaborations

Hillebrands and Stegeman: Brillouin studies of ZnS.
Himel & Ruffner: Waveguide loss of films.
Gabel, Sasian, and Himel: Waveguide studies of polished surfaces.
Leavitt and Sasian: RBS studies of ceria-polished substrates.
Leavitt: RBS analysis of films.

TASK 2A

## STRUCTURE MODIFICATION BY ION-ASSISTED DEPOSITION

Principal Investigators: H. A. Macleod and M. R. Jacobson

### Project Goals

Investigate the use of ion-assisted deposition (IAD) for modification of film structure, and determine its utility for improving the performance of optical films.

### Summary

Progress on the URIP contract has been concentrated in four areas, as listed above in the section on project goals. The following sections deal with each of these areas separately, but it should be noted that there was significant interaction between these projects; for example, the IAD work relied heavily on RBS analysis at the Ion Beam Analysis Facility and on other characterization methods provided by the Measurement Laboratory. We point out here that unless otherwise noted, the coatings studied were deposited in the Balzers 760 evaporation system. This cryo-pumped box coater achieves base pressures of about $2\times10^{-6}$ mbar, and is equipped with a Commonwealth Scientific 3-cm Kaufman hot-cathode ion source.

### Work Accomplished

*Ion-Assisted Deposition of Oxides, Nitrides, Oxynitrides, Fluorides, and Metals*

Extensive IAD work has been carried out on metal oxide, oxynitrides, nitrides, and fluorides, and on metals, with considerable success. Parameters that have been varied include beam current and voltage, ion beam duty cycle (continuous and intermittent bombardment), and bombardment gas species (helium, neon, argon, and krypton, as well as oxygen and nitrogen). Summaries of the results for these materials follow.

## Metal Oxides - Alumina and Titania

Bombardment of alumina by both oxygen and argon ions was conducted largely to investigate the unusual behavior noted in a previous study by Ebert.[1] Alumina exhibits a very high packing density for oxide films, even when deposited on ambient temperature substrates. This is shown by the lack of a measurable vacuum-to-air shift in optical properties (comparison between properties immediately after deposition while still under vacuum and after venting to atmospheric pressure). The fact that no shift occurred, even for low index samples, indicates that alumina is dense enough to preclude moisture penetration. Our results also emphasize the importance of oxygen partial pressure on both unbombarded and bombarded coatings. We noted a strong increase in index with IAD, up to 1.70 at 350 nm, without any correlation to or change in density. The films were clearly amorphous according to x-ray diffraction (XRD) and transmission electron microscope (TEM) measurements; changes in index are presumably caused by alterations in the amorphous network, rather than in crystallinity. Ar bombardment increased, while O bombardment decreased absorption; we believe that O atoms can fill vacancies without adding impurities. Finally, the Kaufman guns cannot provide long-term O bombardment due to oxidation of their filaments. Cold cathode or filament-free Kaufman guns may be preferable.

Intermittent oxygen ion bombardment of titania films was attempted, to determine whether it could approach the increased refractive index and decreased absorption achieved in continuously bombarded films. The experiment was performed in the Balzers 760 chamber, with the substrates rotating through a 300 V ion beam from the ion gun while accumulating material from thermally evaporated $Ti_2O_3$ tablets. The results were positive, with the optical constants reaching values reported by others for the IAD of titania.

## Metal Nitrides - Aluminum Nitride

We compared two possible means of producing AlN: reactive evaporation of Al in an $N_2$ atmosphere, and IAD bombardment of thermally evaporated Al by a neutralized N ion beam. The former did not succeed in incorporating N into the film, but under the right conditions, the latter yielded stoichiometric AlN, or even superstoichiometric $AlN_x$, with x as high as 1.5! We believe that the N atoms were implanted, the bombardment stimulated $N_2$ sorption, or that the N atoms in the plasma were somehow activated with respect to neutral $N_2$.

Films with $x \geq 1$ were dielectric, but had considerable visible absorption.

Annealing at 500°C reduced the absorption and moved it toward the UV, presumably by permitting interstitial N to diffuse from the film or O to fill N vacancies. $AlN_x$ films with x as low as 0.5 were also produced, but these were two-phase films, with transparent and opaque crystallites alternating throughout the film on a scale of a few $\mu$m. For this work, the 3-cm gun was marginally able to bombard the sample; the 12-cm gun purchased this year with URIP funds will enable us to further explore this method.

### Metal Oxynitrides - Aluminum Oxynitride

We explored the possibilities of tailoring the index of AlN by bombarding thermally evaporated Al film with N in an $O_2$ atmosphere. This highly hybrid reactive IAD approach yielded films ranging in index from 1.65 to 1.93, depending on the ion-gun current density. In addition, absorption was systematically lower. We believe that oxygen fills the vacancies left by N bombardment.

### Metal Fluorides - Cryolite and Magnesium, Aluminum, Lanthanum, Cerium, and Neodymium Fluorides

Despite the differences among the many metal fluorides deposited, our work produced these general conclusions. First, IAD tends to sputter fluorine atoms preferentially, resulting in substoichiometric films. Second, the resulting vacancies are often filled with O or $OH^-$, which are available from residual water vapor or from implantation if O ion bombardment is employed. Visible absorption will be minimal if enough O is available to fill these vacancies, but some UV absorption characteristics of these metal oxides will appear. However, if preferential sputtering creates too many vacancies to fill, we observe visible and UV absorption.

Refractive index and packing density tend to increase under IAD. Other related properties change as well: vacuum-to-air shifts, water absorption bands, and tensile stress decrease. While these quantities can approach bulk values during more intense IAD, there is a point at which growing film absorption begins to undermine these improvements. We have also noted that crystalline fluorides ($LaF_3$, $CeF_3$, and $NdF_3$) will transform from fluoride to oxyfluoride phases when O content reaches a high level.

Tungsten filament erosion in the ion gun measurably contaminated the films, according to RBS measurements. The contamination did not seem to affect the optical properties.

### Metals

The IAD of metals has been studied much less than the IAD of dielectrics. In the interests of rectifying this neglect, Chang-Kwon Hwangbo began an investigation of the IAD of Ag. In general, Ag films are deposited with significant tensile stress. IAD with Ar tends to reduce this stress, and even leave the stress compressive. The effect appears to be proportional to ion beam momentum, rather than beam energy or current density. Momentum also correlates with changes in optical constants, lattice spacing, electrical resistivity, and incorporation of Ar ions.

### *RBS Analysis Techniques*

During the past year, we have worked extensively with Prof. J. Leavitt, director of the Ion Beam Analysis Facility (IBAF) at the University of Arizona Physics Department. There, a large Van de Graaff accelerator, described elsewhere in this report, provides a well-characterized, high-current ion beam for analysis of surfaces. Our main effort has been the derivation of a correction for heavier elements (high-Z correction) to their absolute Rutherford scattering cross-sections ($\sigma$). The conventional calculation of $\sigma$ ignores the effect of the electrons, simplifying the encounter to a simple two-body collision. This approximation holds very well at high collisional energies (> 3 MeV) and/or low atomic number for the bombarded atom. However, for high-Z elements and energies below 3 MeV, a common situation in RBS, $\sigma$ must be corrected to account for electron shielding of the nucleus, which effectively reduces the nuclear charge experienced by the incoming particle.

The high-Z correction is not critical for collisions between particles of similar atomic numbers, but becomes important when the particles are separated by more than a row in the periodic table. If the correction is ignored, the error may exceed the normally quoted precision of the technique. Moreover, computations of atomic densities from RBS data must include the correction regardless of the magnitude of the atomic mass variations. We have verified the importance of the high-Z correction in both regards.

In a related area, we produced an analysis program for IBM-PC standard microcomputers to expedite RBS analysis.

### *Simulation of Thermal and Growth Processes*

Although explicit funding for this area begins in October, 1987, we have

carried out some work with the assistance of Robert Sargent, who is supported by a Kodak Fellowship. He vastly improved the model code, and has modified it to run on the MicroVax computer here at the Center. The results have been applied to models of defect propagation and multilayer deposition. In addition, we also began theoretical work in thermal modeling while partially supported by this contract, and organized an SPIE Symposium on the topic of computer simulation of the growth of thin films for the 1987 Annual Meeting in August.

*Characterization Facility*

In the interests of assembing a central characterization facility, we have successfully solicited the donation of a Cary 2415 spectrophotometer from the Varian Corporation. This instrument, along with the upgraded Fourier transform infrared (FTIR) spectrophotometer, will complement the electron microscopes and WYKO surface profilometer obtained for the characterization facility.

## Plans for the Coming Year

*Ion-Assisted Deposition of Oxides, Nitrides, Oxynitrides, Fluorides, and Metals*

IAD will continue to be the area of concentration in the second year. We plan to work on a number of problems which were briefly investigated during the first year:

* Commissioning of the 12-cm ion gun - because of long delays related to bidding and Arizona law, we did not receive the 12-cm gun and its power supply until September. We are currently installing it in the Balzers 760, and it will be available during the coming months to enhance the size and uniformity of our ion beam for several experiments.

* Dual ion beam experiments - the arrival of the new gun allows us to begin experiments where the smaller gun can ion sputter source or target material and the larger gun can bombard the growing film. Such dual ion beam capability will multiply the parameters under our control during deposition.

* Intermittent bombardment - preliminary work indicates that intermittent bombardment of titania yielded improvements similar to those of continuous bombardment.

We intend to extend this work to other materials:

* Angular dependence - we will investigate whether the angle at which bombarding particles arrive at the substrate affects the ultimate properties of the coating.

* Exotic gas bombardment - while argon is the common gas employed for IAD, due to its moderate mass and low price, it is possible to bombard the film with other noble gases and nitrogen to permit variation of momentum independently of energy. Preliminary results with He, Ne, and Kr indicate clear index dependences on momentum rather than energy.

* Materials: similar oxides, nitrides and fluorides will be deposited this year. For metal films, we will embark on a program of Al deposition. It is known that Al, in contrast to Ag, is ion-beam sputtered in a compressive state. As we have done for Ag, we will compute optical constants with the surface plasmon resonance technique, determine microstructural properties with XRD, measure electrical resistivity with the four-point probe, and derive stoichiometry with the RBS technique. It has also been discovered recently that silver can be efficienlty oxidized in a plasma, so that oxygen bombardment of silver may be expected to yield some interesting materials.

*RBS Analysis Techniques*

We will continue to subject our samples to RBS analysis and to improve the technique:

* Better elemental resolution - the ongoing work at the RBS facility to double the beam energy to over 10 MeV by doubly ionizing the projectile nuclei should be completed this year. Under certain conditions, this can be used to simplify elemental identification by reducing overlap between peaks, producing higher resolution between elements in thicker films. This improvement will be applied immediately to the analysis program.

* Nuclear reaction analysis for H profiling - we will also participate in employing the nuclear reaction analysis (NRA) capability that the IBAF intends to complete this year. To probe the distribution of hydrogen with depth, the most difficult atom to observe for most techniques, a $^{15}N$ projectile nucleus is accelerated to an energy of 6.4 MeV to 10 MeV. The $^{15}N$ nuclei react with hydrogen atoms and produce a $^{12}C$ nucleus, an $\alpha$ particle, and a 4.43 MeV $\gamma$-ray. The resonance can be

easily observed. The method is especially valuable in profiling water in surface layers. Since $H_2$ molecules are rare in the atmosphere, we can attribute observed H either to $H_2O$ or to $OH^-$ which has been physisorbed or chemisorbed to the film surface. By comparing H and O results, we can assign the observed O to either $H_2O$ or free $O_2$. Depth profiling of H will also permit us to judge whether water is trapped deep in the film during deposition or whether it diffuses downward after post-deposition adsorption.

* Program improvement - we will continue to improve our computer program for RBS analysis.

*Simulation of Thermal and Growth Processes*

With the computer model vastly improved, a number of problems will be addressed in the coming year:

* Two element films - the program has been modified to allow particles of different sizes to be deposited.

* Defect propagation - periodic or irregular defects can be introduced at the substrate or at higher levels in the growing film; the consequences on further growth can be assessed.

* Potentials - most important, the simulation has been made much more realistic by the inclusion of a potential function that will influence the behavior of adatoms as they approach the surface.

*Characterization Facility*

As in the past year, the Measurement Laboratory will serve the needs of research groups in the Thin Film Center. The new spectrophotometer will increase the efficiency of our measurements and the accessibility of our data. Our plans for the coming year include:

* Absolute reflectance accessory - we intend to purchase an accessory for the Varian 2415 that will allow us to measure absolute reflectance with high accuracy.

* Electron microscopy - we will submit many of our samples to analysis in our new electron microscope facilities. We also will continue our collaboration with the Thin Film Group at Marseilles and the National Electron Microscopy Laboratory at Arizona State University in Tempe, Arizona.

**Publications citing the URIP program**

J. P. Lehan, J. D. Targove, B. G. Bovard, L. J. Lingg, M. J. Messerly, and H. A. Macleod, "Intermittent Ion Bombardment of Titanium Dioxide Thin Films," Appl. Opt., to be published. (Attached as Appendix A.)

J. D. Targove, "The Ion-Assisted Deposition of Optical Thin Films," Ph.D. Dissertation, University of Arizona, 1987. (Available on request.)

*Related Publications*

Papers:

B. J. Bartholomeusz, K-H. Muller, and M. R. Jacobson, "Computer Simulation of the Nucleation and Growth of Optical Coatings," Proc. SPIE 821, to be published.

B. G. Bovard and H. A. Macleod, "Non-Linear Behavior of Optical Coatings Subjected to Intense Laser Irradiation," submitted to J. Mod. Opt.

R. Sargent and H. A. Macleod, "Computer Simulation of the Growth of Two-Element Films," Proc. SPIE 821, to be published.

R. Sargent and H. A. Macleod, "Computer Simulation of Substrate Defect Propagation in Thin Films," Proc. SPIE 821, to be published.

J. D. Targove, J. P. Lehan, L. J. Lingg, H. A. Macleod, J. A. Leavitt, and L. C. McIntyre, Jr., Appl. Opt. 26, 3733 (1987).

Presentations:

B. G. Bovard and H. A. Macleod, "Thermo-Optical Modeling of Multilayer Optical Thin Films Subjected to Laser Irradiation," at the 1987 Annual Meeting of the Optical Society of America, Rochester, NY, October 19-23.

C-K. Hwangbo, L. J. Lingg, J. P. Lehan, J. D. Targove, M. R. Jacobson, H. A. Macleod, and J. L. Makous, "Ion-Assisted Deposition of Thermally Evaporated Ag Films," at the 1987 Annual Meeting of the Optical Society of America, Rochester, NY, October 19-23.

R. B. Sargent and H. A. Macleod, "Thin Film Growth Modeling," at the 1987 Annual Meeting of the Optical Society of America, Rochester, NY, October 19-23.

J. D. Targove, M. J. Messerly, and H. A. Macleod, "Ion-Assisted Deposition of $Al_2O_3$ Films," at the 1987 Annual Meeting of the Optical Society of America, Rochester, NY, October 19-23.

F. Varnier, C. Boulestix, J. D. Targove, L. J. Lingg, B. G. Bovard, and H. A. Macleod, "Influence of Ion-Assisted Deposition on Structure and Surface Roughness of Aluminum Oxide," at the 1987 Annual Meeting of the Optical Society of America, Rochester, NY, October 19-23.

Dissertation:

M. J. Messerly, "Ion-Beam Analysis of Optical Coatings," Ph.D. Dissertation, University of Arizona, 1987.

**Personnel**

Faculty:

H. A. Macleod

M. R. Jacobson

B. G. Bovard

Staff:

R. H. Potoff

S. Rana

A. McKew

Graduate Students:

L. J. Lingg

C-K. Hwangbo

J. P. Lehan

**Collaborations**

J. A. Leavitt and L. C. McIntyre, Jr., Physics Department, University of Arizona; RBS analysis of samples.

F. Varnier and C. Boulestix, University of Aix-Marseilles, Marseilles, France; electron microscopic investigations of surface topography.

**Reference**

1. J. Ebert, Proc. SPIE, 325, 29 (1982).

TASK 2B

## STRUCTURE MODIFICATION BY ION-ASSISTED DEPOSITION (ION-BEAM ANALYSIS OF THIN FILMS)

Principal Investigator: J. A. Leavitt

### Project Goals

A principal goal of this program is to provide accurate characterization using MeV ion-beam analysis (IBA) of thin films made by other Thin Film Center scientists. We use $^4He^+$ analysis ion beams, in the 1.5 MeV to 5.0 MeV energy range, from our 6 MV Van de Graaff accelerator to determine film thickness, stoichiometry, concentration profiles and crystalline structure by Rutherford backscattering (RBS), high-energy backscattering, and channeling.

Additional goals: development of apparatus for film characterization by nuclear reaction analysis (NRA) of hydrogen in thin films (using $^{15}N$ analysis beams), development of computer programs for data analysis, and investigation use of heavier-than-$^4He$ analysis beams for RBS.

### Work Accomplished

*Film Characterization*

1. During the period 9/9/86 to 10/29/87, we provided complete RBS analyses of at least 173 thin films provided by scientists associated with the Thin Film Center (TFC). In particular, we analyzed:

   a. 139 films for Dr. Macleod's group. Most of these films were fluorides of Nd, Al, Ce, Eu, Gd, La, Tb, Ho, Yb, Er, and Sm measured in connection with the use of ion-assisted deposition for modification of film structure; other films analyzed were AlN, AlNO, NaAlFO, and Ag.

b. 12 samples of silica polished with $CeO_3$ grinding compounds for Gibson/Parks; this investigation apparently produced no significant information concerning surface roughness.

c. 17 films with Au in $Al_2O_3$ for Suits/Gibson.

d. 3 films of SiC, 1 of Al with N implanted, and 1 of Ag for Salik.

e. 2 Nb/Cu superlattices for Bell/Stegeman; we provided stoichiometries of films presumably used for the Brillouin scattering studies.

A portion of the collaborative work with the Macleod group is described in the first-listed publication (manuscript attached as Appendix B).

2. During the period 2/9/87 to 10/29/87, we provided 87 additional complete backscattering analyses of films provided by C. Falco's group in Physics and D. Uhlmann's group in Materials Science, in connection with their attempts to develop superconducting films of the new high-temperature superconducting materials. Our analyses provided accurate film stoichiometries and thicknesses, as well as information on film-substrate interactions. Falco and J. Makous succeeded in making thin superconducting films of $Y_1Ba_2CU_3O_7$ with a transition temperature of 75 K (half-height) during August 1987, thus becoming the third university group in the country (after Stanford and Cornell) to produce high $T_c$ thin films. Our contribution to this work was described in a poster session, Oct. 1-2, 1987 at the Santa Fe meeting (second-listed publication, copy attached as Appendix C). Our contribution is also acknowledged in a joint publication of the Falco-Uhlmann groups (third-listed publication).

*Nuclear Reaction Analysis for Hydrogen Depth Profiling*

Use of NRA for $^1H$ depth profiling with $^{15}N$ analysis beams requires production of substantial beams of doubly ionized $^{15}N^{++}$ in order to cover the desired 6 MeV - 10 MeV energy region with our 6 MV accelerator. We tried both $^{15}N_2$ and $^{15}NH_3$ in our rf ion source and found that $^{15}N^{++}$ ions are not produced in sufficient quantity for practical hydrogen depth profiling. We concluded that our rf ion source should be replaced by a Penning source (which produces a larger fraction of highly charged ions). We acquired $10,715 from IBM-Tucson and bought a Penning source

and extraction electrode from General Ionex; at the time we did not have the funds for the recommended einzel lens and velocity selector to accompany the source.

We received the Penning source and electrode on 5/21/87. We built a 60 Hz bench-test facility and used it to obtain data to determine the best source operating conditions, as well as whether the additional components are necessary to convert our accelerator into a practical NRA device. As a result of the tests, we have concluded that we do need the additional components. We converted $10,295 in capital funds in our section of the TFC contract for purchase of the velocity selector and have acquired $6,910 from the Optical Data Storage Center for purchase of the einzel lens. These items were ordered 10/1/87. We anticipate installation in December 1987.

*Other*

1. We have continued work with heavier-than-$^4$He analysis beams to improve mass and depth resolution in RBS. Preliminary analysis of recent data obtained with C, Ar, and Kr analysis beams indicates no major improvement in mass and depth resolution will result from using the heavier beams.

2. We have continued to develop least-squares fitting programs for accurate deconvolution of overlapping backscattering peaks. We have checked the reliability of the results produced by the deconvolution by comparing with results obtained from data run at energies sufficient to produce separated peaks. See the fourth-listed publication below (manuscript attached as Appendix D).

3. On 10/23/87, a research briefing by J. Leavitt describing our work, entitled "MeV Ion Beam Analysis of Thin Films," was broadcast live, nationwide, by satellite. This briefing contained short discussions of analysis techniques, with illustrative examples from the fields of optical coatings, high $T_c$ superconducting films, optical data storage. A video tape of this one-hour briefing may be obtained from Microcampus, University of Arizona.

**Plans for Coming Year**

A. We plan to continue film characterization for our TFC collaborators (and others). We expect the sample load to increase considerably during the this next year as film-making plants commence operation.

B. We will exert a major effort starting in December 1987 to bring the $^{1}H$ depth profiling capability using $^{15}N$ beams on line. We expect to require approximately two months to get the Penning source installed and operating smoothly.

C. We plan to measure non-Rutherford cross sections for the scattering of He from light elements in the 2 MeV to 10 MeV region.

D. We expect to continue development of our computer fitting programs for improved data analysis.

**Publications**

J. D. Targove, L. J. Lingg, B. G. Bovard, J. P. Lehan, H. A. Macleod, J. A. Leavitt, and L. C. McIntyre, Jr., "Preparation of Aluminum Nitride and Oxynitride Thin Films by Ion-Assisted Deposition," to appear in MRS Symposia Proceedings - Materials Modification and Growth Using Ion Beams - Symposium C, 1987 Spring Meeting (copy attached, Appendix B).

Poster session paper:

J. A. Leavitt and L. C. McIntyre, Jr., "Stoichiometry of High $T_c$ Thin Films by High Energy Backscattering," at New Mexico Section MRS Conference on Developments in High-Temperature Supeconducting Materials, Oct. 1-2, 1987, Santa Fe, NM (copy attached, Appendix C).

Acknowledgment only:

J. L. Makous, L. Maritato, C. M. Falco, J. P. Cronin, G. P. Rajendraw, E. V. Uhlmann, and D. R. Uhlmann, "Superconducting and Structural Properties of Sputtered Thin Films of Y $Ba_2Cu_3O_{7-X}$," submitted to Appl. Phys. Lett.

L. C. McIntyre, Jr., M. D. Ashbaugh, and J. A. Leavitt, "Limits on Accuracy of Stoichiometry Determined by Rutherford Backscattering Using Computer Peak Fitting," to appear in MRS Symposia Proceedings - Materials Modification and Growth Using Ion Beams - Symposium C, 1987 Spring Meeting (copy attached, Appendix D).

**Video Tape:**

J. A. Leavitt, "MeV Ion Beam Analysis of Thin Films," National Technological University/University of Arizona Microcampus Research Seminar, live satellite broadcast/later video tape distribution, 60 minutes, Oct. 23, 1987 (video tape may be obtained from UA Microcampus).

**Personnel**

J. A. Leavitt
P. Stoss
M. D. Ashbaugh

**Collaborations**

All our work is collaborative. See collaborators listed above.

TASK 3

# A NOVEL TECHNIQUE FOR QUANTIFYING THE MECHANICAL PROPERTIES OF THIN FILMS

Principal Investigators: G. I. Stegeman and C. T. Seaton

## Project Goals

The principal objective of this task is to develop Brillouin scattering as a technique for measuring the elastic properties of thin films and interfaces. The work performed can be subdivided into two areas:

a) volume elastic properties of films and their modification;
b) interface-induced modifications of film properties.

## Summary

We developed the experimental tools and analysis techniques for determining elastic constants of films by Brillouin spectroscopy. Stonley and Love waves were observed for the first time with Brillouin scattering. The Stonley waves were used to compare the mechanical properties of a tantalum film at its air and substrate interfaces. The Love waves were used to measure the $c_{12}$ elastic constant for films for the first time. In addition, new longitudinally polarized thin-film guided waves were observed and used to determine (in some cases) the $c_{11}$ elastic constants with much higher precison than previously possible. Finally, modifications in the elastic constants upon polymerization of Langmuir-Blodgett films are being measured.

We have concentrated on modeling and measuring interface effects using Brillouin scattering. As a precursor to the experiments, we modeled theoretically the adhesion of thin films, and found acoustic dispersion characteristics sensitive to film adhesion. We measured films provided by IBM-Tucson to test the sensitivity of Brillouin scattering to interface stresses, without success. Similar investigations of metallic superlattices with large "interface densities" were successful. As a continuation of the interests of B. Hillebrands, we carried out Brillouin scattering

experiments on spin waves in magnetic films and superlattices. Interface magnetism, which reveals important information about the interdiffusion, electronic hybridization and/or polarization at interfaces, as well as about interface anisotropies was investigated.

## Work Accomplished

In the following sections we report the recent results of this project and outline future investigations.

### *Determination of Film Elastic Constants*

We developed computer programs for deducing elastic constants of thin films from experimentally obtained surface-phonon dispersion curves. The fitting procedure requires that the transverse sound velocity of the film be significantly smaller than that of the substrate, which normally can be achieved by a suitable choice of substrate material. The existing programs also require that the symmetries of the film and the substrate are at least tetragonal. Furthermore, at minimum, either the film or the substrate must be opaque. The best precision can be achieved for a sequence of films with thicknesses ranging from 100 Å to 5000 Å. However, in some special cases, the elastic constants could be obtained for single films. Elastic constants have been determined for ZnSe(001) films on GaAs(001),[1,2] CdA- and ODF-Langmuir-Blodgett films,[3,4] Ta films,[5] Cu/Nb,[6,7] and Fe/Pd films.[8,9] In many cases the total set of elastic constants was determined.

### *Evidence for the Existence of Guided Longitudinal Acoustic Phonons in ZnSe on GaAs*

We found theoretical as well as experimental evidence for a new class of long-wavelength acoustic film excitations which we identified as longitudinal guided acoustic phonons.[2] Despite their coupling to propagating transverse film modes at the film boundaries, these new modes have lifetimes comparable to the Rayleigh mode. They are the longitudinal counterpart of the well-known Lamb or Sezawa modes, with analogous existence criteria. The characteristic necessary for observation is a transparent film at least 1 $\mu$m thick, whose longitudinal sound velocities are smaller than those of the substrate. It is most important that these films permit a highly accurate determination of $c_{11}$ for the film, a parameter which is otherwise difficult to

evaluate. Since the displacement field of the modes is nearly completely polarized parallel to the film, the mode can also be used to monitor effects which modulate only dilatational waves.

*Elastic Properties of Metallic Films and Interfaces*

We studied Brillouin scattering from a number of metallic film systems, including tantalum films and Cu/Nb and Fe/Pd superlattices. Superlattices are very well suited for studying interface-related effects because of their large number of interfaces. We measured the elastic constants for Nb/Cu and Fe/Pd superlattices.[7,8] The elastic constants of Cu/Nb and Fe/Pd superlattices exhibit a large softening of $c_{11}$ for small modulation wavelengths. The results are indicative of the importance of the band-structure properties on the elastic properties. A hybridization of the electronic states at the interface and a corresponding modification of the density of states at the Fermi level in the interface region (hybridization length) presumably accounts for the observed behavior. A more quantitative understanding of the observed phenomena is strongly demanded.

The $c_{12}$ elastic constant of the Cu/Nb superlattice was obtained by measuring the Love acoustic modes supported by the film for the first time with Brillouin scattering.[6] The salient question is whether there is also a softening of the $c_{12}$ elastic constant with modulation wavelength. None was measured experimentally to within an accuracy of 10%.

Molybdenum films on sapphire substrates satisfy the conditions for the existence of Stonley waves.[5] These modes are highly localized at the film-substrate interface, in contrast to Rayleigh waves which are localized at the film-air interface. Measurements of the dispersion curves for these two modes on carefully prepared films showed that the tantalum film elastic constants at both film boundaries are essentially identical.

*Elastic Properties of CdA and ODF Langmuir-Blodgett Films and their Modifications upon Film Polymerization*

We studied the elastic properties of CdA-, saturated ODF- and unpolymerized and polymerized $\omega$-ODF- and ODF:ODM-Langmuir-Blodgett films.[3,4] Because of the laminar film structure consisting of parallel aligned, long molecules, which are

perpendicular to the interface and are tightly bound to each other, the films are elastically highly anisotropic and show generally an unusually small value of the transverse sound velocity, i.e., $c_{44}$. For CdA-Langmuir-Blodgett films, all of the elastic constants could be determined.[4] The first preliminary results for the ODF systems indicate a very puzzling behavior of the elastic constants upon polymerization: whereas the ODF:ODM films show a small stiffening of $c_{44}$ upon polymerization, the $\omega$-ODF samples show a decrease in the Rayleigh sound velocity and a slight stiffening of the Sezawa modes. This also indicates large modifications of the longitudinal sound velocity, which are not easily measured in a direct way. Future investigations should permit a more detailed understanding of the elastic properties of these films.

*Modeling Adhesion by Infinitely Thin Buffer Layers: New Long-Wavelength Acoustic Film Excitations*

We used computer simulations to study the influence of adhesion on the dispersion curves of long-wavelength film excitations. We modeled the interface as a very thin buffer layer, characterized by a vanishing transverse sound velocity. In regions where the dispersion curves show a nearly zero slope without a buffer layer, a new mode splits off in the presence of the buffer layer, which is reminiscent of the full symmetric mode of a free-standing film. Future investigations will show whether the predicted new modes can be found experimentally, and whether they will allow us to characterize adhesion.

*Characterization of Interface Stresses*

We attempted to measure the influence of interface stresses on elastic constants. For ZnSe films on GaAs it is known that interface stresses exist in a region up to 1 $\mu$m from the interface, before they are relaxed by the formation of dislocations. Since stress fields do not enter the acoustic equations of motion directly, the only means of detecting them with Brillouin spectroscopy is by a renormalization of the elastic constants due to higher-order terms. We could not find any thickness dependence of the elastic constants within the experimental accuracy of about 5% for this system.[1]

*Interface Magnetism*

In studies of the structural and electronic properties of interfaces, investigation of interface magnetism can shed light on many questions. In particular, the sensitivity of magnetic moments on impurities (interdiffusion) and on modifications of the electronic band structure (hybridization, charge transfer), as well as film growth-induced magnetic interface and volume anisotropies are excellent tools for the characterization of film properties.[9,10] Studying magnetism by measuring spin-wave spectra in a Brillouin scattering experiment allows a quantitative determination of the saturation magnetization, the g-factor, the exchange constant, volume and interface anisotropies, the interface interdiffusion range, and possible magnetic spacer polarizations. We observed and analyzed collective magnetostatic spin-wave excitations in magnetic Fe/Pd and Fe/W superlattices. For Fe/Pd, we found strong evidence for a magnetic polarization of the Pd spacer layers, as well as for a small negative out-of-plane interface anisotropy constant. The reference system Fe/W shows no pronounced anomalies.

This portion of the project was not part of the original program and represents an extension of previous interests for Dr. Burkard Hillebrands.

**Plans for the Coming Year**

The following investigations are tentatively scheduled for the coming year:

1. Characterization of the elastic properties of ZnS films.
2. Elastic properties of Langmuir-Blodgett films upon polymerization.
3. The adhesion problem.
4. Characterization of surface roughness by measuring surface phonons.
5. Characterization of magnetic interface properties.

Topic 1 is an application of the described new method for determination of transparent film elastic constants. Films grown in Task 1 by various methods will be characterized by Brillouin spectroscopy. Topic 2 is a continuation of the current investigations. In Topic 3 we will test our theoretical predictions. It is highly possible that the Langmuir-Blodgett films will provide good testing systems. Topic 4 is intended to check theoretical predictions about roughness-induced frequency renormalizations of the Rayleigh mode. The method will allow characterization of

roughness of highly corrugated surfaces on a length scale of surface-phonon wavelengths. In Topic 5 we will investigate in more detail the Fe/Pd interface and attempt to correlate the observed elastic and magnetic anomalies.

Further additional possibilities exist. In particular:

1. A search for a second surface mode on viscoelastic media.
2. Correlation of elastic film properties with material hardening and working, in collaboration with IBM-San Jose.

**Personnel**

G. I. Stegeman

B. Hillebrands

S. Lee

**Collaborations**

U. J. Gibson, UA - adhesion properties of thin films.

C. M. Falco, UA - preparation of superlattice samples.

J. E. Potts, 3M Company, St. Paul, MN - preparation of ZnSe samples.

J. Swalen, IBM, San Jose, CA - preparation of Langmuir-Blodgett films.

**References**


1. S. Lee, B. Hillebrands, G. I. Stegeman, H. Cheng, J. E. Potts, and F. Nizzoli, "Elastic Properties of Epitaxial ZnSe(001) Films on GaAs Measured by Brillouin Spectroscopy," submitted to J. Appl. Phys. (copy attached as Appendix E).

2. B. Hillebrands, S. Lee, G. I. Stegeman, H. Cheng, J. E. Potts, and F. Nizzoli, "Evidence for the Existence of Guided Longitudinal Acoustic Phonons in ZnSe Films on GaAs," submitted to Phys. Rev. Lett. (copy attached as Appendix F).

3. R. Zanoni, C. Naselli, J. Bell, G. I. Stegeman, and C. T. Seaton, Phys. Rev. Lett. 57, 2838 (1986).

4. B. Hillebrands, R. Zanoni, G. Stegeman, L. Laxhuber, and G. Swalen, to be published.

5. J. A. Bell, W. R. Bennett, R. Zanoni, G. I. Stegeman, C. M. Falco, and C. T. Seaton, "Brillouin Scattering from Love Waves in Cu/Nb Metallic Superlattices," Appl. Phys. Lett., in press.

6. J. A. Bell, W. R. Bennett, R. Zanoni, G. I. Stegeman, C. M. Falco, and C. T. Seaton, Appl. Phys. Lett., 51, 652 (1987).

7. J. A. Bell, W. R. Bennett, R. Zanoni, G. I. Stegeman, C. M. Falco, and C. T. Seaton, "Elastic Constants of Cu/Nb Superlattices," Solid State Comm., in press.

8. P. Baumgart, B. Hillebrands, R. Mock, G. Güntherodt, A. Boufelfel, and C. M. Falco, Phys. Rev. B 34, 9004 (1986).

9. B. Hillebrands, P. Baumgart, G. Güntherodt, Phys. Rev. B 36, 2450 (1987).

10. B. Hillebrands, A. Boufelfel, C. M. Falco, P. Baumgart, G. Güntherodt, E. Zirngiebl, and J. D. Thompson, "Brillouin Scattering from Collective Spin Waves in Magnetic Superlattices," J. Appl. Phys., in press. (copy attached, Appendix G).

TASK 4

## CONTINUUM MODEL OF FILM GROWTH

Principal Investigator: Seth Lichter

### Project Goal

Develop a theoretical continuum approach to modeling the microstructure of thin films.

### Summary

Most thin-film studies use a Monte-Carlo simulation of the deposition process. These models omit much of the relevant thermodynamics and dynamics which govern adatom mobility. This omission is necessitated by the complexity and size of the simulation. Those few simulations which account for particle-particle interactions are limited to extremely small grids.

Additionally, these simulations do not cope with another fundamental aspect of thin-film physics: the deposited film must satisfy some constitutive constraints as well as constraints on stress and strain.

It is our intention to pursue an alternative to the usual numerical computation. Rather than starting with numerical simulation, we will begin with a simulation of the governing physical processes. We will preserve the physics as much as possible, in the belief that a properly formulated model will yield correct results.

The one assumption common to all our work is that the continuum hypothesis can be applied. We recently applied this approach to a model of adatom mobility which gave an analytical basis for the tangent rule.[1] While that initial work focused on the deposition process, this complementary effort will focus on the equations describing the deformation of the film itself.

**Work Accomplished**

In our work, we have ignored the deposition process entirely, and have solved for possible equilibrium structures in the films. Ultimately we hope to use this model to predict the abrupt structural transitions catalogued by Movchan and Demchishin.[2] Our attempts in this area begin with analyses of one-dimensional deformable lattices. This work is in its initial stages.

Other work has centered on the motion of grain boundaries and, in particular, those conditions under which the grain boundaries could organize themselves into columnar microstructures. This work is still in the tentative stage, but we show below how a simple model, based on the usual equations of mechanical equilibrium in an elastic thin film, can be used to predict column size as a function of tensile stress in the film.

The three-dimensional displacements for an elastic body are governed by the equation

$$\rho \frac{\partial^2 u_i}{\partial t^2} = F_i + \mu u_{i,jj} + (\lambda + \mu)\, u_{j,ji} \,. \tag{1}$$

subject to the boundary conditions

$$u_i = f_i\,(x_i,\, t) \,. \tag{2}$$

where $f_i$ is continuous, $u_i$ is the displacement, $F_i$ is the body force, $\mu$ is the shear modulus, $\rho$ is the density, and the subscripts following a comma denote derivatives. We assume the flux of grain boundaries $B_i$ is proportional to the body force

$$B_i = D\, F_i \,. \tag{3}$$

where D is a proportionality constant. We further assume that the divergence of the flux of grain boundaries is compensated for by a creation C and an annihilation A of boundaries such that

$$-D\, \nabla^2 U = C - A \,. \tag{4}$$

Subtracting the elastic solution, restricting the force to lie in a thin plane in the $x_3$ direction, and after some calculation we find

$$\left[\rho \frac{\partial^2}{\partial t^2} - \mu \nabla^2\right] \nabla^2 u_3' = -\nabla_1^2 U_{,3}' \,. \tag{5a}$$

$$-D \nabla^2 U' = \beta u_{3,3}' \,. \tag{5b}$$

$$u_i' = f_i' \qquad \text{on the boundaries,} \tag{5c}$$

where the primes denote the total displacement minus the elastic displacement. A particular solution can be found by suppressing the time dependence. One approximate solution is then

$$w = w_0 \sin\left[a \left(\frac{\beta}{\mu D}\right)^{1/2} x_3\right] \,. \tag{6}$$

where $\beta$ and $w_0$ are constants and a is the characteristic horizontal wave number. As w has the same dependence on the applied stress as does the displacement due to motion of the grain boundaries, we find

$$\tau_{11} \propto a\left(\frac{\beta}{\mu D}\right)^{1/2} \,. \tag{7}$$

where $\tau_{11}$ is the stress. So the solution reveals a periodic array of grain boundaries. Such an array may delineate a row of the columnar microstructure. Furthermore, in this limit, the size of the columns is shown to be inversely proportional to the stress in the film.

## Plans for the Coming Year

This year we hope to show that the possible equilibrium solutions are dependent on the conditions in the film. In the above example the controlling parameter is film stress. The stress can be related to substrate temperature using energy considerations. In this manner we hope to establish the dependence of columnar microstructure on substrate temperature.

## Personnel

S. Lichter

J. Chen

## References

1. S. Lichter and J. Chen, Phys. Rev. Lett., 56, 1396 (1986).

2. B. A. Movchan and A. V. Demchishin, Phys. Met. Metall., 28, 83 (1969).

TASK 5

## ATOMISTIC MODELING OF FILM GROWTH

Principal Investigator: H. A. Macleod

### Project Goals

Use and expand an atomistic model of film growth to investigate the effects of ion bombardment, and substrate and interfacial roughness.

Develop a model to include the range of effects present in an actual coating chamber.

### Summary

The research under Task 5 is scheduled to begin in the second year of this project; preliminary results are described under Task 2A.

TASK 6

## SURFACES AND POLISHING STUDIES

Principal Investigators: R. E. Sumner and R. E. Parks

### Project Goals

An important aspect of the development of thin films is the manufacture and characterization of known substrates. The objectives of the research program in substrate production, conducted at the Optical Shop, are:

1. Define and quantify the different surface defects that may be present in a substrate surface.
2. Determine the surface quality achieved by different polishing procedures in a number of materials (glasses, crystals, and metals).
3. Define efficient polishing procedures to produce surfaces with a given quality, with special emphasis on the production of low-scatter, smooth surfaces.

### Work Accomplished

Goal 1.

Initial library research has been conducted.

An inspection optical microscope to identify visible surface defects has been installed.

A non-contact optical profilometer to measure surface roughness has been installed.

A scatterometer is under construction (see Fig. 1).

Goal 2.

As a preliminary step in designing the grinding and polishing procedures, some simple experiments, that is, observation of the grinding and polishing of quartz substrates, were conducted. The results of these experiments suggest criteria to consider during the grinding process, show how critical the cleaning of the samples may be when characterizing them, and also suggest that a variety of testing

instruments should be used to better characterize and understand the polishing process.

At this point in time some of the necessary materials have been ordered and received, quartz samples and their supports have been prepared, the milling of the polishing materials has been started, flat cast-iron grinding tools have been prepared, and a measurement table has been constructed to quantify material removal during the grinding process.

Two blocks of 19 quartz samples each have been ground and polished using two different procedures. Their characterization is under way. Two other blocks are being prepared.

Notes on the grinding and polishing procedures are being taken.

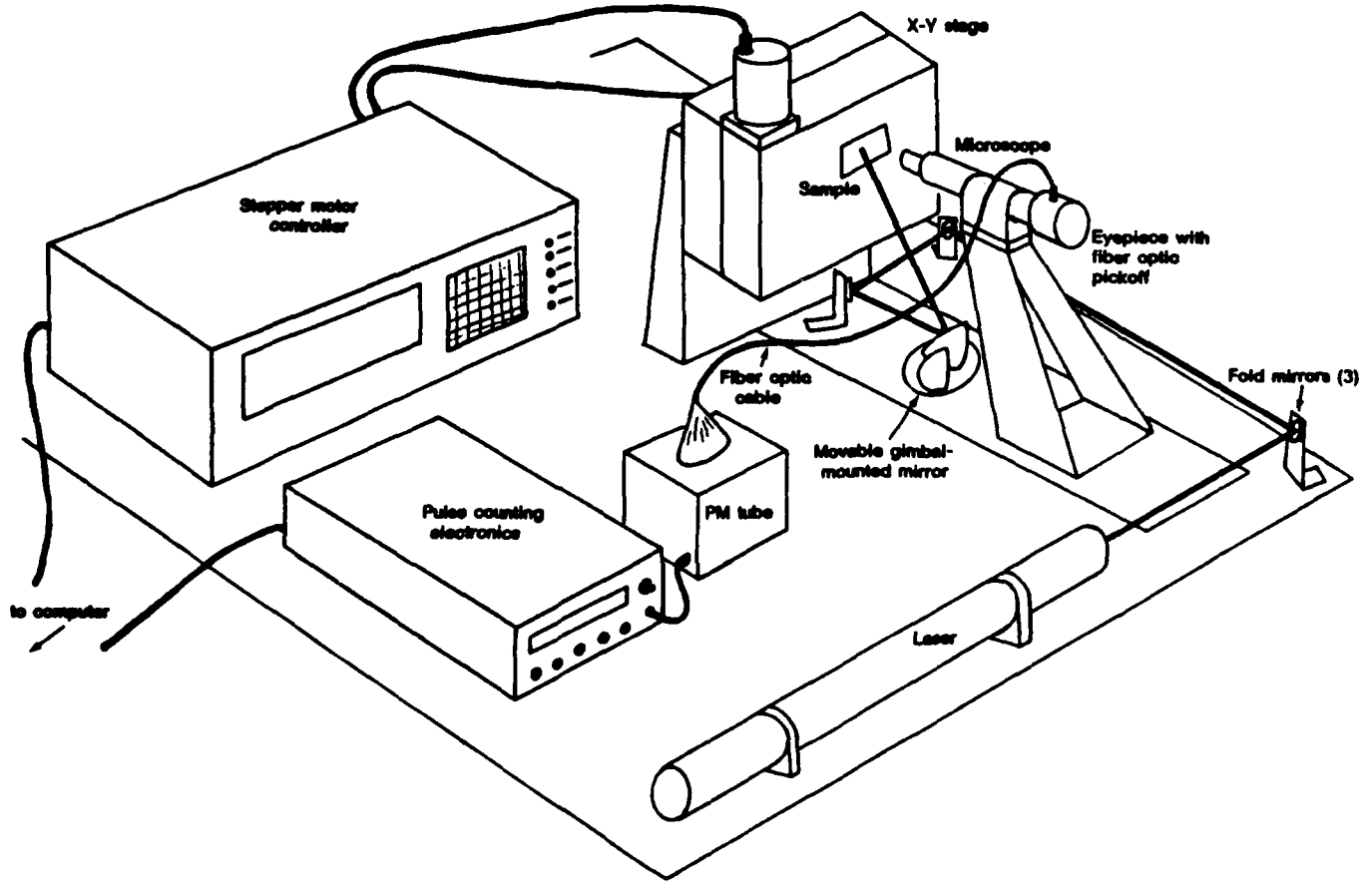


*Figure 1. A diagram of the scatterometer.*

## Plans for the Coming Year

Several blocks of quartz samples will be prepared using different polishing procedures.

Several blocks of BK-7 glass samples and crystal samples will be produced. Polishing procedures will be directed by past experience with the quartz samples.

The surface quality will be characterized for the blocks produced.

## Personnel

R. E. Summer
R. E. Parks
J. M. Sasian

## Collaborations

A number of glass substrates have been prepared for other members of the group.

TASK 7

## CHARACTERIZATION FACILITY

### Project Goal

Set up a central facility for characterization of thin films, surfaces, and substrates.

### Work Accomplished

Major equipment purchases and hiring of a full-time technician to oversee the facility were the major accomplishments in this year. The transmission electron microscope (TEM) and the scanning electron microscope (SEM) were installed in October, and the instruments are operational. Not all of the sample preparation equipment has been received. The WYKO profilometer has been operational for some time, and is being used for both thickness determinations and surface characterization. A series of seminars on the equipment capabilities and limitations is now underway.

A small effort was initiated under this task to tap local expertise on scanning tunneling microscopy. We expect that a vacuum-compatible working model will be completed in the next year.

### Acquisitions for Characterization Facility

1. JEOL 2000FX Transmission Electron Microscope:
   1.4 Å line resolution,
   bright field, dark field, diffraction, and nano-diffraction modes.

   Sample preparation equipment for TEM:
   ion thinner for cross-sectional samples,
   dimpler for cross-sectional samples,
   chemical jet thinner for cross-sectional samples,
   precision core drill for cross-sectional samples.

2. JEOL JSM-U3 Scanning Electron Microscope:
   60 Å resolution.

   Sample preparation equipment for SEM:
   sputter coater, target, etc.

3. WYKO 2-d heterodyne interferometer (on loan).

Other equipment:

4. Varian CARY 2415 spectrophotometer,
   donated to Dr. Macleod's Measurements Lab.

5. Scatterometer,
   built as part of Task 6.

**Personnel**

U. J. Gibson
V. Lindley
M. Kelley

# APPENDIX A

# Intermittent Ion Bombardment of Titanium Dioxide Thin Films

J. P. Lehan, J. D. Targove, B. G. Bovard, L. J. Lingg, M. J. Messerly, and H. A. Macleod

Titanium dioxide is important to the optical coating industry because of its high index; unfortunately, it is not easily deposited as stoichiometric $TiO_2$.[1] Oxygen deficiency in $TiO_2$ results in a broad absorption band, centered about 1.05 $\mu$m, first identified in single crystals by Cronemeyer[2] and later observed in evaporated films by Heitmann.[3] The conventional method of depositing $TiO_2$ (which refers to the oxides of Ti with stoichiometries near the desired $TiO_2$), is reactive evaporation onto a substrate heated to about 200°C or more[4] in an oxygen atmosphere to promote film oxidation. The elevated temperature hardens the coatings; however, it also increases absorption.[1] In addition, high temperatures preclude deposition on a variety of substrates, including plastics and high-precision optical flats. A low-temperature alternative to reactive evaporation is ion-assisted deposition (IAD), which is an effective method of improving the adhesion,[5] stress,[5] packing density,[6] and environmental stability[6] of a wide variety of coating materials. Martin,[7] McNeil,[8] and Allen[9] have reported on the IAD of $TiO_2$ films. These studies, however, along with most other work on the subject, deal with stationary substrates under a constant ion flux. This would not be the situation in a production environment, where planetary rotation ensures uniform coverage of many substrates. To employ IAD in such an environment, the ion beam must move synchronously with the substrates or the beam must extend far enough to immerse all of the substrates in a constant ion flux. Alternatively, the substrates can be rotated through a stationary smaller ion beam, making the bombardment intermittent. The last approach is the easiest and requires the least modification of an existing chamber.

---

J. P. Lehan, B. G. Bovard, L. J. Lingg, and H. A. Macleod are with the Optical Sciences Center, University of Arizona, Tucson, Arizona 85721. J. D. Targove and M. J. Messerly are both formerly with Optical Sciences. J. D. Targove is presently with the Air Force Institute of Technology, Department of Engineering Physics, Wright-Patterson AFB and M. J. Messerly is with 3M.

We investigated the consequences of intermittent ion bombardment on $TiO_2$ films as the substrate rotated through the ion beam. Cerac$^{TM}$ $Ti_2O_3$ tablets were electron-beam evaporated in a cryopumped Balzers BAK 760 box coater equipped with a 3-cm-aperture Commonwealth Scientific$^{TM}$ Kaufman hot-cathode ion source. We added oxygen to the chamber both through the ion gun and the side of the chamber as a neutral background species, to aid oxidation of the growing films. The deposition rate and film thickness were monitored by a quartz crystal oscillator. The transmittance and reflectance of the coatings were measured by a Cary 14 spectrophotometer. We computed the optical constants from the tramsmittance and reflectance profiles using an envelope calculation based on an inhomogeneous, weakly absorbing film model developed by Macleod.[18]

The chamber parameters during the deposition were

Substrate temperature: 25°C, rising to 150°C during deposition

Chamber base pressure: $2\times10^{-6}$ mbar

Added gases: $O_2$

Pressure: $8\times10^{-5}$ mbar admitted through the ion gun

$2\times10^{-4}$ mbar through the side of the chamber

Ion beam voltage: 300 V

Ion beam duty cycle: ≅50%

Evaporation rate: 4 Å/s

Ion gun-to-substrate distance (minimum): 38 cm.

The ion-beam center was aimed at the point recieving the maximum evaporant flux along the substrate's rotation path, which was directly over the electron beam crucible. Therefore, the maximum evaporant and ion fluxes coincided at the substrate. The ions impinged on the substrates at approximately normal incidence while the evaporant arrived at about 15° from the normal. Despite the small size of the ion-gun aperture, the resultant ion beam was very wide, about 60 cm full width at half-maximum current density as measured along the substrate rotation path. This curious effect is probably attributable to ion scattering from the relatively abundant oxygen in the chamber. At $3\times10^{-4}$ mbar and 125°C, the mean free path of an oxygen molecule is 13.7 cm, less than our ion gun-to-substrate distance of 38 cm. We later reduced our ion gun-to-substrate distance to 30 cm to reduce the scattering. The data were taken with 300 eV oxygen ions, as 500 eV ions damaged the films even at modest ion current densities.

The number of ions per arriving molecule, $\gamma$, has been postulated as the physically significant parameter for IAD.[9] With rotation of the substrates, however, $\gamma$ is a function of the substrate location. We thus propose that the time-averaged ratio, $\bar{\gamma}$, be substituted. To calculate $\bar{\gamma}$ we measured the ion-beam profile along the substrate rotation path with a Faraday cup biased at -45 V to repel the neutralizing electrons. The measured ion current density was then fitted to a function; the best fit to the measured data was found to be Lorentzian. The relationship between the current density and the measured evaporation rate allowed us to calculate $\bar{\gamma}$. Since our rotation was along a circular path and the rotation speed was constant, the ion flux was periodic and so averaged over a single period. Then

$$\bar{\gamma} = \frac{1}{2\pi} \int_0^{2\pi} \gamma(\theta) d\theta \ .$$

We assume that the radius is constant for the circular rotation and that $\gamma(\theta)$ is a best fit. This parameter correlated well with the observed changes in film properties whereas the peak in $\gamma(\theta)$ did not.

Because of the strong refractive-index inhomogeneity observed in some of our $TiO_2$ films, we report both an average index, $\bar{n}$, and the degree of inhomogeneity, $\Delta n/\bar{n}$. Figure 1 shows $\bar{n}$ at 550 nm as a function of $\bar{\gamma}$. Notice that, at an ion gun-to-substrate distance of 38 cm, $\bar{n}$ increases until it reaches a maximum at $\bar{\gamma} \cong 0.5$. At an ion gun-to-substrate distance of 30 cm, the slope of the curve is greater. This may be attributable to the reduced scattering of ions by the oxygen backfill. In Fig. 2, we plot the extinction coefficient, k, as a function of $\bar{\gamma}$. Here k is minimum in roughly the same $\bar{\gamma}$ region as the maximum in $\bar{n}$. Note that the film with $\bar{\gamma} \cong 0.4$ in Fig. 2 corresponds to an extinction coefficient value below the resolution of our spectrophotometric measurements and so was estimated for the plot.

Figure 3 plots $\Delta n/\bar{n}$ at 550 nm as a function of $\bar{\gamma}$. The inhomogeneity is taken as negative if the index *decreases* away from the substrate. The critical point demonstrated here is that the minimum degree of inhomogeneity occurs at $\bar{\gamma} \cong 0.4$, the same value that yielded a maximum in refractive index and a minimum in extinction coefficient. We also found that the dispersion of the degree of

inhomogeneity, $\Delta n/\bar{n}$ vs $\lambda$, is altered by intermittent IAD. At $\bar{\gamma} = 0.45$ we observed an approximately linear dispersion curve for the degree of inhomogeneity in the visible region of the spectrum described by the equation $\Delta n/\bar{n} = -0.00011\lambda$ (nm) + 0.0704.

We gain insight into the underlying physical processes if we examine the vacuum-to-air shift (the shift in the spectral profile as the evacuated chamber is brought up to atmospheric pressure) at a wavelength at which the optical thickness of the coating is an integral number of half wavelengths. If we assume that this shift is caused by water adsorption into the film pores,[7] this provides a rough measure of their porosity. Figure 4 plots the vacuum-to-air shift against $\bar{\gamma}$. For $\bar{\gamma}$ below 0.40, intermittent ion-assisted deposition does not densify the films significantly, but above this level some densification of the films occurs. Above $\bar{\gamma} \cong 0.45$, however, absorption rises steeply and index decreases.

Other analysis techniques included x-ray diffraction and x-ray photoelectron spectroscopy. The films showed no crystalline structure in our x-ray diffraction measurements. X-ray photoelectron spectroscopy of the samples showed no discernable shift in the Ti-O binding energy between slightly absorbing and nonabsorbing films. This indicates that the changes affecting optical absorption are small.

From the above data we propose the following model: As we increase the number of arriving oxygen ions, the number of oxygen vacancies decreases. As mentioned earlier, $TiO_2$ is known to be oxygen deficient when thermally evaporated. These oxygen vacancies are filled by chemically active oxygen ions absorbed at the substrate. This simultaneously increases the refractive index and decreases the extinction coefficient.

The filling of oxygen vacancies is a balance between opposing factors. This is demonstrated by examining the optical constants as a function of $\bar{\gamma}$. As $\bar{\gamma}$ increases from 0, we fill oxygen vacancies until with $0.40 \leq \bar{\gamma} \leq 0.45$, the vacancies have been saturated and the preferential sputtering of oxygen out of the film becomes significant. Although the sputtering yield is low for 300 eV ions at $\bar{\gamma} \geq 0.5$, the statistics begin to favor the preferential sputtering of oxygen from the surface of the growing film because the peak ion flux is so large and the Ti-O chemical bond in $TiO_2$ is weak.[11] Sputtering, a function of ion energy, should increase at higher ion

energy. Indeed, we noted that our films were damaged at a lower $\bar{\gamma}$ for 500 eV intermittent ion bombardment. This apparently occurs when the population of active oxygen at the substrate is below that needed to satisfy the oxygen deficiency.

In conclusion, intermittent ion bombardment can increase the refractive index and reduce the absorption of $TiO_2$ films. The range of refractive indices reported here is similar to that reported elsewhere[9] for IAD without substrate rotation. This demonstrates that IAD can be considered for production environments.

The authors would like to acknowledge the support of the Air Force Office of Scientific Research through the University Research Initiative Program.

1. J. Ebert, "Activated Reactive Evaporation," Proc. Soc. Photo-Opt. Instrum. Eng. 325, 29 (1982).

2. D. C. Cronemeyer, "Infrared Absorption of Reduced Rutile $TiO_2$ Single Crystals," Phys. Rev. A 113, 1222 (1959).

3. W. Heitmann, "Reactive Evaporation in Ionized Gases," Appl. Opt. 10, 2414 (1971).

4. H. K. Pulker, G. Paesold, and E. Ritter, "Refractive Indices of $TiO_2$ Films Produced by Reactive Evaporation of Various Titanium-Oxygen Phases," Appl. Opt. 15, 2986 (1976).

5. S. D. Jacobs, A. L. Hrycin, K. A. Cerqua, C. M. Kennemore III, and U. J. Gibson, "Adhesion Enhancements and Internal Stress in $MgF_2$ Films Deposited with an Ion Beam Assist," Thin Solid Films 144, 69 (1986).

6. P. J. Martin, R. P. Netterfield, and W. G. Sainty, "Modification of the Optical and Structural Properties of Dielectric $ZrO_2$ Films by Ion-Assisted Deposition," J. Appl. Phys. 55, 235 (1984).

7. P. J. Martin, H. A. Macleod, R. P. Netterfield, C. G. Pacey, and W. G. Sainty, "Ion-Beam-Assisted Deposition of Thin Films," Appl. Opt. 22, 178 (1983).

8. John R. McNeil, Alan C. Barron, S. R. Wilson, and W. C. Herrmann, Jr., "Ion-Assisted Deposition of Optical Thin Films: Low Energy vs High Energy Bombardment," Appl. Opt. 23, 552 (1984).

9. Thomas H. Allen, "Ion Assisted Deposition of Titania and Silica Films," Proc. Int'l Ion Engineering Congress - ISIAT'83 & IPAT'83, Kyoto 1305 (1983).

10. D. P. Arndt et al., "Multiple Determination of the Optical Constants of Thin-Film Coating Materials," Appl. Opt. 23, 3571 (1984).

11. Roger Kelly, "On the Problem of Whether Mass or Chemical Bonding is More Important to Bombardment-Induced Compositional Changes in Alloys and Oxides," Surface Science 100, 85 (1980).

## Figure Captions

Figure 1. Mean refractive index at 550 nm of $TiO_2$ films bombarded with 300 eV oxygen ions as a function of the average number of ions per arriving molecule. o - 38 cm from ion gun to optic. Δ - 30 cm from ion gun to optic.

Figure 2. Extinction coefficient at 550 nm of $TiO_2$ films bombarded with 300 eV oxygen ions as a function of the average number of ions per arriving molecule. o - 38 cm from ion gun to optic. Δ - 30 cm from ion gun to optic.

Figure 3. Relative inhomogeneity at 550 nm of $TiO_2$ films bombarded with 300 eV oxygen ions as a function of the average number of ions per arriving molecule. o - 38 cm from ion gun to optic. Δ - 30 cm from ion gun to optic.

Figure 4. Vacuum-to-air shift at 450 nm of $TiO_2$ films bombarded with 300 eV oxygen ions as a function of the average number of ions per arriving molecule. o - 38 cm from ion gun to optic. Δ - 30 cm from ion gun to optic.

figure 1

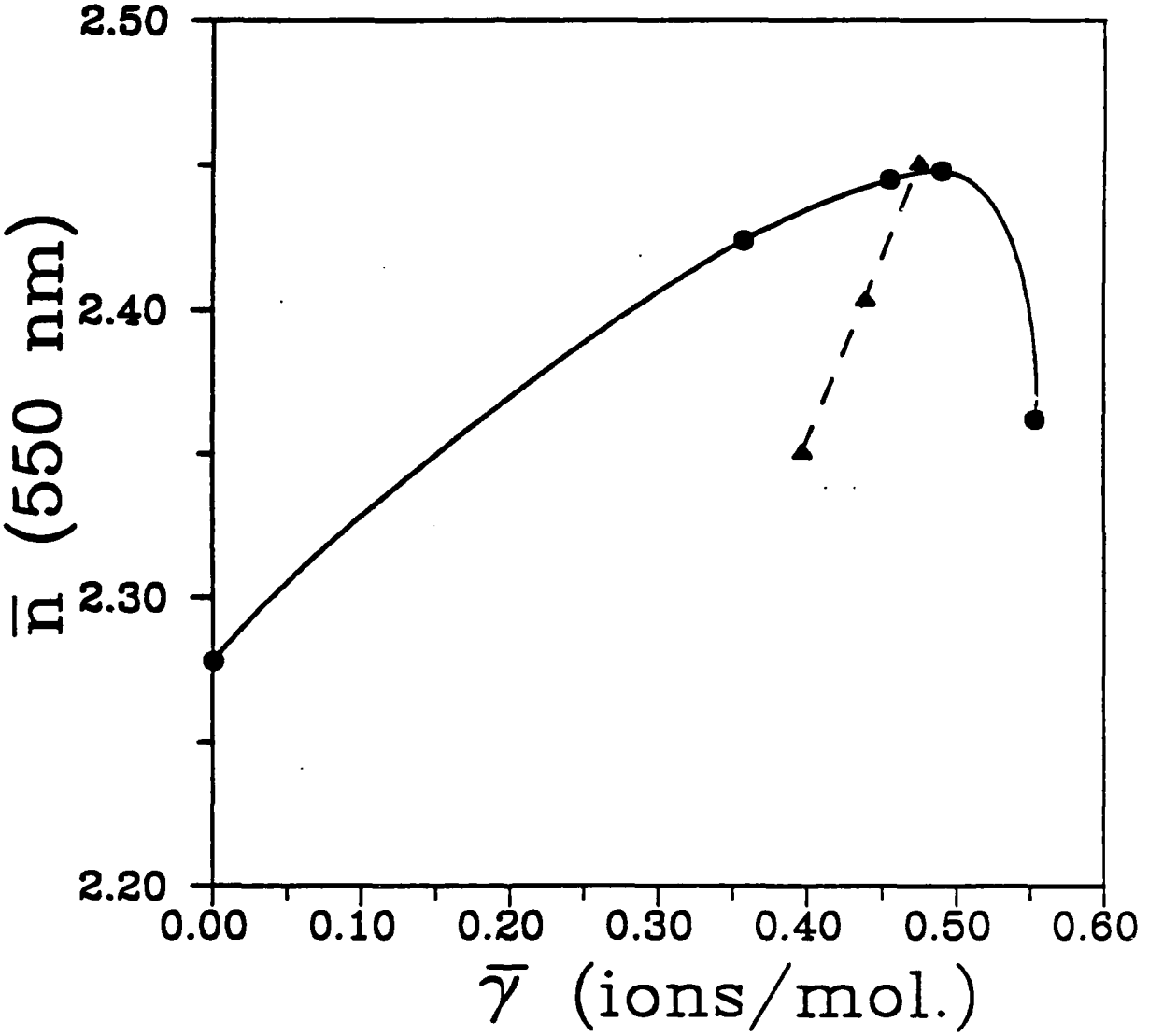
2.50
2.40
2.30
2.20
$\overline{n}$ (550 nm)
0.00
0.10
0.20
0.30
0.40
0.50
0.60
$\overline{\gamma}$ (ions/mol.)

figure 2

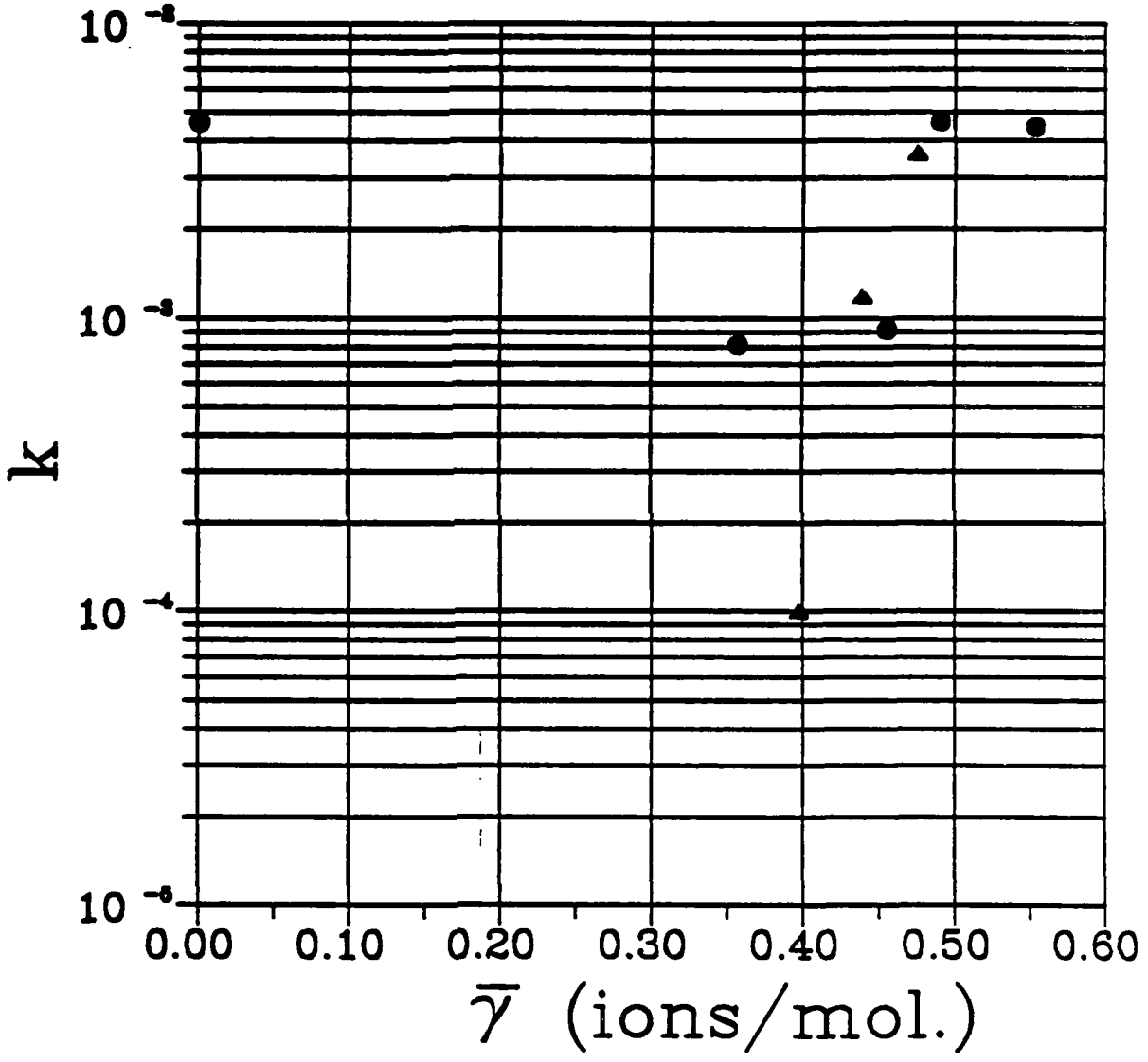

figure 3

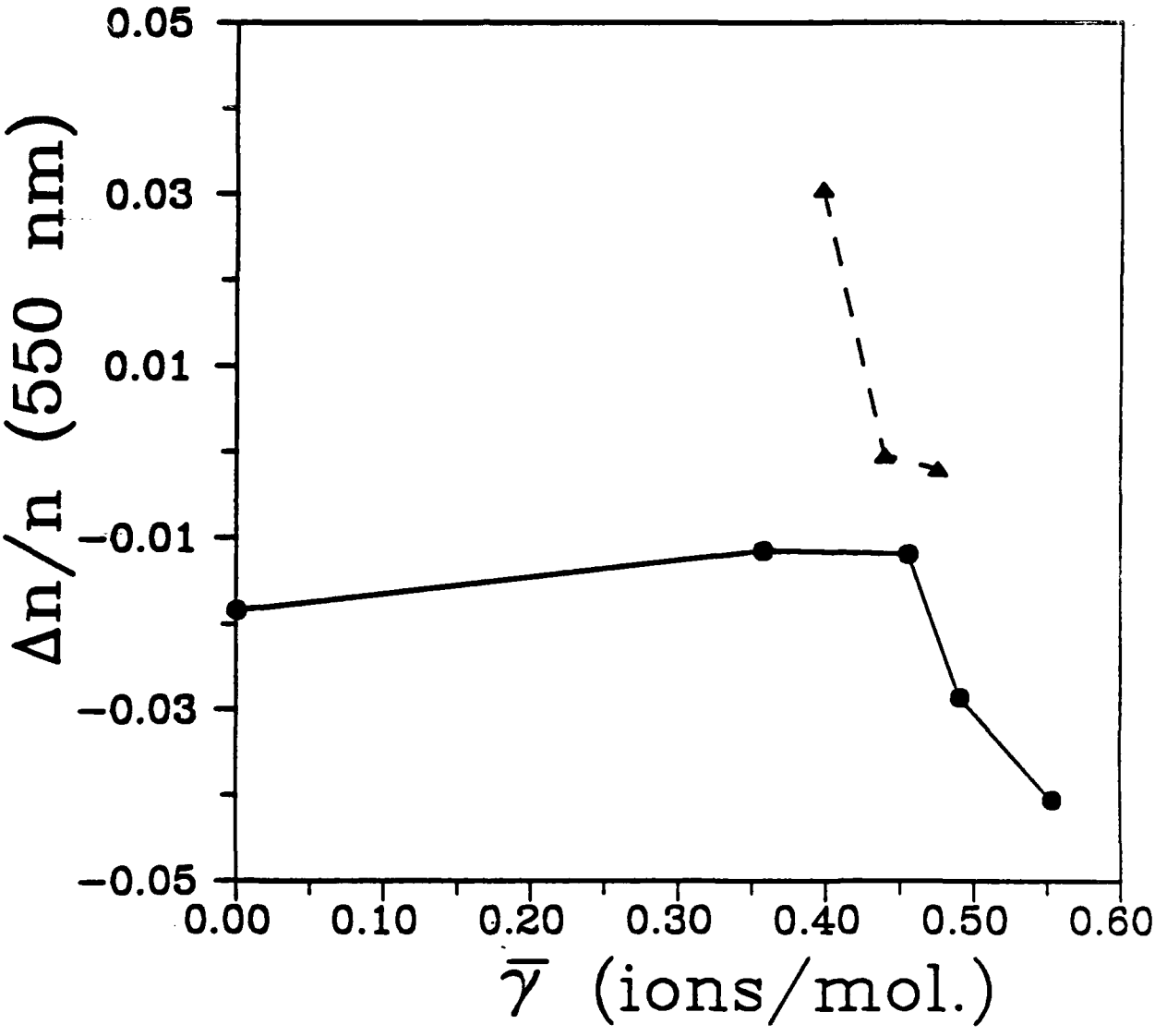
0.05
0.03
0.01
−0.01
−0.03
−0.05
Δn/n (550 nm)
0.00
0.10
0.20
0.30
0.40
0.50
0.60
$\bar{\gamma}$ (ions/mol.)

figure 4

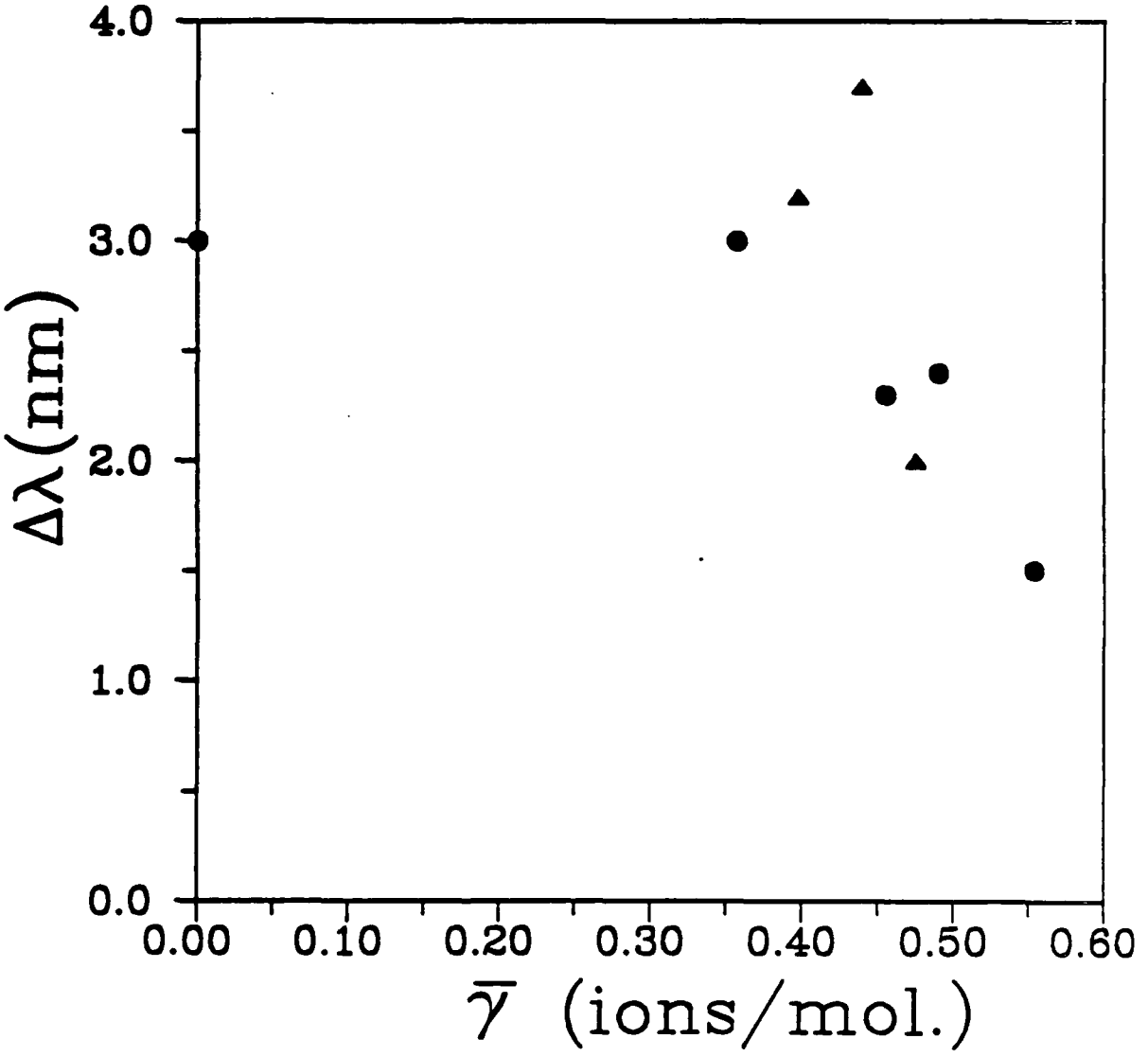
4.0
3.0
2.0
1.0
0.0
Δλ(nm)
0.00
0.10
0.20
0.30
0.40
0.50
0.60
$\overline{\gamma}$ (ions/mol.)

# APPENDIX B

# PREPARATION OF ALUMINUM NITRIDE AND OXYNITRIDE THIN FILMS BY ION-ASSISTED DEPOSITION

J. D. TARGOVE,* L. J. LINGG,* J. P. LEHAN,* C. K. HWANGBO,* H. A. MACLEOD,*
J. A. LEAVITT,** and L. C. MCINTYRE, JR**
*Optical Sciences Center, University of Arizona, Tucson, AZ 85721
**Department of Physics, University of Arizona, Tucson, AZ 85721

## ABSTRACT

Aluminum nitride thin films have been deposited by ion-assisted deposition. Aluminum was electron-beam evaporated onto substrates with simultaneous nitrogen ion bombardment. Rutherford backscattering spectrometry showed that nitrogen-to-aluminum ratios of one or greater could be achieved with sufficient nitrogen ion fluxes. This excess nitrogen apparently degrades the optical properties of the films in the visible. Annealing at 500°C improves the optical properties drastically at the expense of a slight oxygen diffusion into the films. Finally, aluminum oxynitride films were deposited by adding an oxygen backfill to the vacuum chamber during deposition. These films had very similar optical properties to the annealed nitride films.

## INTRODUCTION

Aluminum nitride (AlN) is a very attractive coating material for many applications. Its mechanical strength and chemical stability have resulted in its use as a protective layer on machine tools and as an insulating layer in microelectronic applications. More recently, its relatively wide bandgap (6.5 eV) has led to its consideration as an optical coating material for use in the visible and near-ultraviolet regions [1,2].

Aluminum nitride films have been deposited by many methods, including chemical-vapor deposition [3], reactive ion sputtering [4], ion implantation [5], and dual-beam ion sputtering [6,7]. In this work, we have bomarded a growing aluminum film with a nitrogen ion beam, with the aluminum thermally evaporated from an electron-beam source. It was hoped that the use of a thermal source could provide a large aluminum deposition rate and allow the deposition of AlN over a wide area in a system where only one ion source was available. Martin and Netterfield have recently reported the successful ion-assisted deposition (IAD) of $Si_3N_4$ [8], suggesting that aluminum nitride deposition should also be feasible by IAD. We have also deposited aluminum oxynitride films by adding oxygen to the chamber backfill during the depositions.

## DEPOSITION CONDITIONS

The films were deposited in a Balzers BAK 760 box coater using the geometry shown in Figure 1. The substrates, glass, fused silica, and graphite, were selected for their compatibility with various forms of analysis and were held stationary during the deposition. All coating runs were performed at 100°C with a residual pressure of approximately $6\times10^{-7}$ torr. Aluminum starting material of 99.999% purity was evaporated by an electron beam source from an intermetallic crucible at an aluminum deposition rate of 0.2 to 0.7 nm/s. The aluminum deposition rate was measured by a quartz crystal rate monitor shielded from the ion beam. In most of the depositions, the chamber was filled with $6\times10^{-5}$ torr of $N_2$ gas through the ion gun. Gas could also be bled into the chamber through a leak valve in the side of the chamber, bypassing the plasma discharge in the ion gun. The substrates were ion precleaned before deposition and bombarded during deposition by nitrogen ions from a 3-cm-aperture Kaufman ion source equipped with tungsten filaments and graphite grids. The filament neutralizer emitted thermal electrons to neutralize the beam, preventing charge buildup on the dielectric substrates. A Faraday cup measured the ion current density. Aluminum nitride films were deposited by bombarding the growing aluminum films with a nitrogen ion beam with ion energies of 250, 500, 750, or 1000 eV.

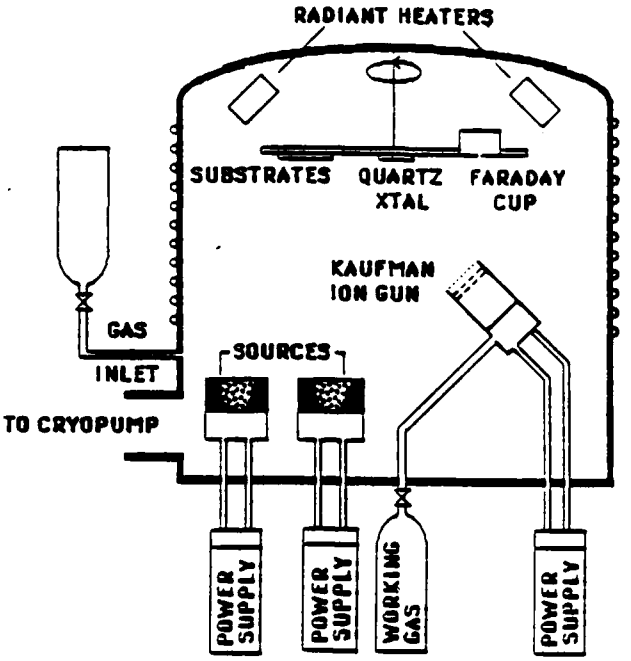


*Figure 1. Schematic of Balzers BAK 760 coating plant configured for ion-assisted deposition.*

## RUTHERFORD BACKSCATTERING SPECTROMETRY

Film stoichiometries can be measured very accurately (to better than one percent) using Rutherford backscattering spectrometry (RBS) [9]. Graphite substrates were used in this work because the silicon and oxygen RBS signals from glass substrates overlap those from aluminum, nitrogen, and oxygen in the films, decreasing measurement accuracy and complicating the analysis. In addition, aluminum nitride films must be less than 100 nm thick to prevent the oxygen and nitrogen backscattering peaks from overlapping for 1.892 MeV $He^+$ ions.

We first deposited an aluminum film at a rate of 0.2 nm/s in a nitrogen backfill of $6 \times 10^{-5}$ torr to determine if (a) this nitrogen would be adsorbed into the films and (b) whether our base vacuum was sufficiently free of oxygen and water vapor to prevent significant oxidation of the films. The nitrogen content of these films was less than 2 at. %. The bulk of the film contained 1.1 ± 0.2 at. % oxygen, with greater oxidation observed near both the substrate-film and film-air interfaces.

Table 1 shows the stoichiometries of aluminum nitride films as determined by RBS. The stoichiometries are expressed in the form $AlN_xO_y$. This is simply a convenient notation, and does not imply the formation of a compound with the indicated stoichiometry. The ratio $\gamma$ of incident nitrogen atoms to aluminum atoms at the substrate has been calculated under the assumption that the ion beam consists of $N_2^+$ ions.

Most of the films have a stoichiometry between $AlN_{0.8}$ and $AlN_{1.2}$, with a large number of the films having superstoichiometric nitrogen concentrations (Figure 2). Harper, Cuomo, and Hentzell have previously reported [6] that dual-beam sputtered films with a similar energy for the ion beam bombarding the substrate are stoichiometric if the nitrogen-to-aluminum arrival rate at the substrate is greater than one. They hypothesize that this self-limiting effect in the stoichiometry is due to diffusion of nitrogen to the surface of the films followed by desorption of $N_2$ from the surface. We observed no such self-limiting effect with ion-assisted deposition. A 1:1 ratio is achieved only for particular sets of deposition conditions rather than for whole regions of the deposition parameter space as observed with dual-beam sputtering. Since the only significant difference between the two methods is the aluminum source, it is possible that highly energetic sputtered aluminum atoms are responsible for the diffusion of excess nitrogen atoms to the surface of the films where they could be desorbed. Bombardment by the

Table 1. Stoichiometries of AlN films ($AlN_xO_y$).

| Al dep. rate (nm/sec) | Ion Beam Energy (eV) | Ion Beam Current Density ($\mu A/cm^2$) | Gamma (N atoms/Al atom) | Stoichiometry x | Stoichiometry y |
|---|---|---|---|---|---|
| 0.2 | 250 | 90 ± 20 | 0.9 ± 0.3 | 0.89 ± 0.01 | 0.04 ± 0.006 |
| 0.2 | 250 | 100 | 1.0 ± 0.4 | 1.01 ± 0.01 | 0.03 ± 0.01 |
| 0.2 | 250 | 140 | 1.5 ± 0.5 | 1.21 ± 0.02 | 0.04 ± 0.01 |
| 0.25 | 250 | 130 | 1.1 ± 0.4 | 0.81 ± 0.02 | 0.06 ± 0.01 |
| 0.2 | 500 | 190 | 2.0 ± 0.5 | 1.24 ± 0.02 | 0.03 ± 0.003 |
| 0.4 | 500 | 100 | 0.5 ± 0.1 | 0.58 ± 0.01 | 0.03 ± 0.01 |
| 0.4 | 500 | 150 | 0.8 ± 0.2 | 1.04 ± 0.02 | 0.03 ± 0.01 |
| 0.45 | 500 | 190 | 0.9 ± 0.2 | 1.15 ± 0.02 | 0.024 ± 0.006 |
| 0.2 | 750 | 100 | 1.0 ± 0.3 | 1.03 ± 0.02 | 0.05 ± 0.01 |
| 0.2 | 750 | 190 | 2.0 ± 0.5 | 1.23 ± 0.03 | 0.12 ± 0.03 |
| 0.2 | 750 | 210 | 2.2 ± 0.5 | 1.17 ± 0.02 | 0.09 ± 0.02 |
| 0.4 | 750 | 145 | 0.8 ± 0.2 | 0.82 ± 0.01 | 0.02 ± 0.01 |
| 0.45 | 750 | 100 | 0.4 ± 0.1 | 0.55 ± 0.01 | 0.023 ± 0.004 |
| 0.45 | 750 | 200 | 0.9 ± 0.2 | 1.27 ± 0.02 | 0.03 ± 0.003 |
| 0.6 | 750 | 380 | 1.3 ± 0.2 | 1.11 ± 0.02 | 0.08 ± 0.02 |
| 0.65 | 750 | 290 | 0.9 ± 0.2 | 1.26 ± 0.02 | 0.027 ± 0.003 |
| 0.25 | 1000 | 200 | 1.8 ± 0.5 | 1.29 ± 0.03 | 0.21 ± 0.01 |
| 0.25 | 1000 | 300 | 2.7 ± 0.6 | 1.58 ± 0.10 | 0.52 ± 0.04 |

nitrogen beam alone presumably does not provide sufficient mobility to the growing film to allow sufficient nitrogen diffusion.

The RBS results also show that the films have very high packing densities: The majority of the films show no measurable amount of oxygen below the surface, suggesting that any oxygen adsorbed from the residual chamber atmosphere during deposition is resputtered, and that the films are too dense for water to migrate through the films after venting the system to atmosphere. There is an oxidized layer at the surface of the films with a thickness of 15 ± 7.5 nm. The oxygen-to-aluminum ratios y in Table 1 are averages across the film, including this surface layer.

A final observation based on the RBS analysis is that the film deposition rate can be increased if a sufficient ion flux is available. We have shown that 300 $\mu A/cm^2$ of 750 eV ions is sufficient to produce a superstoichiometric film for an aluminum deposition rate of 0.65 nm/s.

The RBS results indicate several sets of of deposition conditions which yield a 1:1 aluminum-to-nitrogen ratio. For example, evaporating aluminum at a rate of 0.2 nm/s while bombarding with a 750-eV, 100-$\mu A/cm^2$ ion beam should result in a stoichiometric film. However, we shall show in the next section that films deposited with parameters similar to this are optically absorbing.

## OPTICAL MEASUREMENTS

Transmittance and reflectance measurements have been performed on films deposited onto fused silica substrates in a Cary 14 dual-beam spectrophotometer over a wavelength range of 0.2 to 2.0 $\mu m$. Films deposited with an insufficient ion-beam flux are opaque with a shiny or dull grey appearance depending on the deposition conditions. The sheet resistance of these films has been measured with a four-point probe, which shows that the resistance of films rises above the 3000 $\Omega$/square upper limit of our instrument when the films begin to show any transmittance in the visible. As the film approach the correct stoichiometry, the

transmittance increases. In even the best case, however, the films begin to absorb at wavelengths shorter than 500 nm (Figure 3). Holmes has observed a similar behavior with reactive ion beam sputtered films [4], which he attributed to nitrogen vacancies or defect states, although his films showed no absorption until 450 nm. Our films are in general nonabsorbing at wavelengths longer than 1 μm, and we have therefore used the quarter-wave transmittance in the 1 to 2 μm region to calculate a refractive index for these films. As the dispersion curve of AlN is essentially flat over this wavelength region, calculations performed at slightly different wavelengths are still comparable. Table 2 gives the refractive indices of these films; these values are slightly lower than the literature values of 1.90 to 1.95 [1].

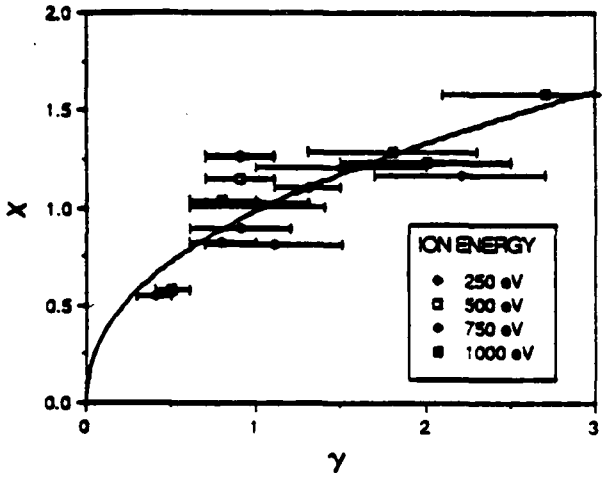


*Figure 2. Stoichiometry of aluminum nitride films, expressed in the form $AlN_x$, as a function of the ratio γ of nitrogen to aluminum arrival rates.*

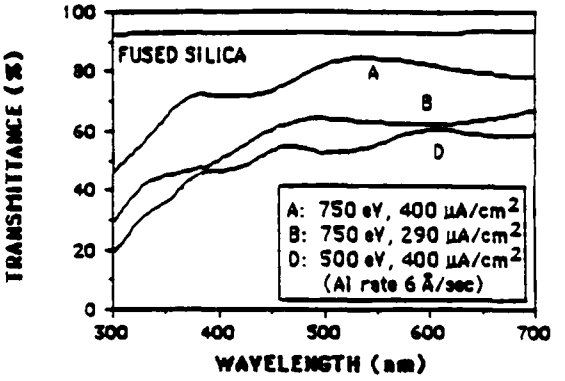


*Figure 3. Transmittance of typical AlN films deposited by ion-assisted deposition.*

**Table 2. Near infrared refractive indices of AlN films.**

| Al dep. rate (nm/s) | Ion Beam Energy (eV) | Ion Beam Current Density ($\mu A/cm^2$) | Gamma (N atoms/Al atom) | Refractive index n |
|---|---|---|---|---|
| 0.2 | 750 | 185 ± 20 | 1.9 ± 0.6 | 1.87 ± 0.02 |
| 0.3 | 500 | 150 | 1.0 ± 0.3 | 1.89 |
| 0.3 | 500 | 190 | 1.3 ± 0.3 | 1.82 |
| 0.4 | 750 | 290 | 1.5 ± 0.2 | 1.86 |
| 0.6 | 750 | 400 | 1.4 ± 0.2 | 1.84 |

## ANNEALING STUDIES

In an attempt to improve the optical properties of the films, a number of films were annealed in a tube furnace at 500°C. Dry nitrogen was flowed through the tube to reduce the oxygen and water content in the furnace, but the tube was not sealed. Table 3 shows the effect of annealing on three RBS samples with widely varying stoichiometries. We see that the nitrogen content of the films remains the same or decreases after 210 minutes, and that the oxygen content of the films increases slightly. The oxygen in the original films was concentrated in a surface layer which became thicker upon annealing as oxygen penetrated into the films.

The annealing of thicker samples on fused silica substrates showed that the optical properties of the films were improved substantially (Figure 4), with no absorption observed at wavelengths longer than 500 nm, and the absorption edge moved below 350 nm. Additional

Table 3. Effect of annealing on stoichiometry of $AlN_xO_y$ films.

| Al dep. rate (nm/s) | Ion Beam Energy (eV) | Ion Beam Current Density ($\mu A/cm^2$) | Stoichiometry Unannealed x | Unannealed y | Annealed x | Annealed y |
|---|---|---|---|---|---|---|
| 0.45 | 750 | 100 | 0.55 ± 0.01 | 0.023 ± 0.004 | 0.56 ± 0.01 | 0.068 ± 0.004 |
| 0.25 | 250 | 130 | 0.81 ± 0.02 | 0.06 ± 0.01 | 0.74 ± 0.02 | 0.15 ± 0.01 |
| 0.65 | 750 | 290 | 1.26 ± 0.02 | 0.027 ± 0.003 | 1.15 ± 0.02 | 0.054 ± 0.005 |

annealing at 500°C did not effect the transmittance of the films, although additional oxygen is certainly diffusing into the films. This suggests that unsatisfied bonds in the films are being filled quickly by oxygen atoms or complexes, eliminating the dangling-bond related absorption. The cause of the remaining absorption is still not positively identified.

## OXYNITRIDE DEPOSITION

Mixed compounds of oxides and nitrides are useful in tailoring the refractive index of coating materials. Aluminum oxynitrides should span the refractive index range between 1.65 and 1.9 in the visible. We have deposited aluminum oxynitride films by adding $3\times10^{-5}$ torr of oxygen to the vacuum chamber during the deposition. This oxygen then occupies adsorption sites created by the nitrogen ion bombardment. Figure 5 shows the transmittance of two films deposited with an aluminum deposition rate of 0.6 nm/sec and bombardment by 750 eV $N_2^+$ ions. Both films have significantly better optical properties than the aluminum nitride films discussed above. This is presumably due to adsorbed oxygen atoms filling vacancies created by the ion bombardment. The films still show an absorption edge more typical of the nitride material. The 200 $\mu A/cm^2$ sample has a refractive index of 1.93 while the 300 $\mu A/cm^2$ film has an index of 1.82 because of its greater oxygen content. The refractive index can thus be varied by changing the ion beam current density. An alternative method would be to pass oxygen through the ion gun. This oxygen would be more effectively implanted into the films, resulting in a larger oxygen content for the same ion beam current density. The refractive index of 1.93 is surprisingly high, and may suggest that the amount of adsorbed oxygen in the film is quite small.

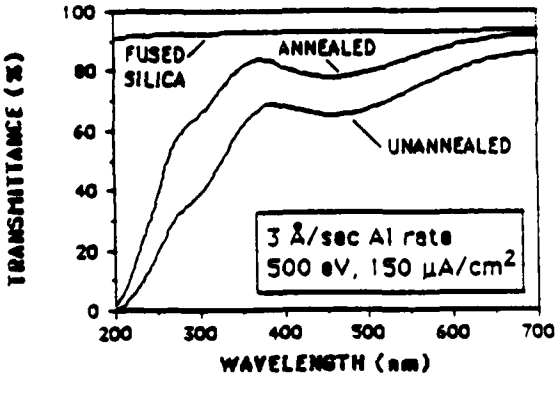


*Figure 4. Transmittance of an AlN film deposited by IAD before and after annealing for 210 minutes at 500°C.*

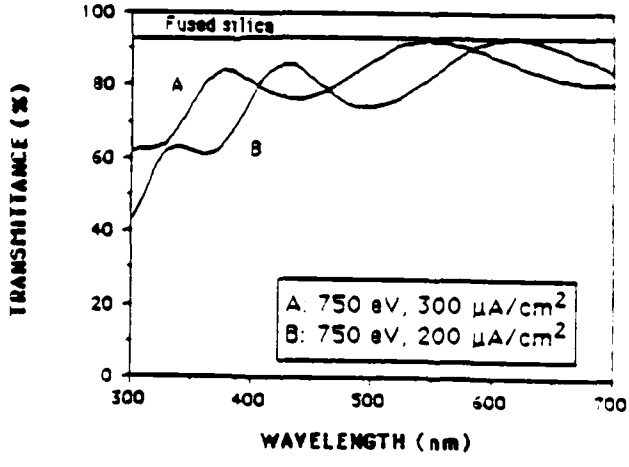


*Figure 5. Transmittance of aluminum oxynitride films deposited by IAD.*

## CONCLUSIONS

Aluminum nitride thin films can be deposited by ion-assisted deposition; however, the diffusion and desorption of excess nitrogen observed for dual-beam ion sputtering is not evident with ion-assisted deposition. An excess of nitrogen is therefore present in many of the films. A nitrogen deficiency results in opaque conducting films, while a nitrogen excess results in insulating films with absorption in the visible region of the spectrum. This absorption can be decreased by annealing in a predominantly nitrogen atmosphere at 500°C, suggesting that the absorption is due to nitrogen vacancies. Absorption is still present below 500 nm, but the films now possess a respectable transmittance in the near ultraviolet.

Adding an oxygen backfill to the chamber during deposition allows the deposition of aluminum oxynitride films. These films have significantly better optical properties than the nitride films and allow the deposition of films with a refractive index between those of $Al_2O_3$ and AlN.

This work was supported by the Air Force Office of Scientific Research through the University Research Initiative Program. The University of Arizona Ion-Beam Analysis Facility is partially supported by IBM-Tucson; the authors thank P. Stoss, M. D. Ashbaugh, B. Dezfouly-Arjomandy, M. F. Hinedi, J. Oder, J. Serveld, and G. van Zyll for assistance with RBS data acquisition and analysis.

## REFERENCES

1. W.T. Pawlewicz, P.M. Martin, R.W. Knoll, and I.B. Mann, Proc. Soc. Photo-Opt. Instrum. Eng. 678, 134 (1986).

2. L.G. Koshigoe, L.F. Johnson, T.M. Donovan, and C.D. Marrs, in *Laser Induced Damage in Optical Materials: 1984*, NBS Spec. Pub 727 (1984).

3. A.J. Noreika and D.W. Ing, J. Appl. Phys. 39, 5578 (1968).

4. Sam Holmes, Proceedings of the Society of Vacuum Coaters 29th Annual Technical Conference, 11 (1986).

5. N. Lieske and R. Hezel, J. Appl. Phys. 52, 5806 (1981).

6. J.M.E. Harper, J.J. Cuomo, and H.T.G. Hentzell, J. Appl. Phys. 58, 550 (1985).

7. Thomas H. Allen, J. Opt. Sci. Amer. A 2, P92 (1985).

8. R.P. Netterfield, P.J. Martin, and W.G. Sainty, Applied Optics 25, 3808 (1986).

9. W.K. Chu, J.W. Mayer, and M.A. Nicolet, *Backscattering Spectrometry* (Academic Press, New York 1978).

# APPENDIX C

# STOICHIOMETRY OF HIGH $T_C$ THIN FILMS BY HIGH ENERGY BACKSCATTERING

J. A. LEAVITT AND L.C. MCINTYRE, JR.
DEPARTMENT OF PHYSICS
UNIVERSITY OF ARIZONA
TUCSON, AZ 85721

# ABSTRACT

ABSOLUTE AREAL DENSITIES (ATOMS/SQ CM) AND RELATIVE AREAL DENSITIES OF HIGH $T_c$ THIN FILMS MAY BE DETERMINED BY HIGH ENERGY BACKSCATTERING, USING 3 TO 5 MEV He ANALYSIS BEAMS, TO ACCURACIES OF ABOUT 3% AND BETTER THAN 1%, RESPECTIVELY.

WE SHOW THREE EXAMPLES OF THE ANALYSIS OF YBaCuO FILMS IN THE THICKNESS RANGE 2500A TO 9000A.

FIGURE 1

ORDINARY 1.9 MEV He RBS SPECTRUM OF A THIN YBaCuO FILM (SAMPLE A) HEAVILY CONTAMINATED WITH Al AND W. NOTE THE INTERFERENCE OF THE Cu, Y, Ba AND W SIGNALS.

C060987 1892 KeV He4 on Sample: YB-A [B] 1 K COUNTS FS

Q' = 25.02 uC DTR = 1.013 Phi = 0 Theta = 170 Omega = ( .78 +/- 0.02) msr

e = ( )KeV/Ch. E' = ( )KeV CF Bi = ( )

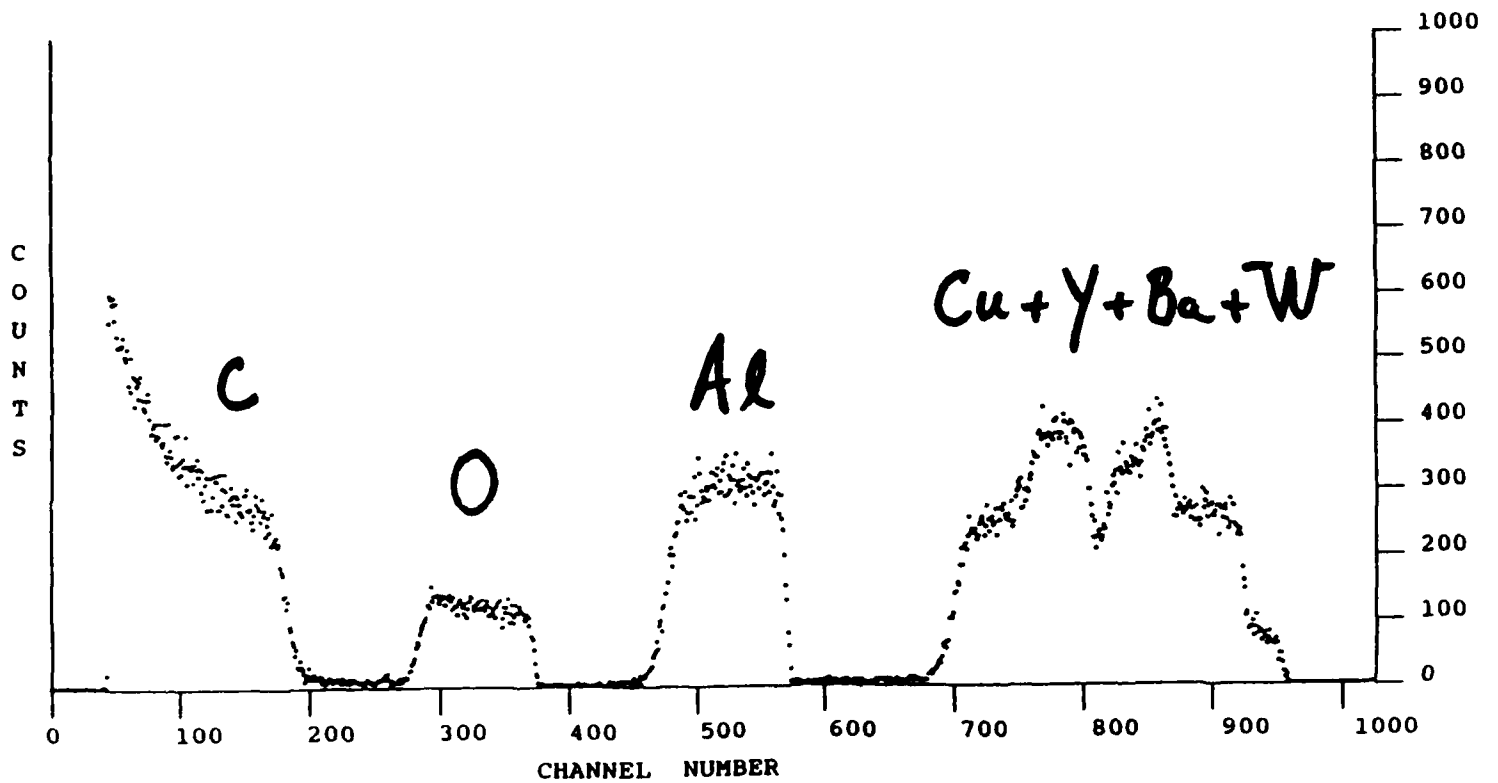

FIGURE 2

HIGH ENERGY 3.8 MEV BACK-SCATTERING SPECTRUM OF THE SAMPLE A. ONLY THE Ba AND W SIGNALS INTERFERE IN THIS SPECTRUM. THE He-O SCATTERING IS NON-RUTHERFORD.

K060987  3776 KeV He4 on Sample:  YB-A [B]  1 K COUNTS FS
Q' =  50.05 uC  DTR =  1.011  Phi = 0  Theta = 170  Omega = (  .78  +/- 0.02) msr
e = (  )KeV/Ch.  E' = (  )KeV CF Bi = (  )

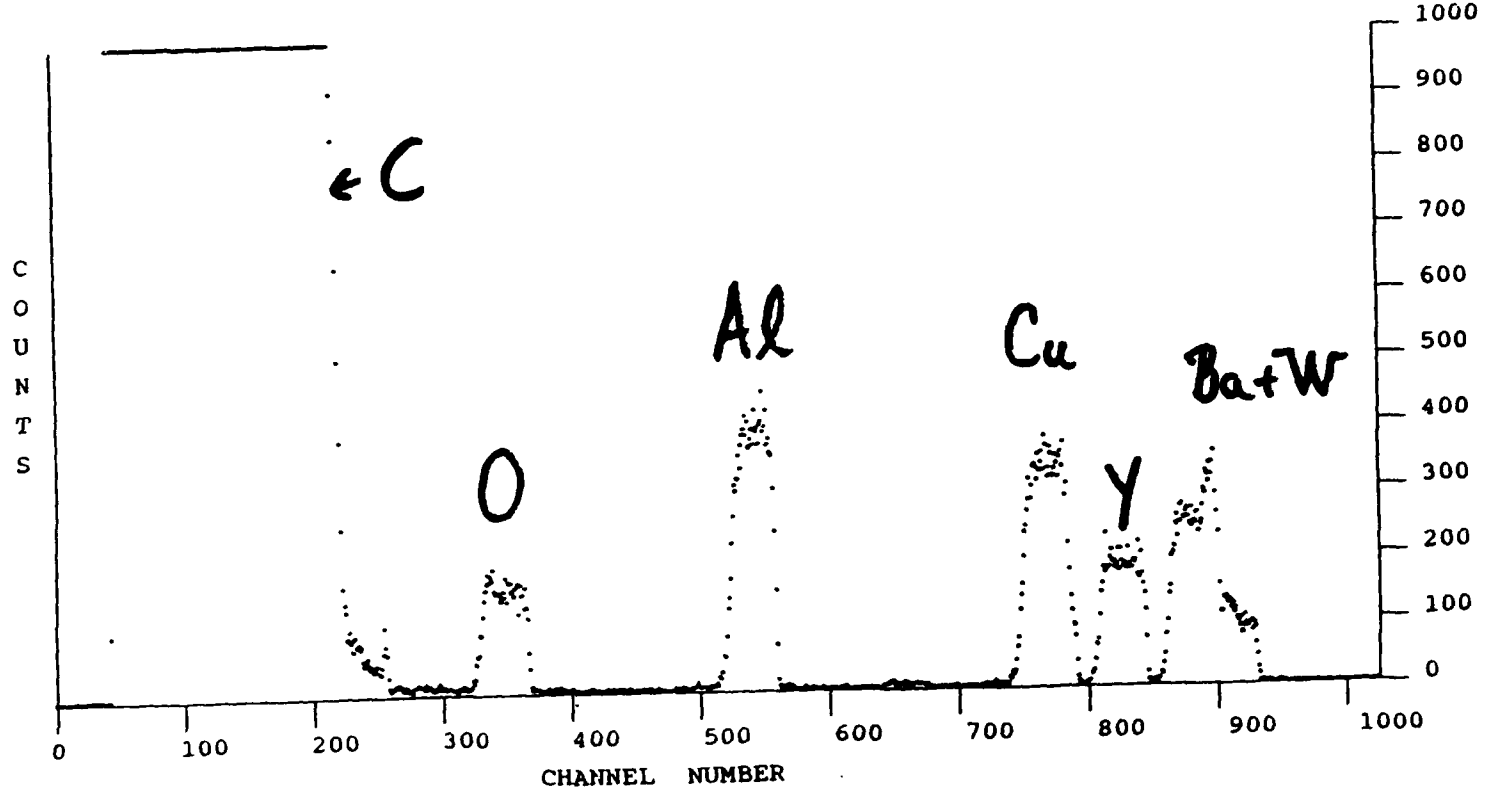

FIGURE 3

COMPUTER DECONVOLUTION OF THE INTERFERING Ba AND W SIGNALS SHOWN IN FIGURE 2.

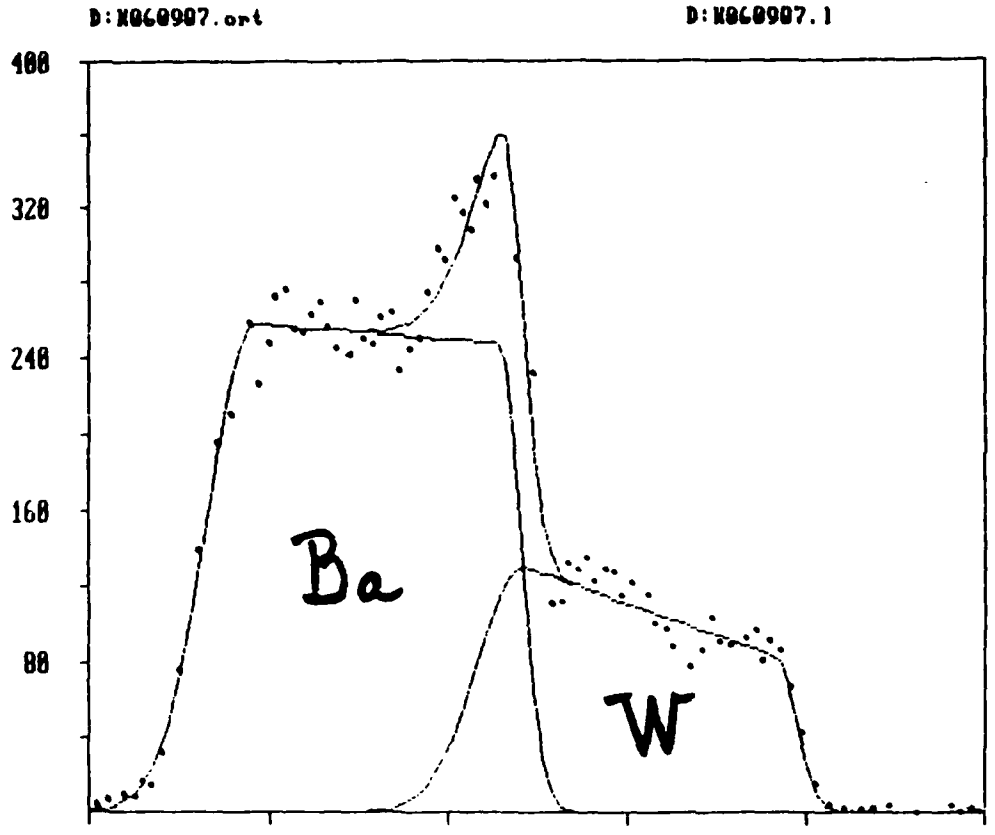


| | | | |
|---|---|---|---|
| #1 | 5.737 | 0.230 | 0.043 |
| 2 | 0.150 | 0.231 | 0.105 |
| 3 | 868.507 | 0.446 | 0.001 |
| 4 | 896.754 | 0.339 | 0.000 |
| 5 | 899.060 | 1.042 | 0.001 |
| 6 | 902.384 | 0.452 | 0.000 |
| 7 | 937.285 | 6.772 | 0.026 |
| 8 | 947.650 | 14.364 | 0.058 |
| 9 | 130.626 | 5.081 | 0.039 |
| 10 | 83.655 | 4.180 | 0.050 |

chisq= 1.27

left area= 9409.35 +/- 491.198
right area= 4163.66 +/- 184.068

total area= 13573.01 +/- 526.329

# TABLE 1

## RESULTS FOR SAMPLE A

| ELEMENT | Nt | ATOMIC % |
|---|---|---|
| Y | 0.51±0.02 | 2.4±0.1 |
| Ba | 0.33±0.02 | 1.5±0.1 |
| Cu | 1.67±0.05 | 7.7±0.1 |
| O | 10.0±0.4 | 46.0±0.6 |
| Al | 9.03±0.29 | 41.7±0.6 |
| W | 0.083±0.005 | 0.4±0.1 |
| Ar | 0.069±0.010 | 0.3±0.1 |

Nt = AREAL DENSITY (E17 ATOMS/SQ CM)

RUN = K060987 SAMPLE = YB-A NE = 7

E0 (keV) = 3776 DTR = 1.011 UCOUL = 50.05
BICF = 0.990 PHI = 0.0
UBICF = 0.030 THETA = 170.0 STER = 0.00078

LAYER = 1 ELAYER = 3776.0 MEAN E = 3741.6

| | | | | | |
|---|---|---|---|---|---|
| 1 | W (74) | A = | 4144 | UA = | 189 |
| 2 | BA (56) | A = | 9429 | UA = | 491 |
| 3 | Y (39) | A = | 7096 | UA = | 84 |
| 4 | CU (29) | A = | 12788 | UA = | 113 |
| 5 | AR (18) | A = | 200 | UA = | 27 |
| 6 | AL (13) | A = | 13390 | UA = | 118 |
| 7 | O ( 8) | A = | 5151 | UA = | 152 |

| | | | | | | | |
|---|---|---|---|---|---|---|---|
| 1 | W | NT = | 0.0827 | UNT = | 0.0045 | PUNT = | 5.48 |
| 2 | BA | NT = | 0.3287 | UNT = | 0.0198 | PUNT = | 6.02 |
| 3 | Y | NT = | 0.5112 | UNT = | 0.0166 | PUNT = | 3.25 |
| 4 | CU | NT = | 1.6725 | UNT = | 0.0528 | PUNT = | 3.16 |
| 5 | AR | NT = | 0.0687 | UNT = | 0.0095 | PUNT = | 13.84 |
| 6 | AL | NT = | 9.0342 | UNT = | 0.2851 | PUNT = | 3.16 |
| 7 | O | NT = | 9.9767 | UNT = | 0.4220 | PUNT = | 4.23 |

| | | | | | | | |
|---|---|---|---|---|---|---|---|
| 1 | W | F = | 0.004 | UF = | 0.000 | PUF = | 3.19 |
| 2 | BA | F = | 0.015 | UF = | 0.001 | PUF = | 3.55 |
| 3 | Y | F = | 0.024 | UF = | 0.000 | PUF = | 1.60 |
| 4 | CU | F = | 0.077 | UF = | 0.001 | PUF = | 1.51 |
| 5 | AR | F = | 0.003 | UF = | 0.000 | PUF = | 8.57 |
| 6 | AL | F = | 0.417 | UF = | 0.006 | PUF = | 1.42 |
| 7 | O | F = | 0.460 | UF = | 0.006 | PUF = | 1.31 |

ELOSS (keV) = 68.8 # ITERATIONS = 2 (UNITS OF NT = E17)

# APPENDIX D

# LIMITS ON THE ACCURACY OF STOICHIOMETRY DETERMINED BY RUTHERFORD BACKSCATTERING USING COMPUTER PEAK FITTING.

L. C. MCINTYRE, JR., M. D. ASHBAUGH AND J. A. LEAVITT
Department of Physics, University of Arizona, Tucson, AZ 85721

## ABSTRACT

Rutherford Backscattering Spectrometry (RBS) using MeV ions is capable of routinely measuring absolute atomic areal densities to an accuracy of about 3% and relative areal densities to a fraction of 1% if the elastic scattering peaks from different elements do not overlap. The accuracy of areal density measurements can be seriously reduced in cases where the sample thickness is large enough to cause overlapping peaks. We report here an investigation of the use of standard computer fitting techniques to analyze overlapping peaks in elastic scattering spectra and its effect on the accuracy of the final results of an RBS analysis.

## INTRODUCTION

Rutherford Backscattering Spectroscopy using MeV energy beams of He and other ions has proved to be a useful and accurate method for measuring elemental areal densities and stoichiometry of thin films and, in certain cases, of surface layers of bulk materials. The absolute accuracy of this method is limited to about 3%, due mainly to uncertainties in charge collection of the incident beam and the detector solid angle. These quantities are normally calibrated with a standard Bi in Si target [1] in which the Bi areal density is known to at least this accuracy. Stoichiometry, or relative atomic concentrations, can be determined more accurately since the factors mentioned above, which contribute the bulk of the uncertainty, cancel in these calculations.

Difficulties arise in cases where the films contain similiar mass elements and/or are of sufficient thickness to cause overlapping of the elemental (or in some cases isotopic) peaks in the backscattering energy spectrum. Several computer programs have been reported [2-6] that fit complex backscattering spectra and determine areal densities by modeling the spectrum using the parameters of the experiment, including detector resolution, and the stopping cross section of the incident ion in the film. We present here a somewhat different and simpler approach which assumes each element in a single layer film contributes a standard shape to the spectrum, and the complex spectrum is a sum of several of these standard shapes. The aim is simply to deconvolute several of these overlapping shapes and determine the individual areas. No experimental parameters or stopping-power information is used in the program. The only input information required is an initial estimate of the parameters of the standard shapes. The output is the best-fit parameters from which peak areas can be calculated. We have found this procedure to be useful and efficient in routine RBS anaylsis using a standard IBM PC microcomputer.

## FITTING FUNCTION AND PROCEDURE

A thin film consisting of a uniform distribution of a single isotope, which is either self-supporting or deposited on a substrate containing atoms less massive than those in the film, produces a backscattering energy spectrum with a shape similiar to that shown in Fig. 1.

We have written a piecewise analytic function with six parameters to represent this shape. It is a trapezoid with a half Gaussian on each end. The parameters are shown in Fig. 1 and represent the position and height of each side of the trapezoid and the width of each Gaussian. The procedure used to deconvolute several of these overlapping shapes caused by multiple elements in an actual spectrum is to use a nonlinear least-squares search routine to find the shape parameters (six per element) which best reproduce the data.

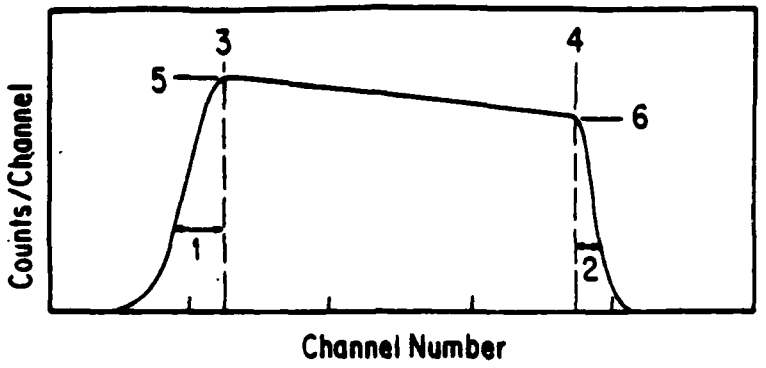


Fig. 1. Piecewise analyic shape representing the backscattering spectrum from a single element. The numbers 1-6 indicate the parameters of the shape.

We have used the subroutine CURFIT in Ref. [7] to determine these parameters. The program was written in IBM Professional FORTRAN and is run on a standard IBM PC microcomputer (with an 8087 math coprocessor). Some early results using this procedure have been reported previously [8].

This method was first tested on a fully resolved, single-element peak to assure that our analytic function would adequately represent the data. When this proved satisfactory, we proceeded to examine two- and three-element cases with various degrees of overlap. Some of these cases, together with comparisons to data taken at higher energy where the elemental peaks are resolved, will be discussed in the next section. We have applied this method to a number of special cases in which we invoke particular relationships between the parameters with some degree of success. If any of the constituents has a nonuniform depth distribution, this method is not appropriate. We have not corrected for the existence of several isotopes for a given element; however, this refinement could be added.

## TEST CASES

### Tantalum Molybdenum Superlattice Film

An example of the fitting procedure described above is shown in Fig. 2, which shows the backscattering spectrum of 1892 keV He ions scattered from a TaMo superlattice film approximately 300 nm thick on a carbon substrate.

At this incident energy, the peaks from the two elements are not resolved. The solid curve in Fig. 2 is the result of a 10-parameter fit to the data using two of our standard shapes. We used 10 instead of 12 parameters by setting the two left Gaussian widths and the two right Gaussian widths equal. The final parameters were obtained with five iterations of the CURFIT procedure, which took about 30 sec per iteration.

Separate peak areas and their uncertainties (based on the uncertainties in the parameters given by CURFIT) were calculated from the final parameters, and the stoichiometry and areal density of each element was calculated. This same film was then analyzed using 4700 keV He ions, which resulted in a backscattering spectrum in which the two peaks are completely resolved. Areal densities and stoichiometry were calculated from the resolved peaks; the two sets of results are shown in Table I.

We see that the areal densities measured in the two cases are statistically consistent and have the same uncertainty. This implies that the 3% uncertainty in charge collection and solid angle dominates any additional uncertainties produced by the computer deconvolution in the low-energy case. The uncertainty in atomic fractions, however, is a factor of five worse in the computer fitted case.

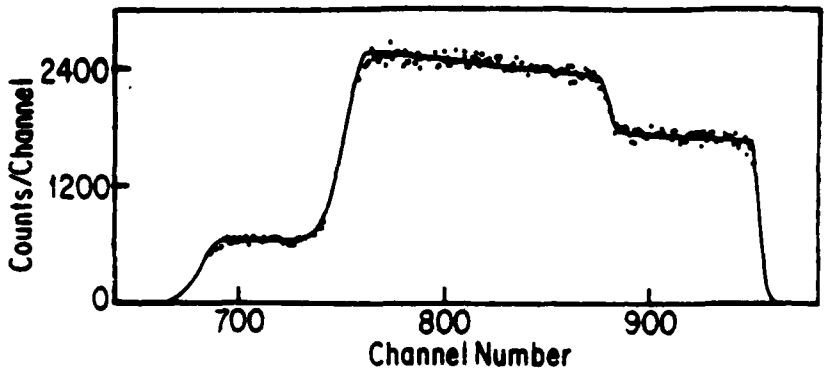


Fig. 2. Backscattering spectrum of 1892 keV He ions on a TaMo superlattice approximately 300 nm thick. The solid curve is a 10-parameter fit to the data.

Table I. Areal density and atomic fractions of TaMo film (Nt is atoms/cm$^2$ in units of $10^{17}$).

| | 1892 keV Computer Fit | | 4700 keV Resolved Peaks | |
|---|---|---|---|---|
| | Nt | F | Nt | F |
| Mo | 9.2 ± 0.3 | 0.497 ± 0.005 | 9.3 ± 0.3 | 0.501 ± 0.001 |
| Ta | 9.3 ± 0.3 | 0.503 ± 0.005 | 9.2 ± 0.3 | 0.499 ± 0.001 |

Aluminimum Oxide-(Argon) Film

An example with three overlapping peaks is shown in Fig. 3. This is a spectrum obtained by backscattering 1892 keV He ions from an aluminimum oxide film with nominal thickness about 600 nm containing argon. The solid curve is a 14-parameter fit to the data using three of our standard shapes. As in the two-peak case, the three left as well as the three right Gaussian widths were constrained to be equal.

This film was also analyzed using 3776 keV He ions, which produced a spectrum in which the three peaks were completely resolved. Table II shows a comparison of the results obtained in the two cases.

We see again that the two results are consistent, the areal densities have similiar uncertainties, and the uncertainties in the atomic fractions are considerably better in the separated peak case. It should be noted that a correction [9] was applied to the oxygen peak in the 3776 keV case to account for non-Rutherford scattering.

## SUMMARY AND CONCLUSION

We have described a simple and rapid application of standard methods for deconvoluting overlapping peaks in an elastic-scattering spectrum using a microcomputer. Its use is limited to films with uniformly distributed elemental constituants within a given layer. We have found this procedure to be convenient and useful in routine RBS analysis, and it requires no experimental parameters or ion-stopping cross sections. The resulting individual peak areas are subsequently included in the total analysis of the film together

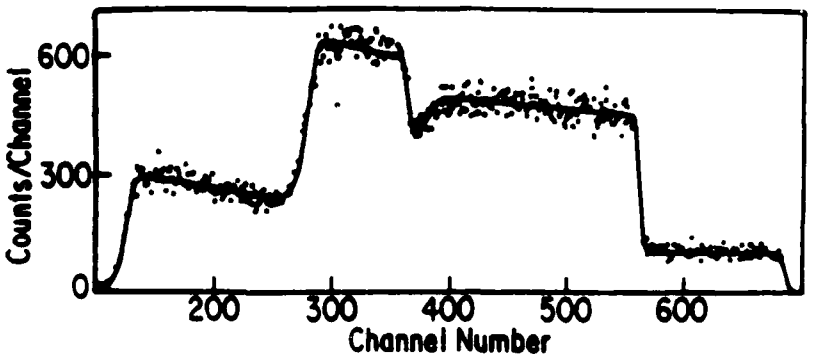


Fig. 3. Backscattering spectrum of 1892 keV He ions on a $Al_2O_3$ film approximately 600 nm thick containing Ar. The solid curve is a 14-parameter fit to the data.

Table II. Areal density and atomic fractions of $Al_2O_3$-Ar film (Nt is atoms/cm$^2$ in units of $10^{16}$).

| | 1892 keV Computer Fit | | 3776 keV Resolved Peaks | |
|---|---|---|---|---|
| | Nt | F | Nt | F |
| Al | 2.65 ± 0.09 | 0.368 ± 0.005 | 2.63 ± 0.08 | 0.367 ± 0.003 |
| O | 4.16 ± 0.16 | 0.577 ± 0.006 | 4.12 ± 0.13 | 0.575 ± 0.003 |
| Ar | 0.40 ± 0.02 | 0.055 ± 0.001 | 0.41 ± 0.01 | 0.058 ± 0.001 |

with any resolved peak areas. The examples given here involve thick targets with resulting wide peak shapes; however, in the majority of cases we have encountered involving thinner films, a typical iteration time is 5-15 sec, and the average number of iterations required is about five. We see that areal densities with comparable accuracy can be obtained from spectra containing resolved or overlapping peaks, but the accuracy of the resulting stoichiometry is still considerably greater in the resolved peak cases.

We would like to thank C. Falco, J. Makous, and L. Gignal for providing us with the films used in the examples presented here. We also thank P. Stoss, B. Dezfouly-Arjomandy, M. F. Hinedi, J. Oder, J. Seerveld, and G. van Zyll for help in taking the data. This work was partially supported by IBM-Tucson, The Optical Data Storage Center, and the Air Force Office of Scientific Research through the University Research Initiative Program.

## REFERENCES

1. Obtained from Central Bureau for Nuclear Measurements, Steenweg op Retie, 2440 Geel, Belgium.
2. P. Borgesen, R. Behrisch, and B. M. U. Scherzer, *Appl. Phys.* A27, 183 (1982).
3. P. A. Sanders and J.F. Ziegler, *Nucl. Instrum. Methods* 218, 67 (1983).
4. E. Rauhala, *J. Appl. Phys.* 56, 3324 (1984).
5. L. P. Doolittle, *Nucl. Instrum. Methods* B15, 227 (1986).
6. W. Li and A. Al-Tamimi, *Nucl. Instrum. Methods* B15, 241 (1986).
7. P. R. Bevington, *Data Reduction and Error Analysis for the Physical Sciences* (McGraw-Hill, New York, 1969).
8. J. A. Leavitt, *Nucl. Instrum. Methods* (to be published).
9. J. A Leavitt, P. Stoss, D. B. Cooper, J. L. Seerveld, L. C. McIntyre, Jr., R. E. Davis, S. Gutierrez, and T. M. Reith, *Nucl. Instrum. Methods* B15, 296, (1986).

# APPENDIX E

# ELASTIC PROPERTIES OF EPITAXIAL ZnSe (001) FILMS ON GaAs MEASURED BY BRILLOUIN SPECTROSCOPY

S. Lee, B. Hillebrands, and G. I. Stegeman

Optical Sciences Center, University of Arizona, Tucson, AZ 85721

H. Cheng and J. E. Potts

3M Company; 3M Center; St. Paul, MN 55144

F. Nizzoli[†]

Dipartimento di Matematica e Fisica, Università di Camerino

I-62032 Camerino, Italy

Brillouin scattering experiments have been performed on a series of epitaxially grown ZnSe(001) films on GaAs (001) of thicknesses between 0.23 $\mu$m and 2.0 $\mu$m. No thickness-dependent modifications of the elastic constants have been found. The obtained room temperature values of $C_{11}$ = 87.0, $C_{12}$ = 54.7 and $C_{44}$ = 39.1 GPa are in good agreement with literature values of ZnSe bulk material. The calculation of the theoretical cross sections shows a good agreement with the experimental data.

PACS numbers: 78.35.+c, 62.20.Dc

[†] Also at Gruppo Nazionale Struttura della Materia, Università di Modena, Italy

Epitaxial films of ZnSe have drawn considerable interest for their physical properties, as well as their applications in optical and ultrasonic devices. Since the ZnSe lattice parameter exceeds that of GaAs at room temperature by 0.27%, epitaxially grown ZnSe(001) films on GaAs(001) are compressively strained in the plane of the interface, and because of the resulting tetragonal distortion of the lattice (Poisson effect), they are tensionally strained normal to this plane. Mitsuhashi *et al.*[1] have measured by X-ray diffraction the dependence of the perpendicular lattice parameter of ZnSe on the layer thickness for films grown on GaAs (001) by metal-organic chemical vapor deposition (MOCVD) at 400 °C. They find that layers thinner than 0.15 $\mu$m grow coherently on GaAs (the mismatch strain is accommodated elastically); between 0.15 and 1.0 $\mu$m the perpendicular lattice parameter (and the elastic strain) diminishes as misfit dislocations form to relieve the strain. Beyond 1.0 $\mu$m, the lattice parameter of ZnSe matches that of the bulk material, so that the strain is fully relieved.

Due to the presence of the residual elastic strain in the films for $h \leq 1$ $\mu$m, the elastic constants of the material might be altered. To date no measurements of elastic constants of epitaxial ZnSe films have been reported.

In this paper we will present Brillouin scattering spectra for ZnSe(001) films grown by molecular-beam epitaxy (MBE) on GaAs(001) substrates. The thickness range of the films reflects the progressive strain relief demonstrated in Ref. 1. The data reveal no modification of the elastic constants with increasing strain; however the elastic constants of the films are in good agreement with those of bulk ZnSe.

Brillouin scattering has been used successfully to measure the elastic properties of thin films for a number of years.[2] In thin films, light is inelastically scattered from thermally excited acoustic phonons guided by the film. Surface and guided acoustic waves, i.e., the Rayleigh, and Lamb or so-called Sezawa modes, are localized modes travelling parallel to the film on a substrate. Their displacement fields show oscillating amplitudes within the film and an exponential decrease of the amplitudes into the

substrate, essentially confining the mode energy to the film. For large film thicknesses, the Rayleigh mode is confined to the surface of the film. With increasing film thickness, its sound velocity approaches rapidly the Rayleigh sound velocity of semi-infinite ZnSe. The modes can be described by partial waves in each material, by solving the wave equations, and by taking the mechanical boundary condition at the film surface and at the interface between the film and the substrate into account.[3] Although the stress fields do not directly enter the equation, they can modify the elastic constants via higher order terms. In addition to the Rayleigh mode, Lamb or so-called Sezawa modes exist if $v_T^L < v_T^S$, where $v_T^L$ and $v_T^S$ are the bulk transverse sound velocities of the layer and the substrate, respectively. The corresponding sound velocities $v_i$ are limited to the regime $v_T^L < v_i < v_T^S$.

The series of ZnSe films used in this work were grown on semi-insulating GaAs(001) substrates in a Perkin-Elmer Model 430 MBE system, as described elsewhere.[4,5] The thicknesses of the films investigated here are 0.23, 0.53, 1.0 and 2.0 $\mu$m, as measured by a Dektak surface profiler.

The Brillouin scattering experiments were performed by measuring surface phonons propagating both in [100] and [110] directions at room temperature in a backscattering geometry using a (3+3)-pass tandem Fabry-Perot interferometer. A single-mode 514.5 nm $Ar^+$ ion laser was used with an incident power of up to 300 mW, depending on the sample thickness and incident angles. For sample thicknesses less than 1.0 $\mu$m or an incident angle less than $50^0$, the power was reduced in order to avoid surface damage. The incident light was p-polarized. The polarization of the scattered light was not analyzed in order to achieve a sufficiently high scattering signal. The aperture of the collecting lens (f = 50 mm) was 1:2.8. Larger aperture did not allow adequate resolution of the localized modes in the spectra.

Figure 1 shows Brillouin spectra (full lines) for a 2.0 $\mu$m sample (Fig. 1a) and a 0.23 $\mu$m sample (Fig. 1b) exhibiting surface phonons propagating in [100] direction.

The angle of incident light was 60°. The scattering intensities show the Stokes/anti-Stokes symmetry, which is characteristic for phonon excitations in the GHz regime at room temperature. The most intense inelastic peak in both spectra at 7.0 GHz is due to the Rayleigh surface mode of the ZnSe film. The next intense peak at 13.6 GHz in Fig. 1a, which is strongly reduced in intensity for the 0.23 $\mu$m sample (Fig. 1b), is identified as a longitudinal guided acoustic phonon described elsewhere.[6] The two peaks between 8 and 10 GHz in Fig. 1b are the localized film modes (Lamb modes).

Dividing the measured mode frequencies by the component $q_{||}$ of the phonon wave vector parallel to the surface, which is determined by the scattering geometry, one obtains the phonon phase or sound velocities. They are plotted in Fig. 2 as a function of $q_{||}h$, where h is the total thickness of the film. Each symbol denotes a different thickness of the ZnSe film. A set of data points for each sample was obtained by varying $q_{||}$, i.e., by changing the angle of incidence from 40° to 70° in 10° increments. The choice of sample thicknesses h and of $q_{||}$ allows the phonon velocities to be followed over a continuous range of $q_{||}h$. The error in the sound velocities is 2% and the error in the film thickness is 5%.

In order to determine the elastic constants of the film, we used the following procedure: from the frequency shifts of the Rayleigh mode and the longitudinal guided acoustic phonon[6] of the 2.0 $\mu$m sample measured in [100] and [110] directions, we determined their corresponding sound velocities and thus their elastic moduli $c_R$ and $c_L$. Since the film thickness is much larger than the acoustic wavelength and thus the penetration depth of the Rayleigh mode, we could assume that the observed Rayleigh sound velocity is that of semi-infinite ZnSe. The sound velocity of the longitudinal guided acoustic phonon is a very good approximation of that of the corresponding longitudinal bulk phonon.[6] From this set of four experimental values we determined the elastic constants of ZnSe by a least-squares fit. The residual sum of squares was much smaller than the experimental error, confirming this procedure. The results are

listed in Table 1 for comparison with literature data.[7-12] The obtained elastic constants of ZnSe films are in excellent agreement with the literature values obtained for the bulk material, thus ruling out modifications due to the film growth within 5%.

The dispersion curves (full lines in Fig. 2) were calculated using the elastic continuum model described above with the obtained elastic constants of ZnSe. Figure 2 shows the dispersion curves and the experimental data in both [100] and [110] directions. All experimental values, especially those for the 0.23 $\mu$m sample, are in very good agreement with the dispersion curves calculated by using the data of the 2.0 $\mu$m sample. This shows that there is no change in the elastic constants of more than the experimental error between h = 0.23 $\mu$m and h = 2.0 $\mu$m.

In order to further test our results, and especially to determine why all theoretically expected modes could not be found experimentally, we also calculated the Brillouin scattering cross-section. The model used here has been described elsewhere[13] and takes both ripple and elasto-optic scattering, as well as corresponding interference terms, into account. The photo-elastic coefficients have been taken from literature.[11] The sign of the coefficients had to be chosen negative in order to produce agreement between the calculation and the experimental data. Figure 1 shows the theoretical curves as dashed lines. They are in good agreement with the experimental spectra. In particular, the relatively small theoretical cross-section for the first Lamb mode in the 0.53 $\mu$m sample reproduces the experimental results.

Although transparent films in general allow for strong elasto-optic scattering contributions, the high refractive index of ZnSe also implies a large ripple scattering term. The dominant scattering contribution for the Rayleigh mode is provided by the ripple scattering mechanism at the film surface. Lamb modes show also a significant contribution from ripple scattering at the film-substrate interface. For some modes, e.g., the first Lamb mode in the 0.53 $\mu$m sample, elasto-optically scattered light from the film is comparable in amplitude to the ripple contributions and interferes destructively with light scattered by the surface ripple, accounting for the observed small cross section.

In conclusion, we have determined the elastic constants for epitaxially grown ZnSe(001) films on GaAs(001). No modification of the elastic constants could be found as compared to the literature (bulk) values. In particular, the elastic constants show no measureable thickness dependence for 0.23 $\mu$m $\leq$ h $\leq$ 2.0 $\mu$m. Thus, the influence of the strain field in the elastic constants seems to be negligible. Since changes in the elastic constants are related to changes in the free-energy density, the latter seems to be unaffected by the strain field, which in turn is corroborated by the absence of dislocation formation for h < 0.15 $\mu$m and the slow onset for 0.15 $\mu$m < h < $\mu$m.[1] Calculations of the scattering cross section are in good agreement with the experimental data, and exhibit scattering intensities mostly dominated by ripple scattering. The lack of obeservation of some Lamb modes could be explained by destructive interferences of scattering contributions, due to ripple scattering at the film surface and elasto-optic scattering in the film.

**Acknowledgements**

This work was supported by the Air Force Office of Scientific Research University Research Initiative Program under contract No. F 49620-86-C-0123, and by the Defense Advanced Research Project Agency under Office of Naval Research contract No. N 00014-85-C-0552. F. Nizzoli acknowledges a travel grant from Consiglio Nazionale Ricerche of Italy.

**References:**


1 H. Mitsuhashi, I. Mitsuishi, M. Mizuta, and K. Kukimoto, Jpn. J. Appl. Phys. 24, L578 (1984).

2 B. Hillebrands, P. Baumgart, R. Mock, and G. Güntherodt, J. Appl. Phys. 58, 3166 (1985).

3 G.W. Farnell, *Physical Acoustics*, edited by W.P. Mason and R.N. Thurston (Academic, New York, 1972), Vol. 9, p.35.

4 J.E. Potts, H. Cheng, S. Mohapatra, and T.L. Smith, J. Appl. Phys. 61, 333 (1987).

5 H. Cheng, S.K. Mohapatra, J.E. Potts, and T.L. Smith, J. of Crystal Growth 81, 512 (1987).

6 B. Hillebrands, S. Lee, G.I. Stegeman, H. Cheng, J.E. Potts, and F. Nizzoli, to be published.

7 D. Berlincourt, H. Jaffe, and L.R. Shiozawa, Phys. Rev. 129, 1009 (1963).

8 B.H. Lee, J. Appl. Phys. 41, 2984 (1970).

9 V.I. Kuslov, A.P. Rusakov, and A.N. Mentser, Fiz. Tverd. Tela 14, 216 (1972); Sov. Phys. Solid State (Eng. Transl.) 14, 1869 (1973).

10 C.G. Hodgins, and J.C. Irwin, Phys. Status Solidi (a) 28, 647 (1975).

11 K. Wasa, M. Yamada, and C. Hamaguchi, Technol. Rep. Osaka Univ. (Japan) 28 No. 1430-1458, 447 (1978).

12 B.Kh. Bairamov, A.V. Gol'Tsev, E. Karaiamaki, R. Laikho, T. Levola, and V.V. Toporov, Fiz. Tverd. Tela (USSR) 25, 1286 (1983); Sov. Phys. Solid State (Eng. Transl.) 25, 739 (1983).

13 A. Marvin, V. Bortolani, F. Nizzoli, and G. Santoro, J. Phys. C 13, 1607 (1980).

**Table Captions:**

Table 1. Elastic constants of ZnSe in comparison to literature data. All values are given in units of GPa.

**Figure Captions:**

Figure 1. Experimental scattering intensities of (a) a 2.0 $\mu$m thick sample (b) a 0.23 $\mu$m thick sample with the wave vector in [100] direction (solid lines) and corresponding theoretical cross sections (dotted lines). The angle of incident light was 60°.

Figure 2. Dispersion curves in (a) [100] and (b) [110] directions, respectively, with experimental data. The error is 2% for the sound velocities and 5% for the film thicknesses. Circles: h = 0.23 $\mu$m, squares: h = 0.53 $\mu$m, and triangles: h = 1.0 $\mu$m.

Table 1

| Method | Piezo-resonance[7] | Ultrasonic Pulse-echo[8] | Ultrasonic interfero-meter[9] | Brillouin Scattering[10] | Thermal Brillouin Scattering[11] | Brillouin Resonance Scattering[12] | Present Work |
|---|---|---|---|---|---|---|---|
| $C_{11}$ | 81.0 ± 5.2 | 85.9 ± 0.3 | 89.5 | 87.2 ± 0.8 | 90.3 ± 1.9 | 90.0 | 87.0 ± 2.1 |
| $C_{12}$ | 48.8 ± 4.9 | 50.6 ± 0.4 | 53.9 | 52.4 ± 0.8 | 53.6 ± 2.3 | 53,4 | 54.7 ± 2.1 |
| $C_{44}$ | 44.1 ± 1.3 | 40.6 ± 0.2 | 39.84 | 39.2 ± 0.4 | 39.4 ± 1.2 | 39.6 | 39.1 ± 1.6 |
| Year | 1963 | 1970 | 1972 | 1975 | 1978 | 1983 | 1987 |
| Density | 5.26 | 5.264 | 5.264 | 5.264 | N/A | 5.264 | 5.264 |

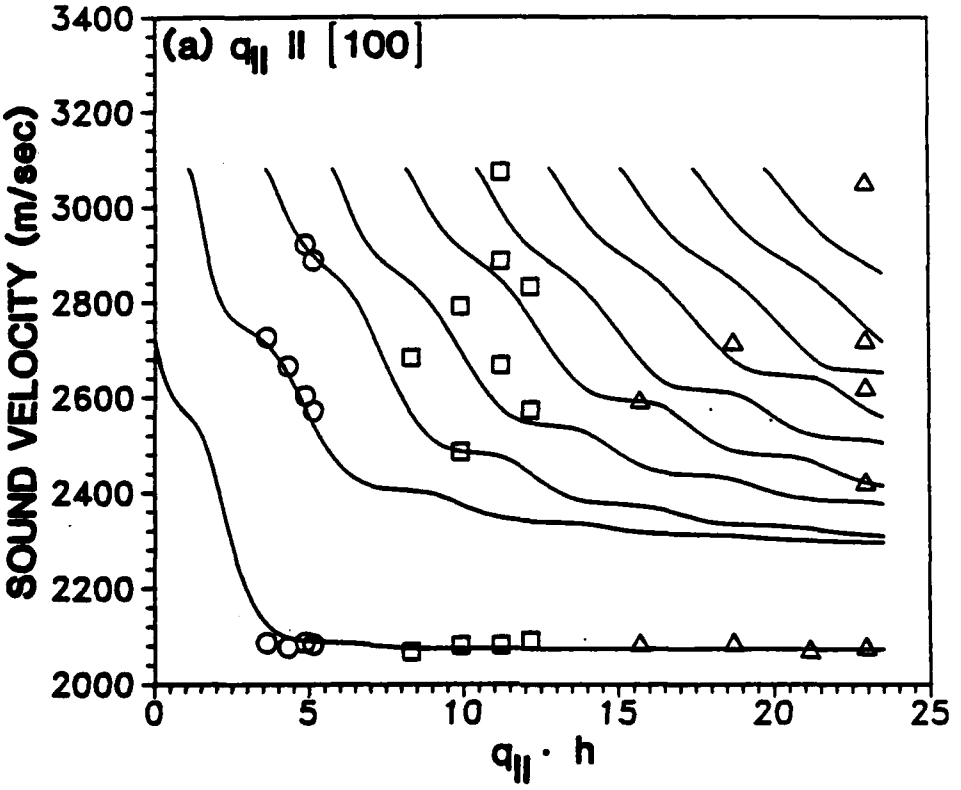
(a) $q_{||}$ || [100]
SOUND VELOCITY (m/sec)
3400
3200
3000
2800
2600
2400
2200
2000
0
5
10
15
20
25
$q_{||} \cdot h$

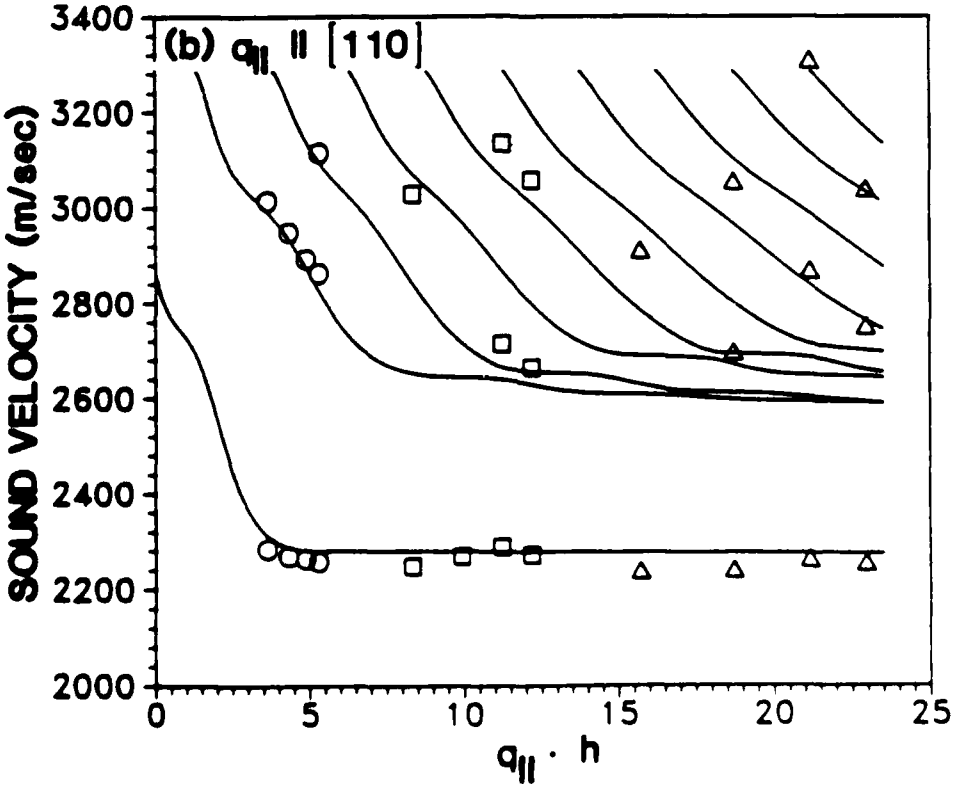
(b) $q_{||}$ || [110]
SOUND VELOCITY (m/sec)
3400
3200
3000
2800
2600
2400
2200
2000
0
5
10
15
20
25
$q_{||} \cdot h$

Figure 1

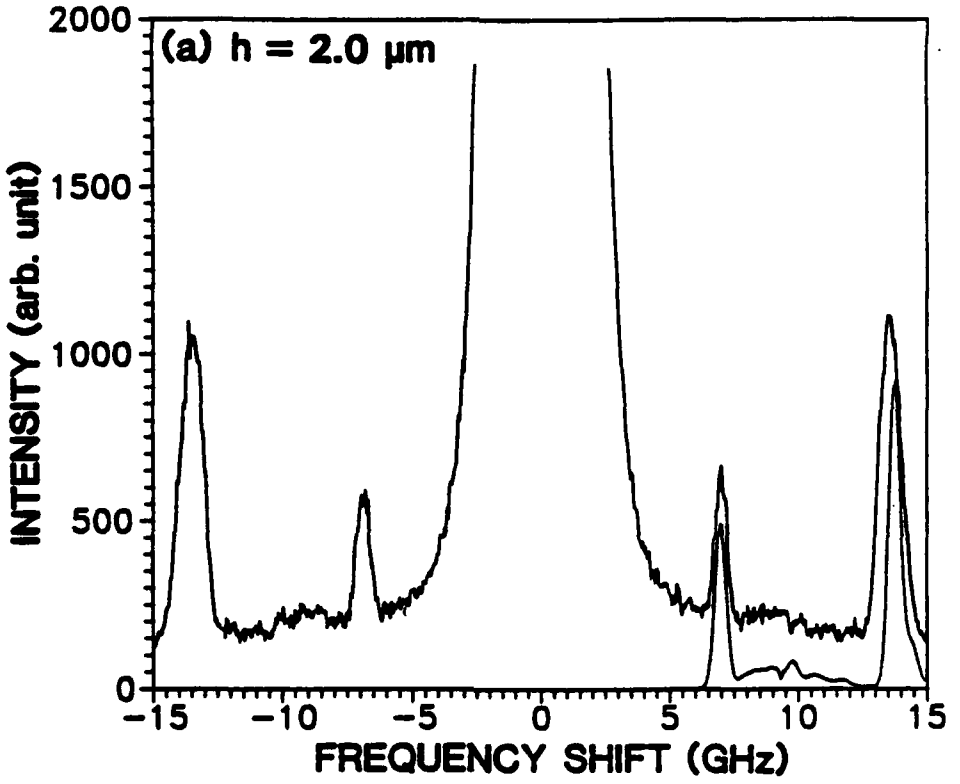
(a) h = 2.0 μm
INTENSITY (arb. unit)
2000
1500
1000
500
0
−15
−10
−5
0
5
10
15
FREQUENCY SHIFT (GHz)

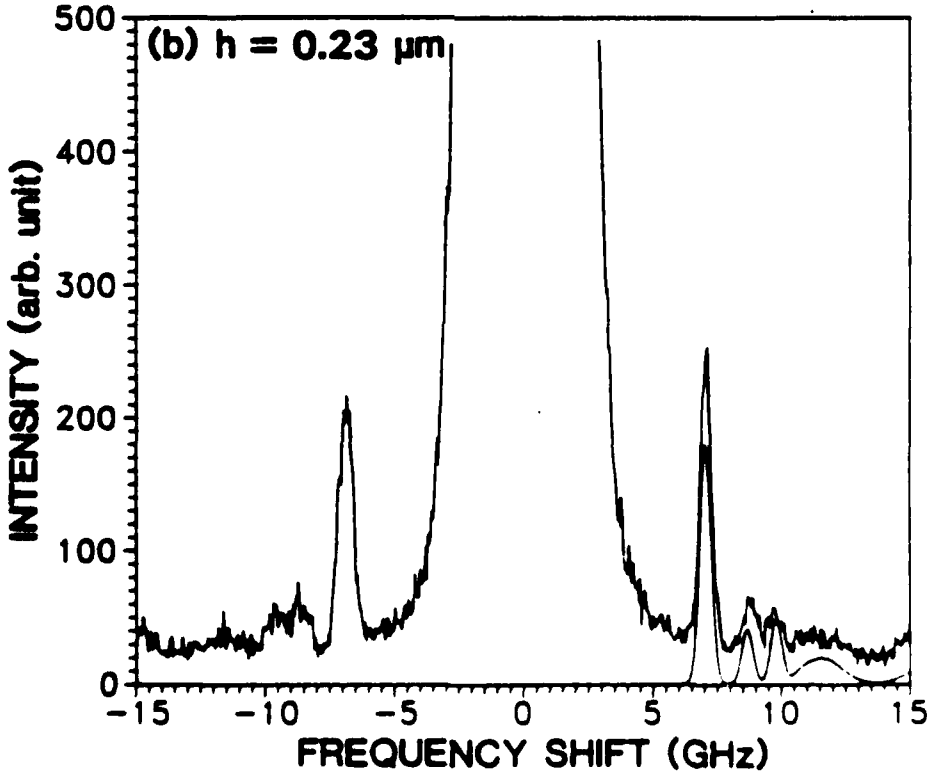
(b) h = 0.23 μm
INTENSITY (arb. unit)
500
400
300
200
100
0
−15
−10
−5
0
5
10
15
FREQUENCY SHIFT (GHz)

Figure 2

# APPENDIX F

# EVIDENCE FOR THE EXISTENCE OF GUIDED LONGITUDINAL ACOUSTIC PHONONS IN ZnSe FILMS ON GaAs

B. Hillebrands, S. Lee, G.I. Stegeman

Optical Sciences Center, University of Arizona, Tucson, AZ 85721

H. Cheng, J.E. Potts

3M Company; 3M Center; St. Paul, MN 55144

F. Nizzoli†

Dipartimento di Matematica e Fisica, Università di Camerino

I-62032 Camerino, Italy

**Abstract:**

We report theoretical as well as experimental evidence for a new class of long-wavelength acoustic film excitations which we identify as longitudinal guided acoustic phonons. Despite a coupling to propagating transverse film modes, these new modes have lifetimes comparable to the Rayleigh mode and are the longitudinal counterpart to the well-known Lamb or Sezawa modes, with analogous existence critera. The properties of the new modes are discussed in detail for ZnSe films on GaAs, the material system for which we were able to observe these modes by Brillouin spectroscopy.

† also at Gruppo Nazionale Struttura della Materia, Università di Modena, Italy

PACS - numbers: 78.35+c, 68.55.Pr

In the field of long-wavelength acoustic surface and film excitations, the Rayleigh mode, which always exists on the surface of a semi-infinite material, is the most prominent member.[1] For a film on a substrate, higher-order modes, which are called Lamb or Sezawa modes, exist in the sound velocity regime bounded by the transverse sound velocities of the film ($v_T^f$) and the substrate ($v_T^s$) for the case $v_T^f < v_T^s$.[2] All of these modes consist of shear vertical and longitudinally polarized partial waves whose field components propagate parallel to the surfaces and decay exponentially with distance into the substrate, thus confining the mode energy to the immediate vicinity of the film (or surface for a Rayleigh wave). Within the film, the shear partial waves are propagating in character and the longitudinal partial waves are always evanescent. Recently the longitudinal counterpart to the Rayleigh mode, the so-called longitudinal resonance with a sound velocity slightly below the longitudinal sound velocity and with longitudinal components decaying exponentially into the medium, was predicted theoretically and observed experimentally in gold.[3-5] However, since this mode radiates usually quite strongly into transverse substrate modes, the mode is quasi-localized, i.e., leaky, with a relatively large linewidth when probed by Brillouin spectroscopy. Consequently, it was expected that the longitudinal counterparts of the Lamb (Sezawa) modes, whose velocities are even higher than those of the longitudinal resonances, would have even larger linewidths and be more difficult to observe. In this paper we report on the successful observation of these modes by Brillouin spectroscopy in epitaxial ZnSe films on GaAs substrates. Contrary to initial expectations, we also found that the lifetime of these modes can be long and the linewidths narrow, comparable to those of the Rayleigh wave itself.

The nature of the longitudinal guided acoustic waves can be easily understood by examining the acoustic reflections at the two film boundaries. Since the principal contribution to the total displacement field consists of propagating, longitudinally-polarized, partial waves in the film, which are incident and reflected from the film

boundaries at grazing angles, mode conversion into the shear-polarized standing waves in the film is weak. For $v_L^f < v < v_L^s$ where $v_L^f$, v, and $v_L^s$ are respectively the film, guided wave, and substrate longitudinal wave velocities, the longitudinal fields decay evanescently into the substrate and no radiation into substrate longitudinal modes can occur. Furthermore, the grazing incidence angle condition also ensures very weak radiative coupling into substrate shear modes. These waves can be identified as longitudinal guided acoustic waves because their properties and existence conditions are completely analogous to those of the Lamb modes. With increasing film thickness the sound velocities decrease approaching asymptotically $v_L^f$. Varying the substrate sound velocity in a computer simulation for a ZnSe film on a (001) GaAs substrate, we also found evidence for higher-order longitudinal guided modes.

The materials system which satisfies the above requirements on acoustic properties consisted of (001) ZnSe films grown on semi-insulating (001) GaAs substrates, as described elsewhere.[6,7] Sample thicknesses were 0.23, 0.53, 1.0 and 2.0 $\mu$m. The Brillouin measurements were performed in air at room temperature using a Sandercock-type (3+3)-pass tandem Fabry-Perot interferometer in a backscattering geometry. The light source was a single mode 514.5 nm $Ar^+$ ion laser. The laser power at the sample was typically 200 mW. The light scattering geometry was chosen to investigate modes with their acoustic wave-vector component parallel to the surface, $q_{||}$, lying along the [100] and [110] directions of ZnSe. The magnitude of $q_{||}$ was varied by using angles of light incidence $\Theta$ between 40° and 70° to the surface normal. The aperture of the collecting lens was 1:2.8. The incident light was p-polarized; no polarization analysis of the scattered light was made.

Figure 1 shows typical spectra for $\Theta$ = 60° and $q_{||}$ in the [100] direction. The peak at 7 GHz is identified as scattering from the Rayleigh phonon (labeled "R" in Fig. 1). The peaks between about 8 and 12 GHz are due to the localized Lamb (Sezawa) modes (labeled "S"). A pronounced peak of magnitude comparable to the Rayleigh

wave line is observed near 14 GHz in the 2 $\mu$m and the 1 $\mu$m films. It is identified as scattering from the longitudinal guided acoustic phonon (labeled "L" in Fig. 1). With decreasing film thickness, its intensity decreases, accompanied by a linewidth broadening. For h = 2$\mu$m, the frequency position of the mode, 14 GHz, is very close to the frequency of a longitudinal acoustic phonon in ZnSe travelling parallel to the film. With decreasing film thickness, the mode frequency shows a slight increase.

We have calculated the Brillouin scattering cross section using a theory which takes into account both the mechanical and the electro-magnetic boundary conditions at the film interfaces including both ripple and elasto-optic coupling mechanisms.[8] The elastic constants of ZnSe were evaluated from (i), the frequency shifts of the peaks associated with the longitudinal guided mode which yield to a good approximation (see below) the sound velocity of a longitudinal bulk phonon travelling parallel to the film, and (ii), the Rayleigh mode in the 2 $\mu$m film, all measured in [100] and [110] directions.[9] Their values of $c_{11}$ = 87.0 ± 2.1, $c_{12}$ = 54.7 ± 2.1 and $c_{44}$ = 39.1 ± 1.6 GPa are in good agreement with values reported for bulk ZnSe.[10-15] The photo-elastic coefficients and the dielectric constants of ZnSe and GaAs have been taken from literature.[14,16,17] In Fig. 1 the calculated cross section is shown by dashed lines. Good agreement between the theoretical curves and the experimental data was achieved by convolving the theoretical curves with the experimental spectrometer function. Only the absolute value of the theoretical cross section has been adjusted. Since the calculation takes all boundary conditions into account, it is not surprising that the new guided longitudinal phonon is reproduced quite well.

Figure 2 shows for the guided longitudinal mode the calculated variation of the squared parallel and perpendicular components of the displacement field in the film (negative abecissa) and the substrate (positive abscissa) normalized with respect to the maximum value of the parallel component in the substrate. They are a measure of the displacement energy. In the film the displacements are dominantly longitudinal and

their squared values exceed those of the substrate by a factor of 70 for h = 2 $\mu$m. The two pairs of partial waves in the film, longitudinal and shear, each form standing wave patterns. The larger periodicity is due to the longitudinal partial waves, whereas the shorter oscillations are due to the transverse components. The inset of Fig. 2 indicates the propagation directions associated with the longitudinal (L) and transverse (T) film and substrate partial waves. The longitudinal partial waves travel nearly parallel to the film whereas the transverse ones have a larger wave vector component perpendicular to the film.

As an existence criterion for guided waves, it is necessary that the partial waves interfere constructively. Thus the wave-vector component perpendicular to the film, $q_\perp$, must obey the resonance condition

$$2\, q_\perp\, h + \delta_S + \delta_I = 2\, n\, \pi, \qquad (1)$$

where $\delta_S$, $\delta_I$ are the phase shifts upon reflection at the two film surfaces respectively, and the mode index n is a positive integer. A calculation of the phase shifts using a simplified model[18] (i.e. elastically isotropic medium) shows that Eq. 1 is fulfilled very accurately for the longitudinal partial waves with n = 1. Eq. 1 also predicts several additional properties of the mode. Because the elastic properties of the media bounding the film are dissimilar, there is a minimum film thickness below which Eq. 1 cannot be satisfied. With increasing film thickness the value of $q_\perp$ decreases in order to fulfill Eq. 1, thus decreasing the modal sound velocity. A decreasing value of $q_\perp$ implies a decreasing amount of mode conversion into shear waves resulting in increasing localization, as experimentally observed (see Fig. 1 ). In the limit of infinitely thick films, $q_\perp$ approaches zero, which implies that the guided longitudinal acoustic phonon becomes an ordinary longitudinal bulk phonon travelling parallel to the film. It should be stressed that, for a film of finite thickness, no longitudinal bulk phonon

travelling parallel to the film may exist because the mechanical boundary conditions at the interfaces cannot be satisfied.

Fig. 3 shows results of computer simulations of the maximum of the squared parallel displacement-field amplitude of the longitudinal guided mode, normalized as in Fig. 2, as a function of the film thickness. With increasing film thickness the sound velocity shows an over-all decrease with small superimposed oscillations. The intensity of the mode increases, accompanied by strong aperiodic oscillations which exhibit monotonically increasing maxima with intervening regions of smaller maxima, accompanied by corresponding oscillations in the linewidth. The oscillatory behavior is due to the mode conversion at each reflection of transverse into longitudinal partial waves and vice versa. The transverse waves can also fulfill a resonance condition similar to Eq. 1, however with a large n which also increases with increasing film thickness. Since the total transmission of energy across the interface is proportional to the transmission coefficient at the interface and the displacement amplitude of the transverse film partial waves, a film resonance of the transverse modes implies a maximum in the energy loss into the substrate. Since the transverse mode resonance condition is periodically fulfilled with increasing film thickness, the guided mode attenuation also oscillates, accompanied by a corresponding oscillation in the linewidth. The two different types of maxima can be related to the odd or even value of n: a calculation in the isotropic approximation[18] of the phase factors for the reflection of the transverse film modes at the surface ($\delta_s = -\pi/2$) and at the interface ($\delta_i \cong 0.2$) yields a major maximum in the displacement field for even n and a secondary maximum for odd n.

In summary, we have found a longitudinal guided acoustic mode in ZnSe(001) films on GaAs(001). Its calculated linewidth is unusually small, typically 0.5% of its mode frequency. Despite the decay channel into transverse substrate modes, the new mode is the longitudinal counterpart to the (transverse) Lamb modes in a film. Thus the

classification of long-wavelength acoustic surface and film excitations now exhibits complete symmetry with respect to shear and longitudinal waves, and includes surface modes (Rayleigh mode, longitudinal resonance) and film modes (Lamb modes, guided longitudinal modes). The new longitudinal guided wave reported here offers a number of interesting possibilities. For example, it allows a very accurate determination of the longitudinal sound velocity in films, a parameter which is otherwise difficult to evaluate. Here we actually utilized this feature to evaluate the elastic constants of the ZnSe film. Since the displacement field is nearly completely polarized parallel to the film, the mode can be used to monitor effects which modulate only dilatational waves, and vice versa. The observation and application of the novel mode in systems other than ZnSe/GaAs is presumably only restricted by the existence criteria on the acoustic velocities described above.

## Acknowledgements

This work was supported by the Air Force Office of Scientific Research/University Research Initiative Program under contract No. F 49620-86-C-0123, and by the Defense Advanced Research Project Agency under Office of Naval Research contract No. N 00014-85-C-0552. F. Nizzoli acknowledges a travel grant from Consiglio Nazionale Ricerche of Italy.

## REFERENCES


[1] Lord Rayleigh, Proc. London Math. Soc. 17, 4 (1887).

[2] K. Sezawa, K. Kanai, Bull. Earth. Res. Inst. Tokyo 13, 237 (1933).

[3] N. E. Glass, A. A. Maradudin, J. Appl. Phys. 54, 796 (1983).

[4] R.E. Camley, F. Nizzoli, J. Phys. C 18, 4795 (1985).

[5] L. Bassoli, F. Nizzoli, J.R. Sandercock, Phys Rev. B 34, 1296 (1986).

[6] J.E. Potts, H. Cheng, S. Mohapatra, T.L. Smith, J. of Appl. Phys. 61, 333 (1987).

[7] H. Cheng, S.K. Mohapatra, J.E. Potts, T.L. Smith, J. of Crystal Growth 81, 512 (1987).

[8] V. Bortolani, A.M. Marvin, F. Nizzoli, G. Santoro, J. Phys. C 16, 1757 (1983).

[9] S. Lee, B. Hillebrands, G.I. Stegeman, H. Cheng, J.E. Potts, F. Nizzoli, to be published.

[10] D. Berlincourt, H. Jaffe, L.R. Shiozawa, Phys. Rev. 129, 1009 (1963).

[11] B.H. Lee, J. Appl. Phys. 41, 2984 (1970).

[12] V.I. Kuskov, A.P. Rusakov, A.N. Mentser, Fiz. Tuerd. Tela 14, 216 (1972). Sov Phys. Solid State (engl. transl.) 14, 1869 (1973).

[13] C.G. Hodgins, J.C. Irwin, Phys. Status Solidi (a) 28, 647 (1975).

[14] K. Wasa, M. Yamada, C. Hamaguchi, Technol. Rep Osaka Univ Japan No. 1430-1458, 447 (1978).

[15] B.Kh. Bairamov, A.V. Gol'Tsev, E. Karaiamaki, R [illegible] Toporov, Fiz. Tuerd. Tela (USSR) 25(5), 1286 (1983).

[16] Landolt-Börnstein, New Series III/17b, O Madelung, M [illegible] Springer, Berlin, Heidelberg, New York (1982).

[17] Landolt-Börnstein, New Series IV/22a, O Madelung, M [illegible] Berlin, Heidelberg, New York, London, Paris, Tokyo.

[18] B.A. Auld, *Acoustic Fields and Waves in Solids*, [illegible] York (1973).

AD-A191 996 CENTER FOR THIN FILM STUDIES(U) ARIZONA UNIV TUCSON OPTICAL SCIENCES CENTER R P SHANNON ET AL. 15 NOV 87 AFOSR-TR-88-0136 F49620-86-C-0123 2/2

UNCLASSIFIED F/G 20/12 NL

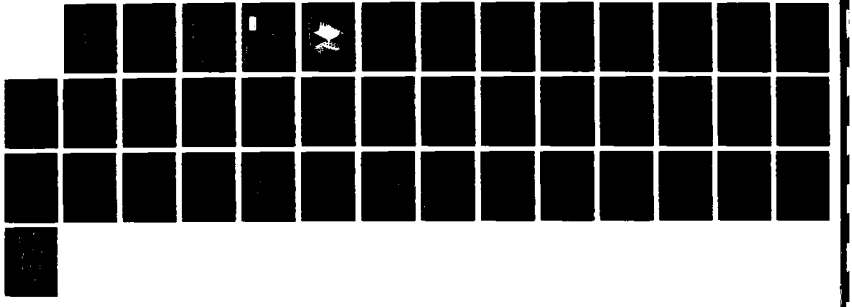

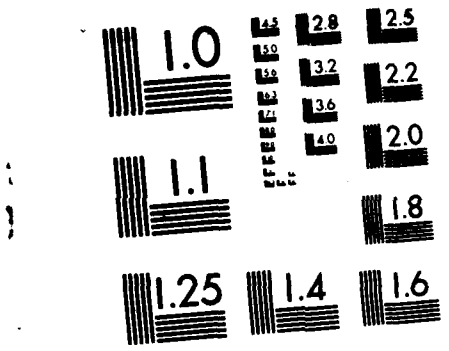


MICROCOPY RESOLUTION TEST CHART
NATIONAL BUREAU OF STANDARDS-1963-A

## FIGURE CAPTIONS

**Fig. 1:**

Brillouin spectra of ZnSe(001) films on GaAs(001) substrate. The angle of incidence is 60°, the film thicknesses are as indicated. R: Rayleigh mode, S: Lamb (Sezawa) modes, L: longitudinal guided mode.

**Fig. 2:**

Modal displacement field profile for a 2 μm ZnSe(001) film on GaAs(001), normalized with respect to the maximum value of the parallel component in the substrate. The negative values of the abscissa refer to the film, whereas the positive values refer to the substrate. The ordinate is the squared amplitude component parallel to the film (full lines) and perpendicular to the film (broken lines) of the displacement field. *Inset:* Sketch of the partial waves which constitute the longitudinal guided mode. T: transverse, L: longitudinal partial waves. Not shown is the exponentially decaying substrate longitudinal partial wave.

**Fig. 3:**

Surface plot and contour plot of the squared parallel displacement field as a function of the film thickness h and the sound velocity v.

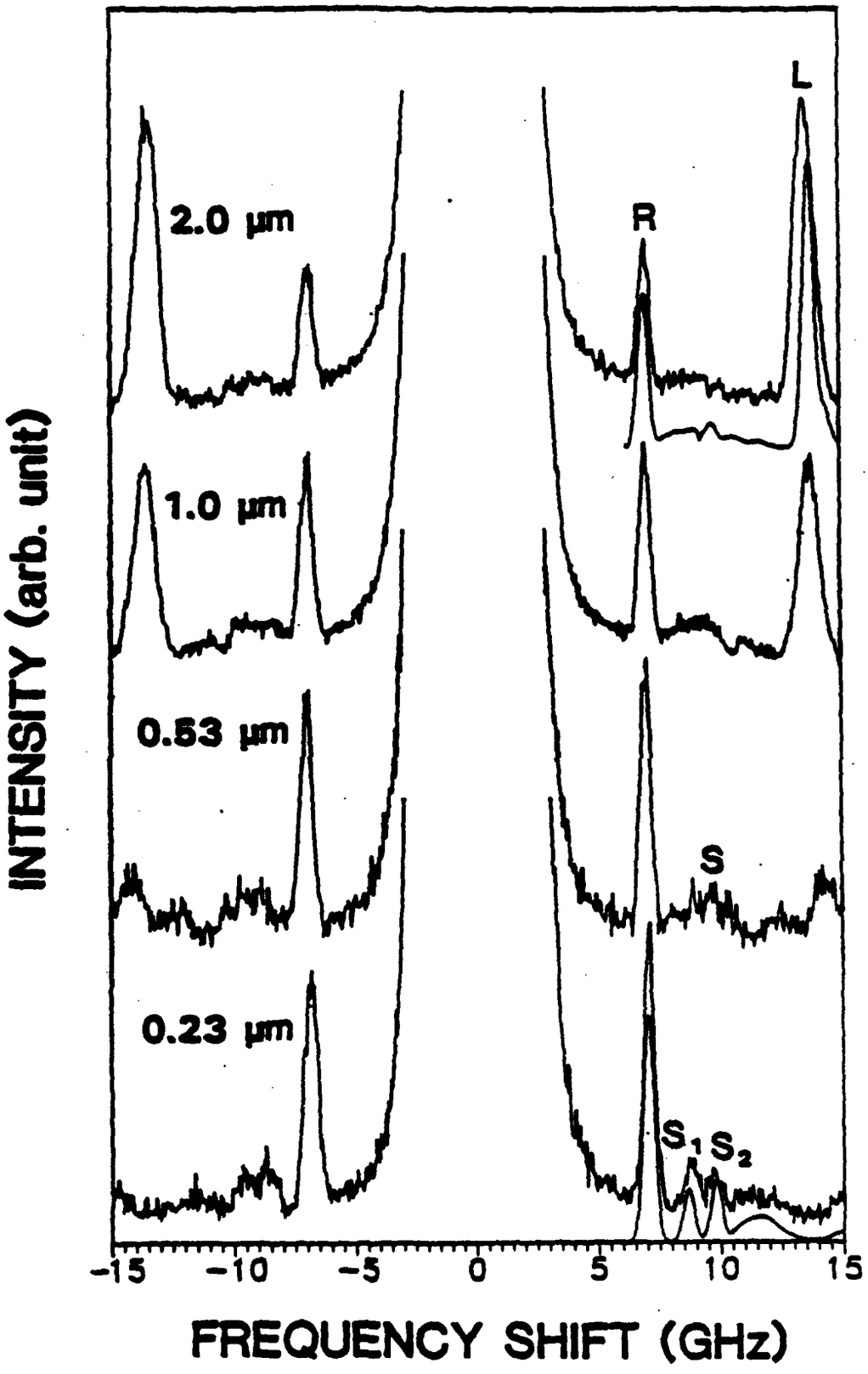
INTENSITY (arb. unit)
2.0 μm
1.0 μm
0.53 μm
0.23 μm
L
R
S
S1 S2
-15
-10
-5
0
5
10
15
FREQUENCY SHIFT (GHz)



Figure 1

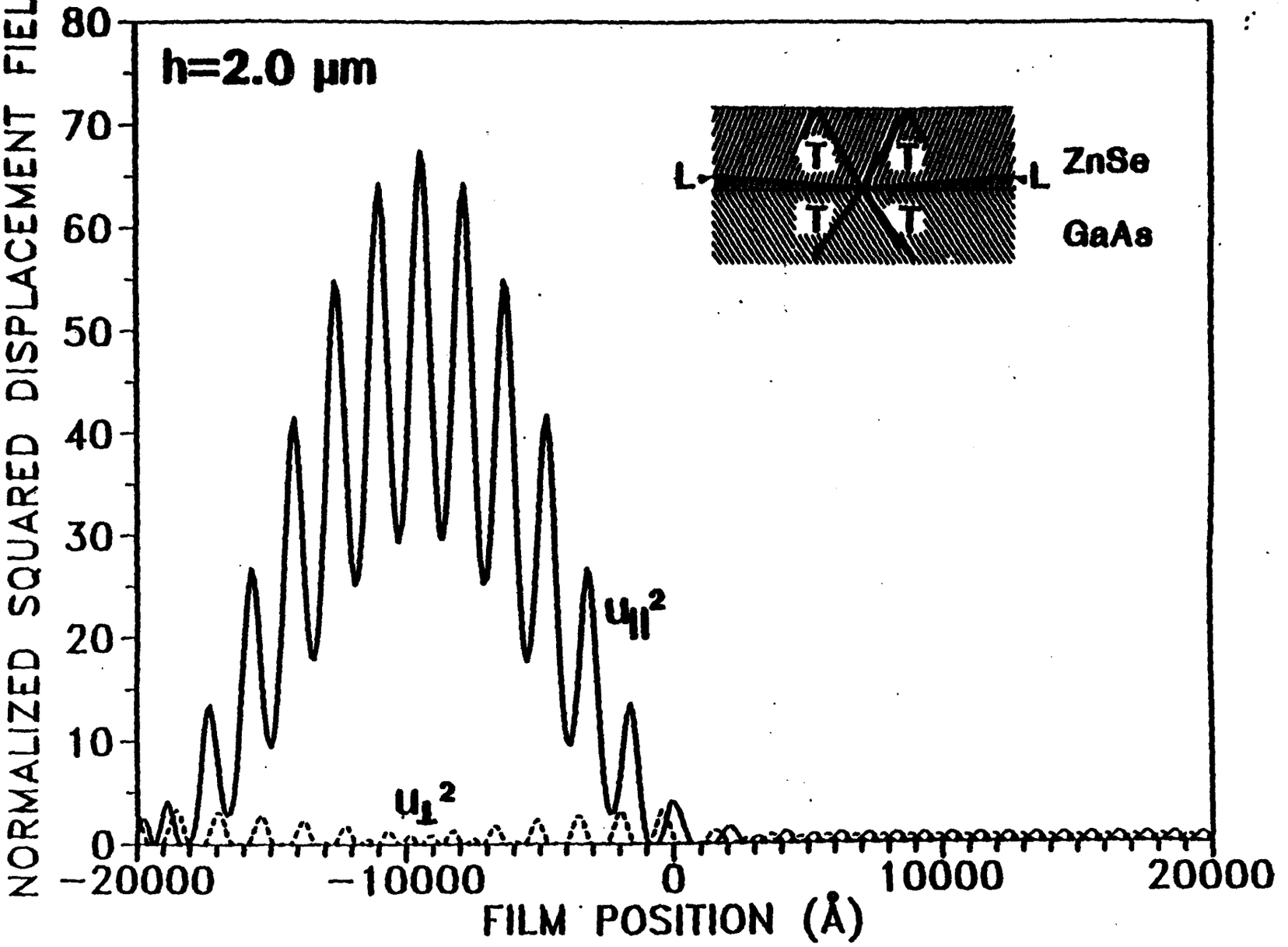
h=2.0 μm
NORMALIZED SQUARED DISPLACEMENT FIELD
80
70
60
50
40
30
20
10
0
−20000
−10000
0
10000
20000
FILM POSITION (Å)
$u_{\parallel}^2$
$u_{\perp}^2$
L
T
T
T
T
L
ZnSe
GaAs

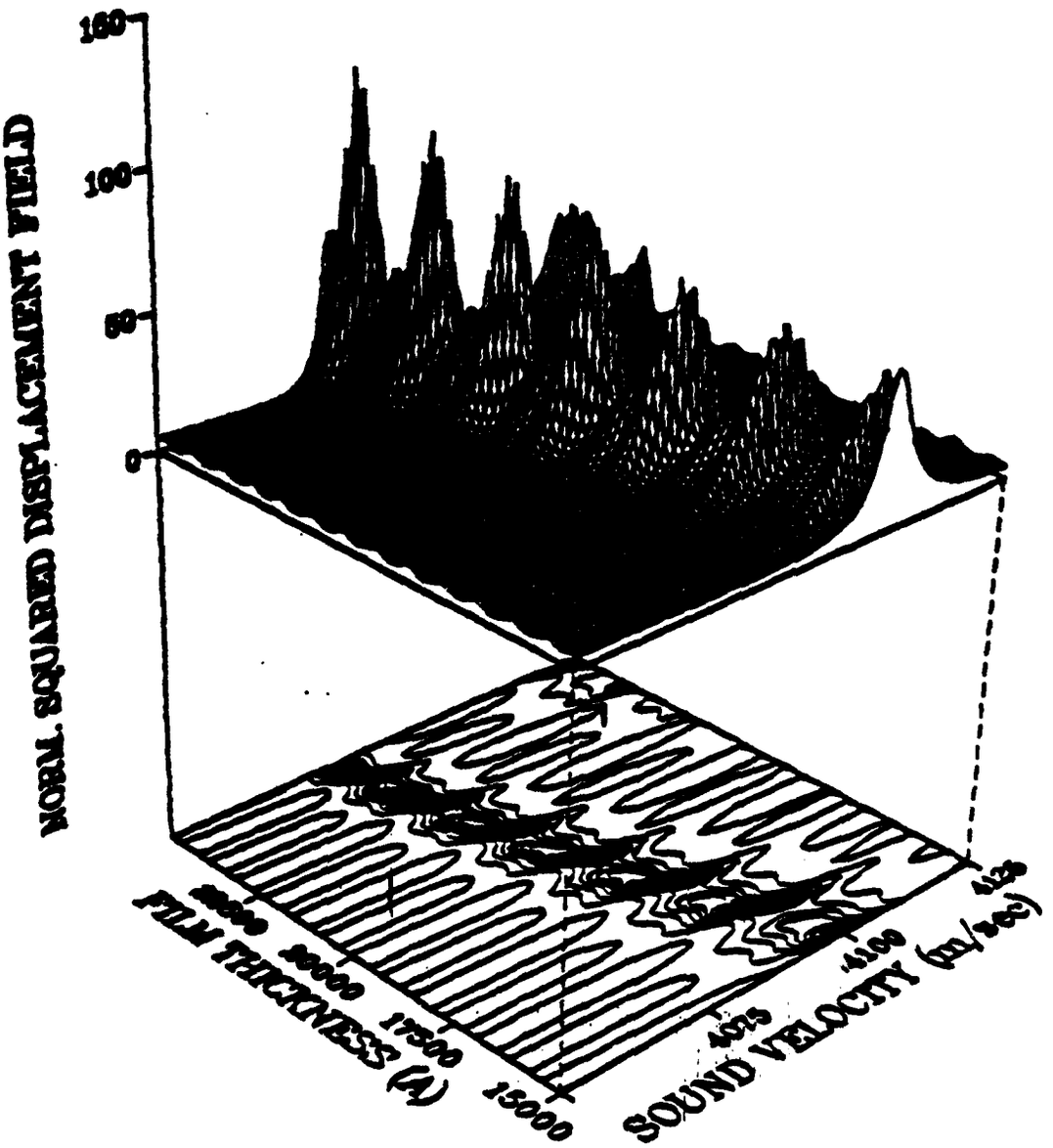
NORM. SQUARED DISPLACEMENT FIELD
160
100
0
FILM THICKNESS (A)
15000
17500
SOUND VELOCITY (m/sec)
4075
4125

# APPENDIX G

# BRILLOUIN SCATTERING FROM COLLECTIVE SPIN WAVES IN MAGNETIC SUPERLATTICES (invited)

B. Hillebrands

Optical Sciences Center, University of Arizona, Tucson, AZ 85721

A. Boufelfel, C.M. Falco

Dept. of Physics and Optical Sciences Center, University of Arizona, Tucson, AZ 85721

P. Baumgart, G. Güntherodt

II. Physikalisches Institut, Universität Köln, 5000 Köln 41, Federal Republic of Germany

E. Zirngiebl, J.D. Thompson

Los Alamos National Laboratory, Los Alamos, NM 87545

We report on the observation and the analysis of collective magnetostatic spin-wave excitations in magnetic superlattices. The influence of interface anisotropies, which can become dominant for small modulation wavelengths, is discussed. For the system Fe/Pd we show that Brillouin spectroscopy experiments in combination with the measurement of the saturation magnetization by a SQUID magnetometer give evidence for a magnetic polarization of the Pd spacer layers, as well as for a small negative out-of-plane interface anisotropy constant of $K_s$ = -0.15 erg/cm$^2$.

PACS-Numbers: 75.30.Ds, 75.30.Gw, 75.70.-i, 87.35.+c

Magnetic multilayered structures have gained considerable interest in the past few years due to their unusual magnetic properties. Besides novel static phenomena like the anti-phase domains in Gd/Y superlattices[1] and the spin spiral effects in Dy/Y superlattices[2] the so-called collective spin wave excitations are the first and the only dynamic collective features of superlattices reported so far.[3–10] In most cases they are made up from surface spin-waves in each magnetic layer coupled by their dipolar stray fields via the intervening nonmagnetic spacer layers giving rise to a new kind of spin-wave band, which exhibits partially bulk-mode- as well as surface-mode-like behavior. A study of these excitations can reveal information about the magnitude and the direction of the saturation magnetization, about magnetic anisotropies, and about a possible polarization of the spacer material. In particular Brillouin spectroscopy seems to be best suited to study magnetic interface anisotropies due to the sensitivity of spin waves to the anisotropy fields. It is therefore of crucial importance to consider Brillouin scattering experiments in addition to established methods of magnetic measurements in order to gain more information about the magnetism of multilayered structures.

So far there are only few reports on the observation of spin waves in magnetic superlattices by Brillouin spectroscopy.[6–10] After theoretical predictions of the existence of the collective modes by Camley et al.,[3] Grünberg and Mika,[4] and by Emtage and Daniel,[5] first experimental evidence was provided by Brillouin scattering experiments in Mo/Ni superlattices by Grimsditch et al.[6] and Kueny et al.[7]. A first detailed experimental proof of the predicted magnetic properties of the collective spin-wave band including measurements of the band shapes was presented by Hillebrands et al. for Fe/Pd and Fe/W superlattices.[8,9]

In this paper we present Brillouin scattering experiments on Fe/Pd superlattices in addition to a brief review of earlier reported results.[8,9] We outline how to fully include

interface anisotropies in the calculation of the spin-wave frequencies and re-analyze within the new model the experimental data of the Fe/Pd-system. We demonstrate that a previous description[8,9] of the observed spin-wave frequencies by a decrease of the saturation magnetization $4\pi M_s$ for small modulation wavelengths $\Lambda$ can be improved by the approach of considering a small out-of-plane interface anisotropy assuming a value of $4\pi M_s = 17 \pm 2$ kG independent of $\Lambda$. A recently reported strong increase of $4\pi M_s$ for small $\Lambda$, as measured by den Broeder et al. using a vibrating sample magnetometer,[11] can consistently be described by the assumption of a magnetic polarization of the Pd spacer layers. The interpretation is corroborated by magnetization measurements in magnetic fields parallel and perpendicular to the layers using a SQUID magnetometer.

The Brillouin scattering experiments were performed at room temperature under vacuum in backscattering geometry using a (3+3)-pass tandem Fabry-Perot interferometer described elsewhere.[13] A single-mode 5145 Å $Ar^+$ ion laser was used with an incident power of p-polarized light of up to 250 mW. The sampling time per spectrum was typically 5 h. The inelastically scattered light was analyzed depolarized in order to suppress surface phonon signals. The applied magnetic field was oriented parallel to the layer planes and perpendicular to the scattering plane.

The Fe/Pd superlattice samples were prepared on single crystal sapphire substrates using a sputtering technique described elsewhere.[14] The sample parameters are listed in Ref. 8. The modulation wavelength $\Lambda$ varies between 33 and 188 Å, and the number of bilayers N varies between 49 and 90. The modulation wavelengths of the different samples were determined by x-ray diffraction. As shown by Bragg and wide-film Debye-Scherrer x-ray diffraction the layers grew with a preferred orientation of bcc Fe(110) planes and fcc Pd(111) planes, with no in-plane orientation. The samples exhibited long-range structural coherence of at least 300 Å perpendicular to the layers.

In Figs. 1 and 2 typical Brillouin spectra of magnetic superlattices are displayed for an applied magnetic field of 1 kG. Fig. 1a shows the spectrum of a Fe/Pd superlattice with a modulation wavelength of $\Lambda$ = 46.2 Å. The thickness d of the magnetic material is close to that of the nonmagnetic material ($d_0$). The band of collective spin-wave excitations can clearly be identified in the right-hand part of the spectrum by its specific asymmetric shape. The density of states is largest at small frequency shifts and decreases asymmetrically toward the upper band edge. At the latter discrete spin-wave modes can still be resolved due to the small thickness and the finite number of bilayers.[8,9] Their strong Stokes/anti-Stokes asymmetry identifies them as surface-mode-like spin waves. On the other hand, the modes near the lower edge of the spin-wave band are bulk-mode-like because of their small Stokes/anti-Stokes asymmetry. If we neglect the discrete modes near the upper band edge the shape of the spin-wave excitation band is qualitatively similar to the calculated Brillouin scattering cross section for the semi-infinite superlattice system Mo/Ni.[3]

In Fig. 1b we show the Brillouin spectrum of an Fe/Pd superlattice with d = 41.7 Å and a much larger $d_0$ = 138.7 Å. In this case the spin-wave band becomes narrower and no discrete peaks are observable near the upper band edge. A drastically different spectrum is found for the case of $d_0$ (9.1 Å) much smaller than d (41.0 Å) as shown in Fig. 1c. In this case a very intense discrete mode is found near 27.7 GHz in the anti-Stokes spectrum. This superlattice surface spin-wave mode, which travels about the total superlattice stack, is allowed to exist besides the collective spin-wave band.[3-5] It would merge with the latter for $d = d_0$.

The effect of inverting the applied magnetic field on the Brillouin cross section is demonstrated in Fig. 1d. Since the direction of the applied field defines the sense of revolution of each surface spin-wave mode about each magnetic layer, an inverted field

exchanges the Stokes and anti-Stokes parts of the spectra.

Fig. 2 shows Brillouin spectra of a Fe/Pd superlattice sample with d = 89.4 Å and $d_0$ = 99.0 Å for different applied magnetic fields H. With increasing H the spin-wave frequencies increase, accompanied by a band-width narrowing.

Since the thickness of each magnetic layer in the superlattices considered here is as low as 16 Å for the smallest modulation wavelength, an influence of interface anisotropies on the spin-wave frequencies cannot generally be excluded. For a single epitaxial layer of epitaxial Fe(110) on a W(110) substrate prepared in UHV by electron beam evaporation and *in situ* measured by Brillouin scattering an *increase* of the spin-wave frequencies toward smaller Fe thicknesses has been observed for d < 60 Å.[15] Using a modified Damon-Eshbach theory, which includes properly the magnetic in-plane and out-of-plane anisotropy contributions, a quantitative description of the observed mode behavior could be achieved. From a fit of the experimental data the anisotropy constants could be determined.[15]

In the following we will describe the theory used in the present work on magnetic superlattices, which includes magnetic interface anisotropy contributions. It is an extension of a theoretical approach described elsewhere,[12] which allows in the magnetostatic limit for the calculation of spin-wave frequencies of superlattices under the inclusion of volume anisotropy contributions described by the volume anisotropy constant $K_1$ and an uniaxial anisotropy constant $K_U$. We dropped contributions from the latter, since there is no evidence in the superlattices for uniaxial contributions, which cannot be described more adequately by surface anisotropies. Exchange contributions are neglected.[3–5,10,12]

Since the Fe layers investigated here all have the (110) planes parallel to the interfaces of the superlattice, we restrict ourselves in the following to this case. We will use a spherical coordinate system, where $\Theta$ is the azimuthal angle measured against the interface normal and $\Phi$ is the polar angle measured with respect to the crystallographic [001] axis in the layer plane. The free energy density[16-18] of the system consists of i) the potential energy density $f_p$ of the magnetization $M_s$ in the external field H,

$$f_p = - M_s H \sin\Theta \cos(\Phi_H - \Phi) , \tag{1}$$

where $\Phi_H$ is the angle between the crystallographic [001] direction in the surface and the external field H, ii) the free energy density $f_v$ due to volume anisotropies,

$$f_v = \frac{K_1}{4}\left\{ \cos^4\Theta + \sin^4\Theta\,[\,\sin^4\Phi + \sin^2(2\Phi)] + \sin^2(2\Theta)\left[\cos^2\Phi - \frac{1}{2}\sin^2\Phi\right]\right\}, \tag{2}$$

and iii) the free energy density $f_i$ due to interface anisotropies in the homogeneous magnetization approximation,[19]

$$f_i = \frac{2}{d}(K_s \cos^2\Theta + K_{s,p} \sin^2\Theta \cos^2\Phi) , \tag{3}$$

where d is the thickness of the magnetic layers and the factor 2 counts the two interfaces. $K_s$ and $K_{s,p}$ are the out-of-plane and the in-plane anisotropy constants, respectively. Since the films considered here are isotropic in plane, we have to average Eqs. 1-3 over the in-plane angle $\Phi$:

$$f_p^{iso} = - M_s H \sin \theta \,. \tag{4}$$

$$f_v^{iso} = \frac{K_1}{4} \left[ \frac{7}{8} \sin^4 \theta + \cos^2 \theta \right]. \tag{5}$$

$$f_i^{iso} = \frac{2}{d} \left[ K_s \cos^2 \theta + \frac{1}{2} K_{s,p} \sin^2 \theta \right]. \tag{6}$$

With the resulting free energy density f,

$$f = f_p + f_v + f_i \,. \tag{7}$$

we are now able to determine the components of the dynamic susceptibility tensor $\chi$:[16–18]

$$\chi_{11} = \frac{4 \pi \gamma^2 f_{\phi\phi}}{\Omega^2 \sin^2 \theta} \,. \tag{8}$$

$$\chi_{12} = \frac{4 \pi}{\Omega^2} \left[ \frac{\gamma^2 f_{\theta\phi}}{\sin \theta} - i \gamma M_s \right]. \tag{9}$$

$$\chi_{21} = \frac{4 \pi}{\Omega^2} \left[ \frac{\gamma^2 f_{\theta\phi}}{\sin \theta} + i \gamma M_s \right]. \tag{10}$$

$$\chi_{22} = \frac{4 \pi \gamma^2 f_{\theta\theta}}{\Omega^2} \,. \tag{11}$$

with

$$\Omega^2 = \omega_0^2 - \omega^2 , \tag{12}$$

$$\omega_0 = \frac{\gamma}{M_S \sin\theta} \sqrt{f_{\theta\theta} f_{\phi\phi} - f_{\theta\phi}^2} , \tag{13}$$

where $f_{\mu\nu}$ refer to the second derivatives of $f$ with respect to $\mu$ and $\nu$. $\gamma$ is the gyromagnetic ratio and $\omega$ the spin-wave frequency. Since for all superlattices considered in this work the magnetization has no out-of-plane component (see below) we may assume in the following $\theta = 90^0$. The evaluated expressions for $f_{\theta\theta}$, $f_{\phi\phi}$ and $f_{\theta\phi}$ are

$$f_{\theta\theta} = M_S H - \frac{3}{8} K_1 + \frac{4}{d} \left[ K_S - \frac{1}{2} K_{S,p} \right] , \tag{14}$$

$$f_{\phi\phi} = M_S H , \tag{15}$$

$$f_{\theta\phi} = 0 . \tag{16}$$

It should be pointed out, that due to the (110) orientation of the crystallites in each magnetic film the anisotropy contributions do not average to zero. However, only a linear combination of the three anisotropy constants enters the calculation, contrary to results of epitaxial films, where the constants enter independently in $f_{\theta\theta}$ and $f_{\phi\phi}$.[15]

The rest of the calculation is straightforward. Solving Maxwell's equations in the magnetic and nonmagnetic layers and taking the magnetic boundary conditions at each interface into account, the problem of finding solutions for propagating spin waves can be reduced to finding the zeros of the boundary-condition determinant. Since at each

interface only magnetic interactions between the adjacent layers have to be considered the boundary-condition determinant can be written in the form of a band matrix. This allows to apply very effective numerical tools in order to efficiently calculate the spin-wave frequencies even for 90 bilayers.

The parallel component of the spin-wave wave-vector, $q_{||}$, is defined by the scattering geometry of the Brillouin scattering experiment. The perpendicular component $q_{\perp}$ is given in each layer by the relation[12]

$$q_{\perp} = q_{||} \sqrt{-\frac{1 + \chi_{22} \sin^2 \alpha}{1 + \chi_{11}}} , \qquad (17)$$

where $\alpha$ is the angle between $q_{||}$ and $4\pi M_s$. In the absense of surface anisotropies $q_{\perp}$ is always imaginary, resulting in surface spin-wave modes. However, in particular for small magnetic thicknesses and large positive surface anisotropy contributions, $q_{\perp}$ can become real and the spin waves have bulk-like character in the corresponding layer.

Figs. 3 and 4 show results of the calculations. We used the parameters obtained from the fit of the spin-wave frequencies in single epitaxial Fe(110) films on W(110) reported in Ref. 15. The parameters are given in Figs. 3 and 4. Fig. 3 shows the obtained spin-wave frequencies for a N=10 superlattice as a function of the Fe layer thickness d, which is equal to the thickness $d_0$ of the nonmagnetic spacer material. As in the case of single layers the spin-wave frequencies increase for small d. The mode of highest frequency, which is the surface spin-wave mode revolving about the total superlattice stack, shows an overall frequency increase with decreasing d and is well separated from the residual modes. Contrary to the case of vanishing interface anisotropies, this

mode cannot be described as a surface spin wave of a magnetic layer of a thickness equal to the total thickness of the superlattice stack,[3-5] since in the latter case the surface anisotropy contribution should be negligible due to the 1/d factor. All residual modes are nearly degenerate in frequency for very small d. An analysis of the wave solutions in each layer shows, that due to the dominating interface anisotropy terms the spin waves are bulk-mode-like in each layer, which compared to surface modes have smaller dipolar stray fields in the nonmagnetic spacer layers and are thus less coupled to each other.

Fig. 4 shows the spin-wave frequencies of a N=10 superlattice with $d = d_0 = 30\text{Å}$ as a function of the surface anisotropy constant $K_S$. In the plotted range the energy contribution of the surface anisotropy is too small to turn the magnetization out of plane for negative values of $K_S$. With increasing $K_S$ the spin-wave frequencies increase, whereas for negative values of $K_S$ the spin-wave frequencies are reduced.

In order to test the influence of interface anisotropies in Fe/Pd superlattices as well as to address the above described discrepancies in the reported values of the saturation magnetization,[8,9,11] we have re-analyzed the previously measured Brillouin scattering data using the new model. In order to support the reported increased values of the saturation magnetization for vapor-deposited Fe/Pd superlattices of Fe thicknesses between 2 and 6 Å (Ref. 11) we also measured for some of our samples $4\pi M_S$ and the saturation field (kink field) $H_S$ by means of a SQUID magnetometer for applied magnetic fields H up to 54 kG parallel as well as perpendicular to the layers. The results from the SQUID measurements are listed in Table 1 together with those from Ref. 11. For all samples we obtained higher values of the saturation magnetization as compared to the Brillouin scattering results reported in Refs. 8 and 9. Fig. 5 shows a plot of the saturation magnetization obtained from the SQUID measurements as a function of the

inverse Fe thickness 1/d including the data from Ref. 11, except sample 1/8.2. The values of $4\pi M_s$ of each superlattice sample have been obtained by dividing the measured magnetic moment by the total Fe volume. The data points lie roughly on a straight line, which can be described by

$$4\pi M_s(d) = 4\pi M_s(d=\infty)\left[1 - \frac{d_s}{d}\right], \tag{18}$$

where $d_s$ is the amount, by which the thickness of the magnetic layers differs from that of the Fe layers. $4\pi M_s(\infty)$ is the intrinsic magnetization of Fe. An extrapolation of this line into the regime of the data of Ref. 11 agrees with the latter, in particular with the sample of largest Fe thickness (d = 6 Å). The line is given by $4\pi M_s(\infty) = 14.5 \pm 1.5$ kG and $d_s = -1.5$ Å, assuming a uniform magnetization across the total magnetic thickness. The negative value of $d_s$ implies that the thickness of the magnetically active material is larger than the Fe thickness, i.e. that Pd is magnetically polarized. However, since in the Pd material only the product of $4\pi M_s(\infty)$ of Pd and $d_s$ enters Eq. (18), we cannot determine each of both factors independently.

An intrinsic saturation magnetization, which is independent of $\Lambda$, allows for a consistent description of the Brillouin scattering data as well. An increased value of $4\pi M_s$ would result in increased spin-wave frequencies, which, however, are not observed experimentally. On the other hand, a small increase in d with a corresponding decrease in $d_0$ modifies the spin-wave frequencies only slightly.

Assuming therefore the saturation magnetization to be independent of the modulation wavelength $\Lambda$, magnetic anisotropy effects have to account for the observed decrease of the spin-wave frequencies with decreasing $\Lambda$. Since only a linear combination of all

anisotropy constants enters the formula (see Eq. 14 and 15) and $K_{s,p}$ is usually much smaller than $K_s$, we assumed $K_{s,p} = 0$ and for $K_1$ a literature value of $4.8 \cdot 10^5$ erg/cm$^2$.[20] A good fit of the experimental data could be achieved within the experimental error by a value of $4\pi M_s = 17 \pm 2$ kG and an out-of-plane anisotropy constant $K_s = -0.15 \pm 0.03$ erg/cm$^2$. For comparison, an analysis of the saturation field $H_s$ (see Table 1) as a function of 1/d as determined by the SQUID magnetometer yields a value of $K_s = -0.38 \pm 0.1$ erg/cm$^2$. The latter value has the same sign as the value obtained from the Brillouin spectroscopy data. The higher absolute value might be due to the contribution of higher order anisotropy constants, which may show no influence on the spin-wave frequencies.[21] However, both values are too small to rotate the direction of magnetization out of plane. This is confirmed by the absence of hysteresis effects in the perpendicular-field SQUID measurements.

In conclusion, we have shown that the observation of spin-wave spectra in superlattices by Brillouin spectroscopy reveals important information about the magnetic properties of these artificially layered materials. In particular we have demonstrated the influence of interface anisotropies on the spin-wave frequencies which may become dominant for small modulation wavelengths. Since the spin-wave frequencies are sensitive to the intrinsic saturation magnetization, the combination of Brillouin spectroscopy with magnetometric investigations allows potentially for the determination of dead layers as well as polarization of the non-magnetic spacer layers at the interfaces. We applied both types of methods to the Fe/Pd superlattice system. From the comparison of the results a consistent description could be found by assuming a saturation magnetization of 17 ± 2 kG, which is independent of the modulation wavelength, a polarization of the Pd layer at each interface and a small negative out-of-plane interface anisotropy of $K_s = -0.15$ erg/cm$^2$. The obtained value for the saturation magnetization is about 20% smaller than the bulk Fe value of 21 kG, which we attribute to the sputtering process.

Future investigation on both sputtered and MBE-grown Fe/Pd systems will help to clarify this point. Presently the physical origin of the Pd polarization is not clear. The situation is reminiscent of the formation of giant moments,[22] but the physical conditions, i.e. the Fe concentration and the temperature range, are not comparable. From the Bethe-Slater diagram and the lattice constant mismatch, which causes a stretching of the spacing of nearest neighbor Pd atoms by 10 %, the interface mismatch would not give rise to a magnetic moment in the Pd layer. On the other hand, a hybridization of the Pd(d) states with the Fe(d) states is very likely due to the large density of Pd states at the Fermi level, and might account for the observed behavior. A fully self-consistent band structure calculation would be most desirable for this case.

## ACKNOWLEDGEMENTS

We would like to thank G. Rado and G. Stegeman for discussions and support. The work at the University of Arizona was supported by the Air Force Office of Scientific Research / University Research Initiative Program under contract No. F 49620-86-C-0123, and by the Department of Energy - Materials Sciences Division under Contract No. DE-FG02-87-ER45297. The work at the University of Cologne was supported by Deutsche Forschungsgemeinschaft, SFB 125. Work at Los Alamos National Laboratory was performed under the auspices of the Department of Energy.

## REFERENCES


[1] C.F. Majkrzak, J.W. Cable, J. Kwo, M. Hong, D.B. McWhan, Y. Yafet, J.V. Waszczak, C. Vettier, Phys. Rev. Lett. 56, 2700 (1986)

[2] M.B. Salamon, S. Sinha, J.J. Rhyne, J.E. Cunningham, R.W. Erwin, J. Borchers, C.P. Flynn, Phys. Rev. Lett. 56, 259 (1986)

[3] R.E. Camley, T.S. Rahman, D.L. Mills, Phys. Rev. B 27, 261 (1983)

[4] P. Grünberg, K. Mika, Phys. Rev. B 27, 2955 (1983)

[5] P.R. Emtage, M.R. Daniel, Phys. Rev. B 29, 29, 212 (1984)

[6] M. Grimsditch, M.R. Khan, I.K. Schuller, Phys. Rev. Lett. 51, 498 (1983)

[7] A. Kueny, M.R. Khan, I.K. Schuller, M. Grimsditch, Phys. Rev. B 29, 2879 (1984)

[8] B. Hillebrands, P. Baumgart, R. Mock, G. Güntherodt, A. Boufelfel, C.M. Falco, Phys. Rev. B 34, 9000 (1986)

[9] B. Hillebrands, P. Baumgart, R. Mock, G. Güntherodt, A. Boufelfel, C.M. Falco, J. Appl. Phys. 61, 4308 (1987)

[10] G. Rupp, W. Wettling, W. Jantz, R. Krishnan, Appl. Phys. A 37, 73 (1985)

[11] F.J.A. den Broeder, H.C. Donkersloot, H.J.G. Draaisma, W.J.M. de Jonge, J. Appl.Phys. 61, 4317 (1987)

[12] G. Rupp, W. Wettling, W. Jantz, Appl. Phys. A 42 45 (1987)

[13] R. Mock, B. Hillebrands, J.R. Sandercock, J. Phys. E 20, 656 (1987)

[14] C.M. Falco, J. Phys. (Paris) Colloq. 45, C5-499 (1984)

[15] B. Hillebrands, P. Baumgart, G. Güntherodt, Phys. Rev. B 36, 2450 (1987)

[16] G. Rupp, W. Wettling, A.S. Smith, W. Jantz, J. Magn. Magn. Mat 45, 404 (1984)

[17] J.O. Artman, Phys. Rev. 105, 62 (1957)

[18] E.P. Valstyn, I.P. Hanton, A.M. Morish, Phys. Rev. 128, 2078 (1962)

[19] U. Gradmann, J. Korecki, G. Waller, Appl. Phys. A 39, 101 (1986)

[20] E.P. Wohlfarth, in *Ferromagnetic Materials*, E.P. Wohlfarth (ed), (North Holland, Amsterdam 1980)

[21] M.J. Pechan, I.K. Schuller, Phys. Rev. Lett. 59, 132 (1987)

[22] J. Crangle, W.R. Scott, J. Appl. Phys. 36, 921 (1965)

## TABLE CAPTION

**Table 1:**

**Parameters and results of the Fe/Pd superlattices investigated by SQUID measurements. $n_{Fe}$ ($n_{Pd}$): number of atomic Fe (Pd) layers per bilayer; Λ: modulation wavelength; $4\pi M_s$: measured SQUID values of the saturation magnetization; $\mu_0 H_K$: perpendicular saturation field.**

## FIGURE CAPTIONS

**Figure 1:**

**Room temperature Brillouin spectra of Fe/Pd superlattices in an applied magnetic field of 1 kG: (a) d = 21.9 Å and $d_0$ = 24.3 Å, (b) d = 41.7 Å and $d_0$ = 138.7 Å, and (c,d) d = 41.0 Å and $d_0$ = 9.1 Å. In (d) the direction of the applied field has been reversed compared to (c). The angle of incidence of the laser beam is 45°.**

**Figure 2:**

Room temperature Brillouin spectra of a Fe/Pd superlattice consisting of 49 bilayers with d = 89.4 Å and $d_0$ = 99.0 Å for different applied magnetic fields as indicated in the Figure. The angle of incidence of the laser beam is 45°.

**Figure 3:**

Calculated spin-wave frequencies as a function of the layer thickness for a N=10 superlattice with equal thicknesses of the magnetic and nonmagnetic layers. The parameters are as indicated in the Figure.

**Figure 4:**

Calculated spin-wave frequencies as a function of the out-of-plane interface anisotropy constant $K_s$. The parameters are as indicated in the Figure.

**Figure 5:**

Values of the saturation magnetization obtained from the SQUID measurements (crosses) and values from Ref. 11 (circles) as a function of the inverse Fe thickness. The solid line is a fit to our data and the dashed line is an extrapolation into the regime of the data of Ref. 11.

Table 1:

| $n_{Fe}/n_{Pd}$ | number of bilayers | $\Lambda$ (Å) | $4\pi M_s$ (kG) | $\mu_0 H_k$ (kG) |
|---|---|---|---|---|
| 44/44 | 49 | 188.4 | 15.6 | 20.0 |
| 20/20 | 70 | 86.8 | 16.9 | 17.2 |
| 10/10 | 90 | 42.2 | 19.2 | 14.7 |
| 3/8.2† | 125 | 26.5 | 27.0 | 11.0 |
| 2/8.2† | 136 | 24.4 | 27.4 | 8.5 |
| 1/8.2† | 150 | 22.2 | 25.2 | 4.6 |

† data from den Broeder et al.[11]

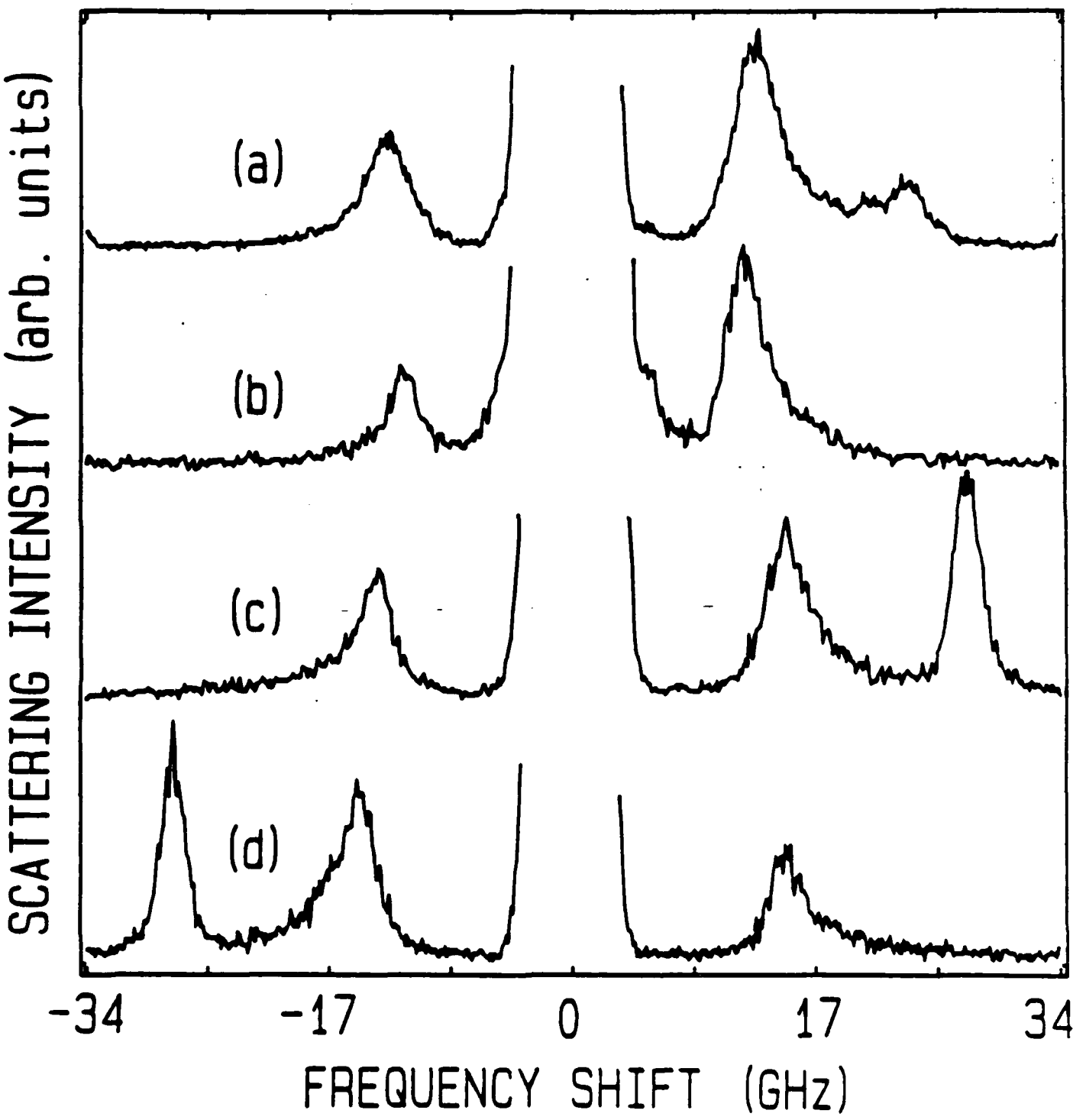
SCATTERING INTENSITY (arb. units)
(a)
(b)
(c)
(d)
-34
-17
0
17
34
FREQUENCY SHIFT (GHz)



Fig. 1

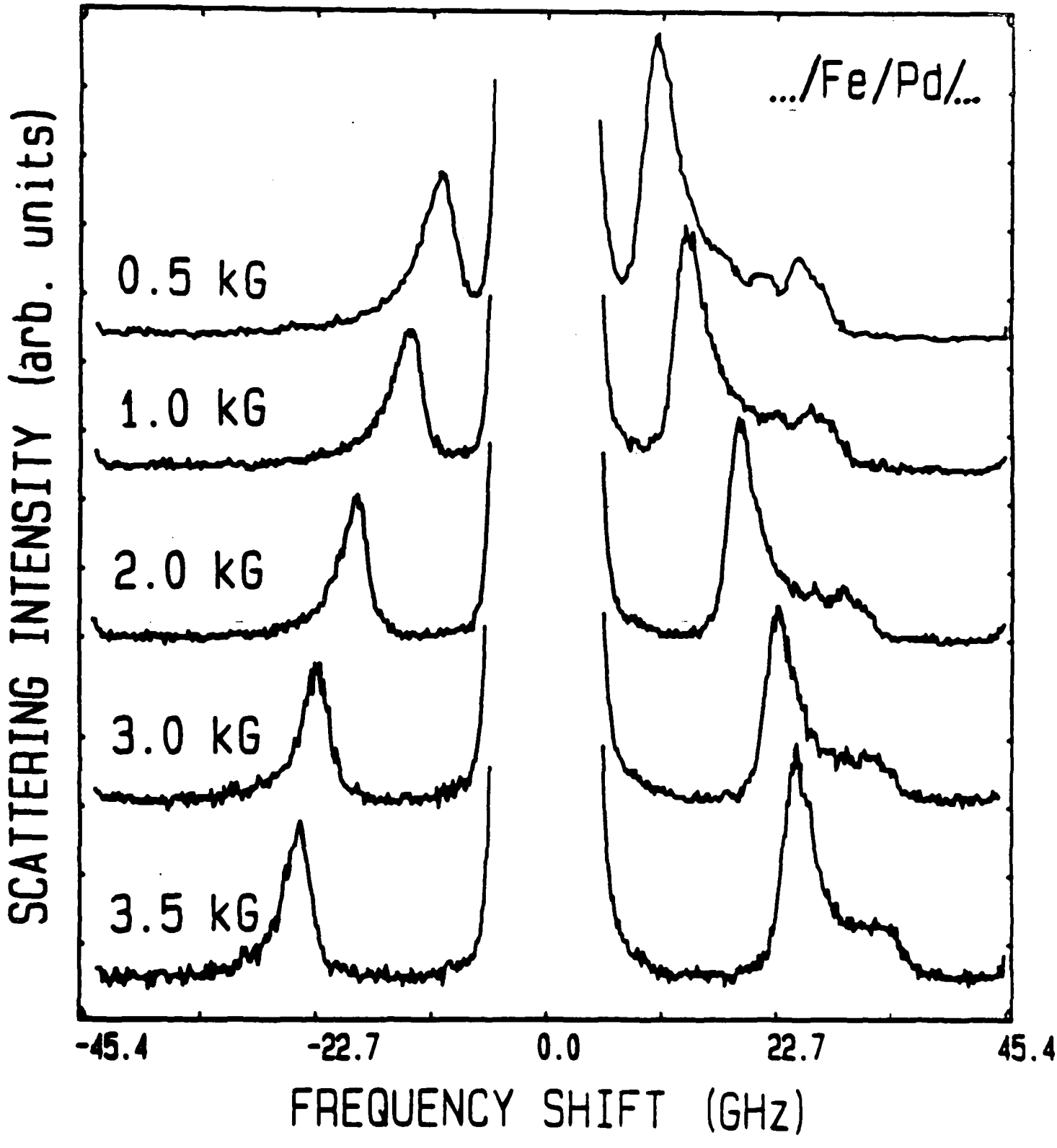
.../Fe/Pd/...
0.5 kG
1.0 kG
2.0 kG
3.0 kG
3.5 kG
SCATTERING INTENSITY (arb. units)
-45.4
-22.7
0.0
22.7
45.4
FREQUENCY SHIFT (GHz)



Fig. 2

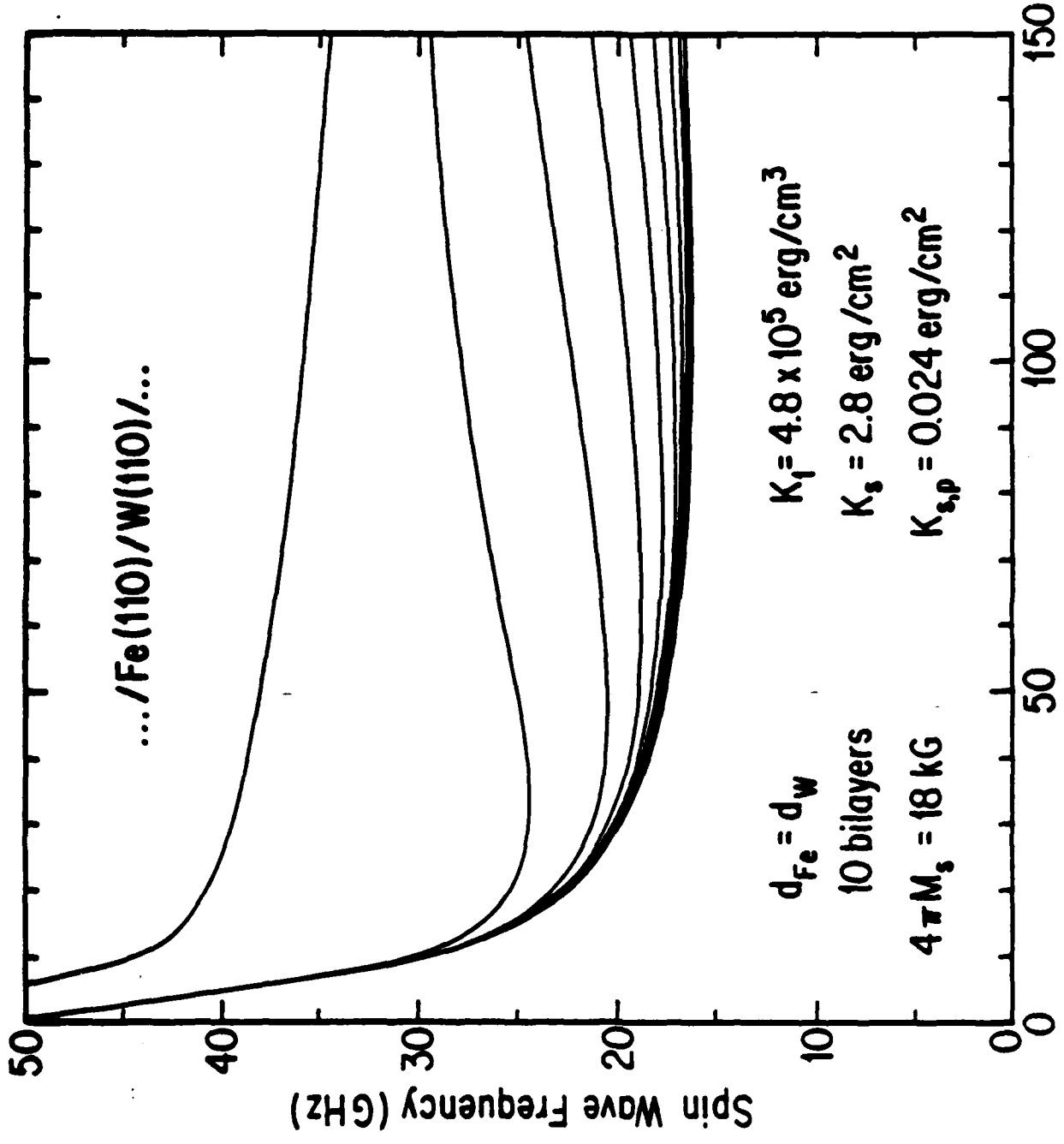
.../Fe(110)/W(110)/...
$d_{Fe} = d_W$
10 bilayers
$4\pi M_s = 18$ kG
$K_1 = 4.8 \times 10^5$ erg/cm$^3$
$K_s = 2.8$ erg/cm$^2$
$K_{s,p} = 0.024$ erg/cm$^2$
Spin Wave Frequency (GHz)
Fe Film Thickness (Å)
0
10
20
30
40
50
0
50
100
150

Fig. 3

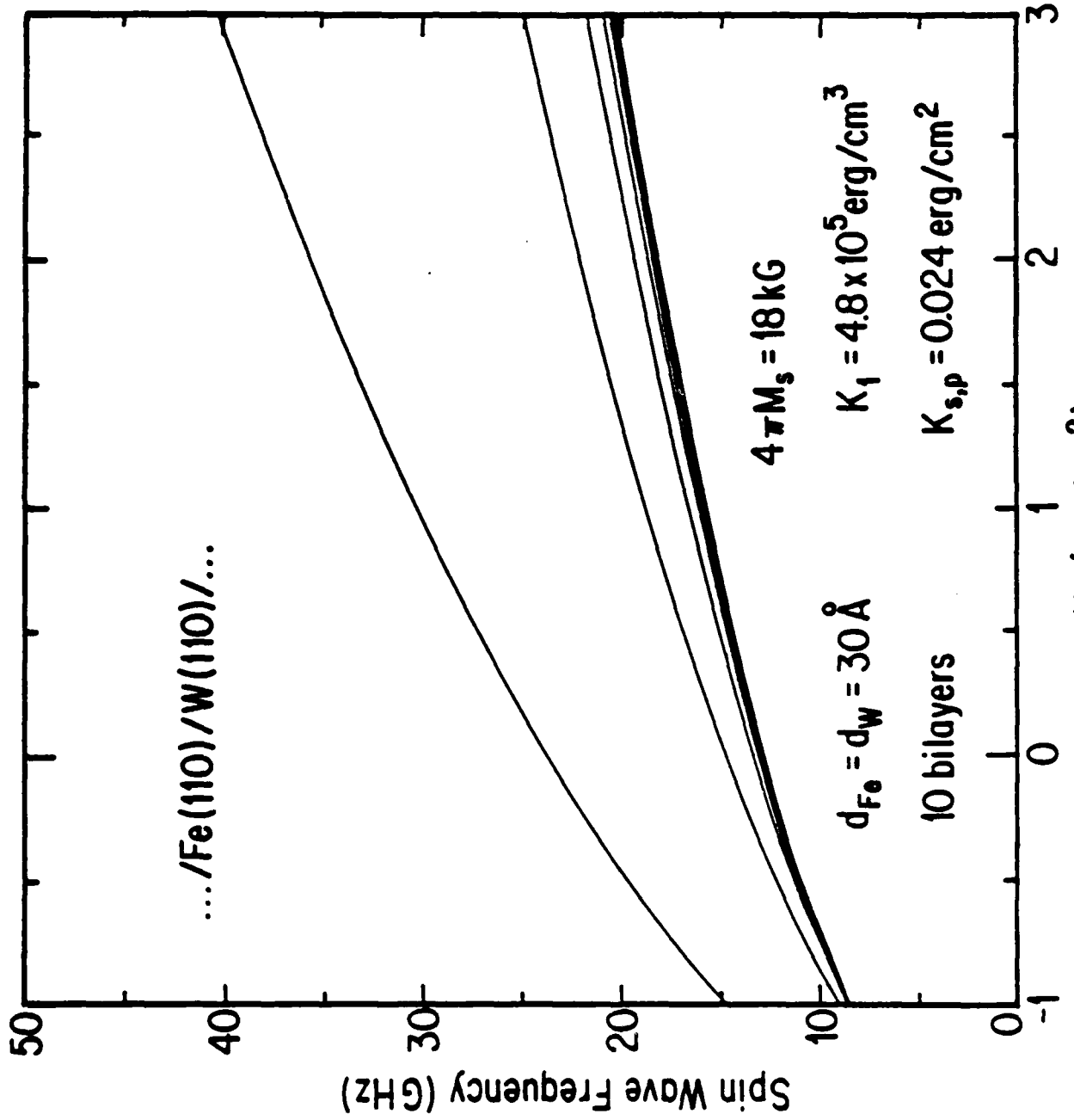
Spin Wave Frequency (GHz)
50
40
30
20
10
0
-1
0
1
2
3
$K_s$ (erg/cm$^2$)
..../Fe(110)/W(110)/...
$4\pi M_s = 18$ kG
$K_1 = 4.8 \times 10^5$ erg/cm$^3$
$K_{s,p} = 0.024$ erg/cm$^2$
$d_{Fe} = d_W = 30$ Å
10 bilayers

Fig. 4

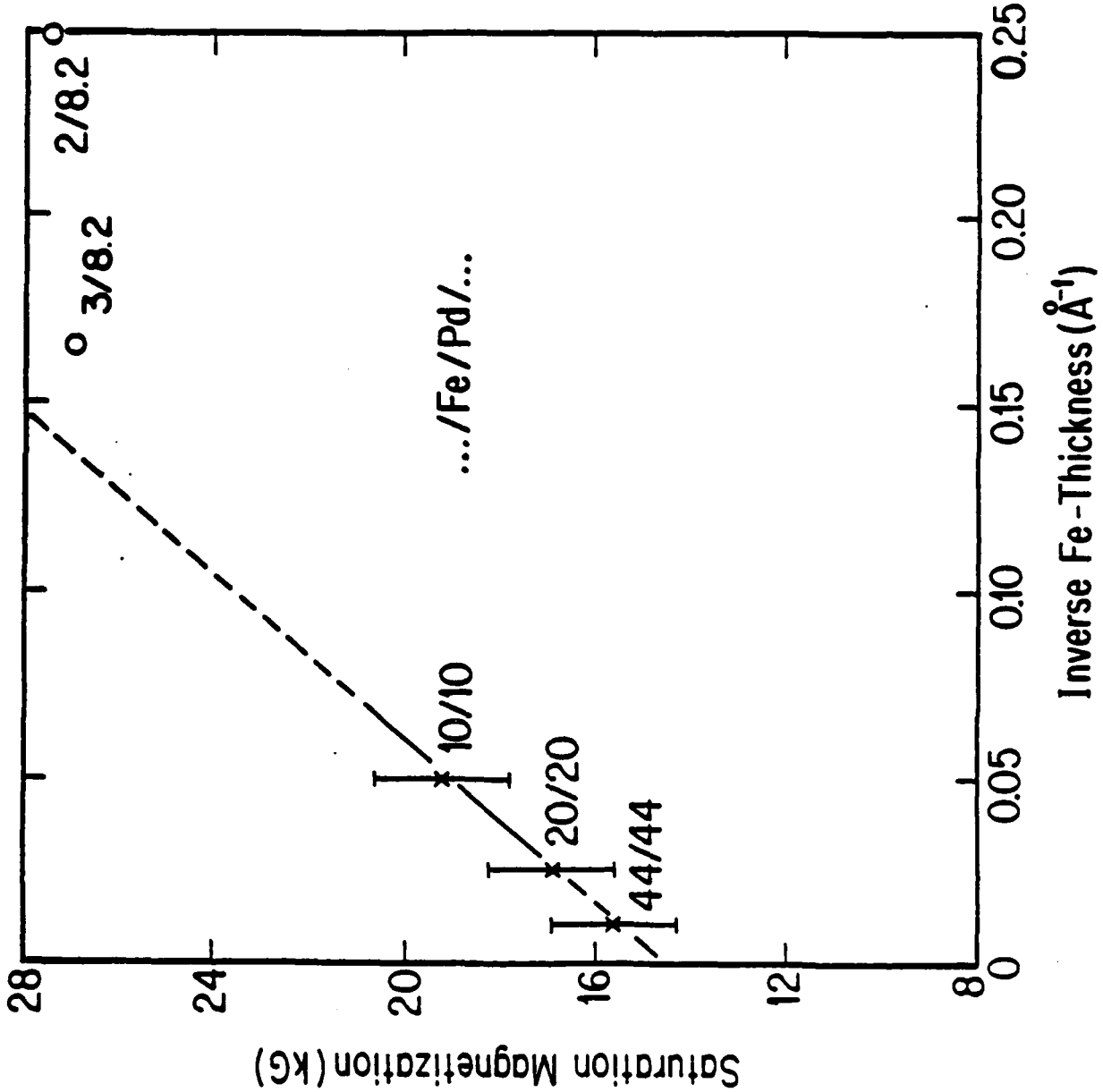
Saturation Magnetization (kG)
28
24
20
16
12
8
0
0.05
0.10
0.15
0.20
0.25
Inverse Fe-Thickness (Å⁻¹)
.../Fe/Pd/...
o 3/8.2
2/8.2
10/10
20/20
44/44

Fig. 5

FIGURE 4

HIGH ENERGY 3.8 MEV BACK-SCATTERING SPECTRUM OF A THIN YBaCuO FILM (SAMPLE B) ON AN ALUMINUM OXIDE SUBSTRATE. THE Cu,Y AND Ba SIGNALS ARE WELL RESOLVED. THE OXYGEN SIGNAL IS UNOBSERVABLE.

AC091087 3776 KeV He4 on Sample: S-910-A [B] 4 K COUNTS FS

Q' = 50.03 uC DTR = 1.01 Phi = 0 Theta = 170 Omega = ( .78 +/- 0.02) msr

e = ( )KeV/Ch. E' = ( )KeV CF Bi = ( .99 +/-0.03)

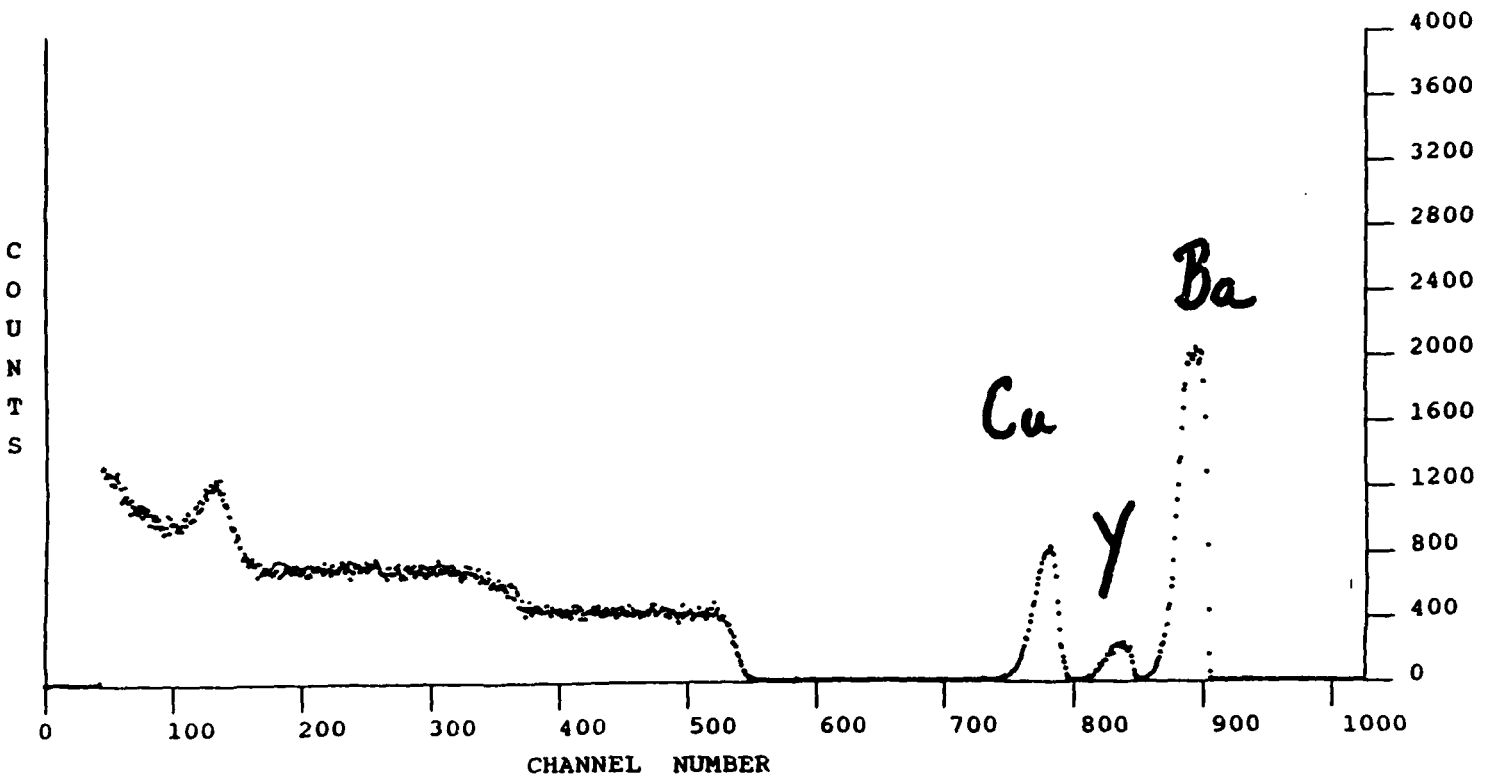

# TABLE 2

## RESULTS FOR SAMPLE B

| ELEMENT | Nt | REL. ATOMIC % |
|---|---|---|
| Y | 2.10±0.06 | 23.0±0.1 |
| Ba | 2.63±0.08 | 28.8±0.1 |
| Cu | 4.40±0.13 | 48.2±0.2 |

Nt = AREAL DENSITY (E17 ATOMS/SQ CM)

FIGURE 5

PORTION OF THE HIGH ENERGY
4.7 MEV BACKSCATTERING SPECTRUM
OF A THIN YBaCuO FILM (SAMPLE D)
SHOWING INTERFERENCE OF THE Cu,
Y AND Ba SIGNALS.

AD091087 4700 KeV He4 on Sample: S-910-B [B] 4 K COUNTS FS

Q' = 50.04 uC DTR = 1.021 Phi = 0 Theta = 170 Omega = ( .78 +/- 0.02) msr

e = ( )KeV/Ch. E' = ( )KeV CF Bi = ( .99 +/-0.03)

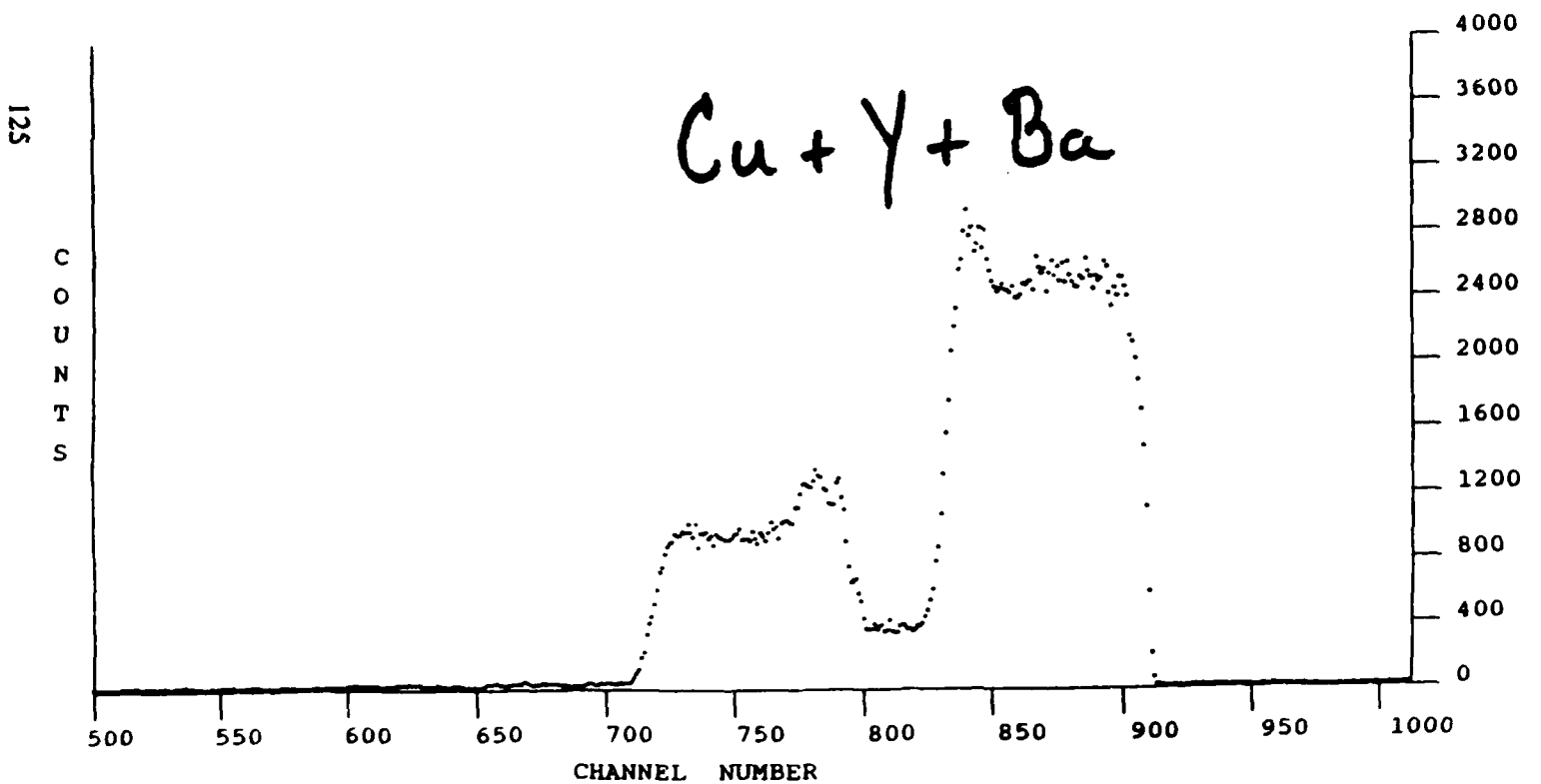

FIGURE 6

COMPUTER DECONVOLUTION OF THE INTERFERING Cu,Y AND Ba SIGNALS SHOWN IN FIGURE 5.

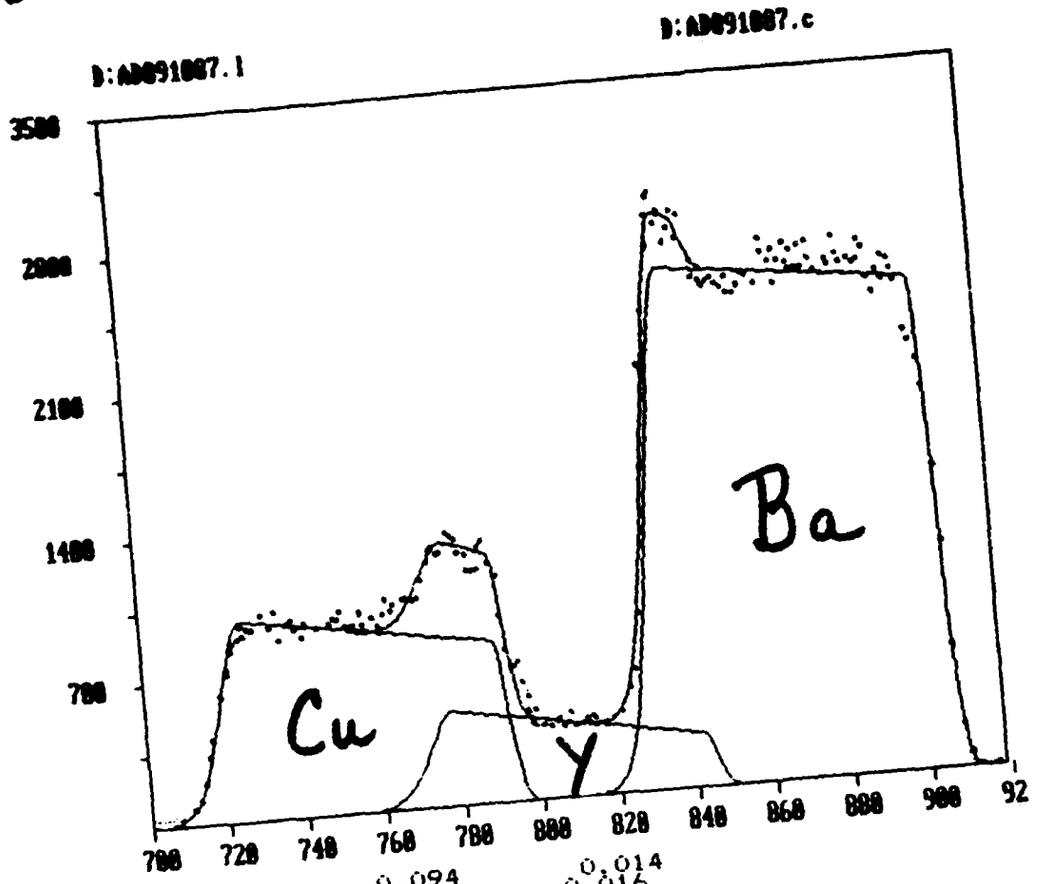


| | | | |
|---|---|---|---|
| 6 | 6.576 | 0.094 | 0.014 |
| 7 | 2.901 | 0.046 | 0.016 |
| 8 | 726.250 | 0.169 | 0.000 |
| 9 | 790.676 | 0.120 | 0.000 |
| 10 | 779.418 | 0.34 | 0.000 |
| 11 | 844.007 | 0.6 | 0.001 |
| 12 | 840.091 | 0.14 | 0.000 |
| 13 | 904.711 | 0.089 | 0.000 |
| 14 | 2409.190 | 12.548 | 0.005 |

chisq= 5.12

left area= 68369.99 +/- 1001.825

center area= [illegible] +/- 1130.327

right area= 189858.95 +/- 1158.088

total area= 286556.34 +/- 1903.223

# TABLE 3

## RESULTS FOR SAMPLE D

| ELEMENT | Nt | REL. ATOMIC % |
|---|---|---|
| Y | 3.14±0.15 | 11.6±0.3 |
| Ba | 10.2±0.3 | 37.6±0.3 |
| Cu | 13.8±0.5 | 50.8±0.4 |

Nt = AREAL DENSITY (E17 ATOMS/SQ CM)

# FIGURE 7

FITTING FUNCTION REPRESENTING THE BACKSCATTERING SPECTRUM OF A SINGLE ELEMENT. PARAMETERS 1 AND 2 ARE WIDTHS OF LEFT AND RIGHT HALF-GAUSSIANS; PARAMETERS 3,4,5 AND 6 ARE HEIGHTS AND LOCATIONS OF THE CENTRAL TRAPEZOID.

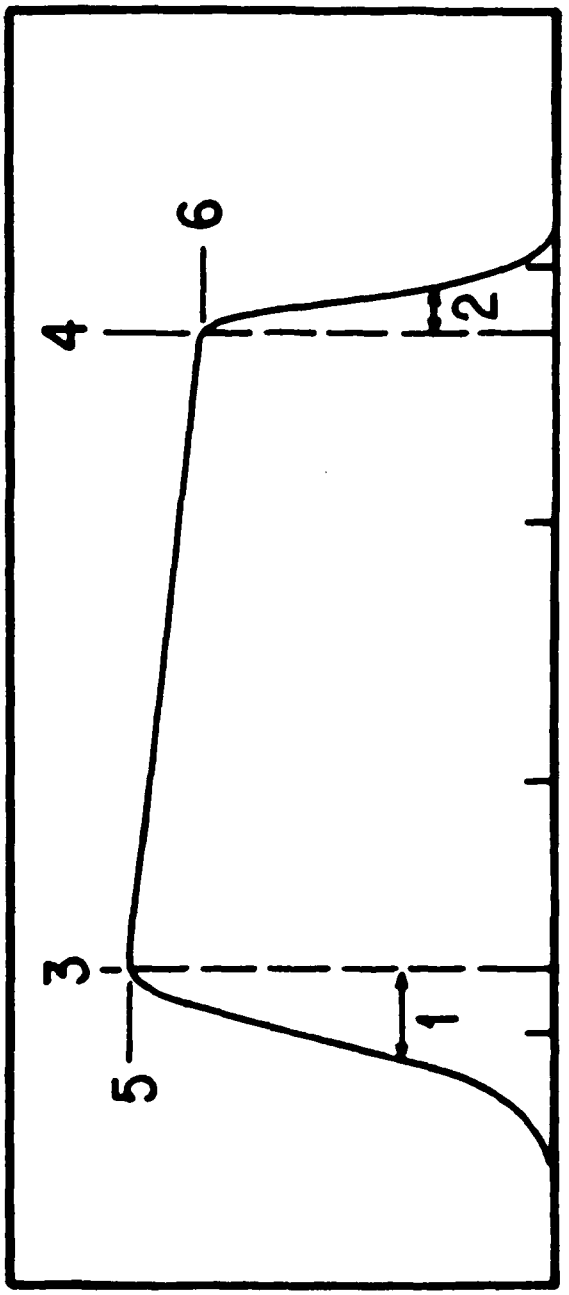
Counts/Channel
Channel Number
6
4
3
5
2
1

FIGURE 8

# BASIC BACKSCATTERING SPECTROMETRY

$Q$ = NUMBER OF HE IONS INCIDENT.

$A_i$ = COUNTS IN BS PEAK FOR ELEMENT $i$.

$\Omega$ = SOLID ANGLE SUBT. BY DETECTOR.

$\sigma_i$ = SCATTERING XSECTION, He ON $i$.

# Accurate Stoichiometry

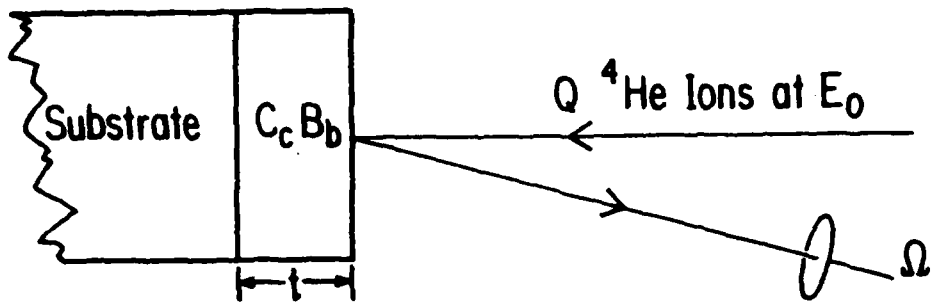


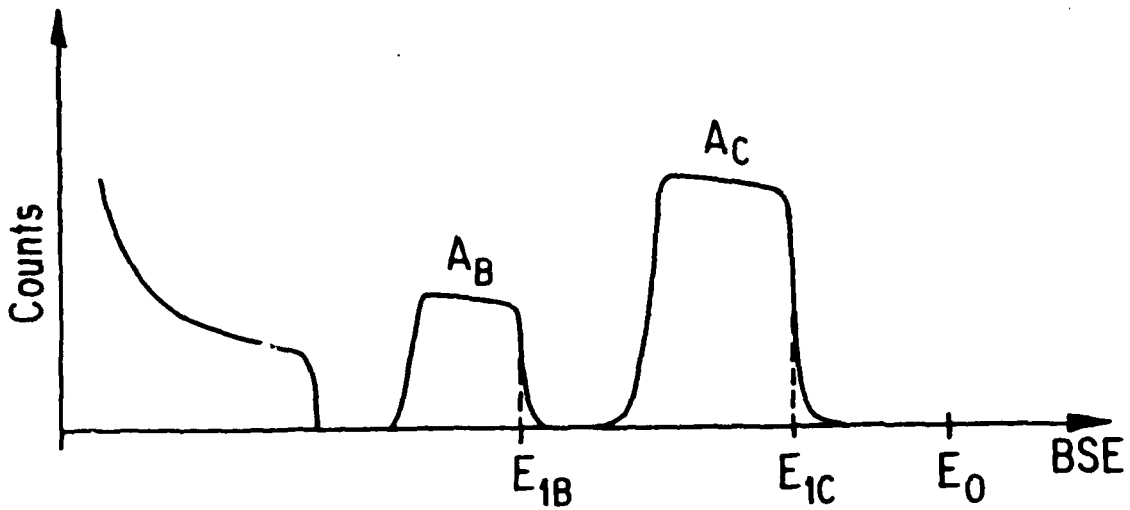


$$(Nt)_i = \frac{A_i}{Q\Omega\sigma_i}$$

$$\frac{c}{b} = \frac{N_c}{N_b} = \left(\frac{A_c}{A_B}\right)\left(\frac{\sigma_B}{\sigma_c}\right)$$

# ACKNOWLEDGEMENTS

WE EXPRESS THANKS TO C. FALCO AND HIS GROUP FOR PERMISSION TO USE THE DATA ON THEIR YBaCuO FILMS. WE THANK P. STOSS, B. DESFOULY-ARJOMANDY, M.D. ASHBAUGH, J. ODER, Z. YANG AND G. VAN ZYLL FOR ASSISTANCE IN TAKING AND ANALYZING THE DATA.

THE ION BEAM ANALYSYS FACILITY AT THE UNIVERSITY OF ARIZONA IS SUPPORTED BY IBM-TUCSON, THE AIR FORCE OFFICE OF SCIENTIFIC RESEARCH THROUGH THE UNIVERSITY RESEARCH INITIATIVE PROGRAM AND BY THE OPTICAL DATA STORAGE CENTER.

END

DATE

FILMED

5-88

DTIC